

# FUNCTIONALIZED BILAYER GRAPHENE FOR QUANTUM TECHNOLOGIES

by

Noel A. García-Martínez

Joaquín Fernández-Rossier

# Contents

---

<b>1</b>	<b>INTRODUCTION</b>	<b>1</b>
1.1	A nuclear spin based graphene quantum bit . . . . .	3
1.2	Scope of this thesis . . . . .	4
<b>2</b>	<b>GRAPHENE</b>	<b>8</b>
2.1	Basic definitions . . . . .	10
2.2	Slater-Koster tight-binding model . . . . .	12
2.2.1	Slater-Koster versatility . . . . .	14
Angular dependence . . . . .	14	
Other materials . . . . .	15	
2.3	Basic Properties . . . . .	17
2.4	Other Hamiltonian terms . . . . .	18
2.4.1	Mass . . . . .	18
2.4.2	Zeeman . . . . .	18
2.4.3	Spin-Orbit coupling . . . . .	19
2.4.4	Electric field and Rashba . . . . .	20
<b>3</b>	<b>GRAPHENE BILAYER</b>	<b>22</b>
3.1	Basic definitions . . . . .	24
3.2	electric field . . . . .	25
3.2.1	Gap opening . . . . .	26
3.2.2	Electric control of the charge density . . . . .	26
3.3	Topology and kink states . . . . .	28
3.4	Spin proximity . . . . .	29
<b>4</b>	<b>ANOMALOUS MAGNETISM OF <math>sp^3</math> DEFECTS ON GRAPHENE</b>	<b>33</b>
4.1	Adatom vs. vacancy . . . . .	34
4.2	A vacancy in gapless graphene . . . . .	35
4.3	Methods . . . . .	36
4.3.1	The embedding technique . . . . .	36

4.3.2 Mean field Hubbard model . . . . .	39
4.3.3 The kernel polynomial method . . . . .	40
4.4 Non interacting zero temperature magnetization . . . . .	41
4.5 Finite temperature susceptibility . . . . .	43
4.6 Effect of interactions . . . . .	44
4.6.1 Local magnetic moment . . . . .	46
4.6.2 Spin splitting . . . . .	48
4.6.3 Localization . . . . .	49
4.7 Conclusions . . . . .	50
5 <i>sp</i> <sup>3</sup> DEFECT IN BIASED BILAYER GRAPHENE	51
5.1 A note on the geometry . . . . .	51
5.2 Two types of vacancies . . . . .	52
5.2.1 Hollow sites . . . . .	54
5.2.2 Role of the interlayer coupling . . . . .	56
6 HYPERFINE COUPLING	60
6.1 Adatom in the SK-approximation . . . . .	60
6.2 Dependence on the parameters . . . . .	61
6.3 Hyperfine Interaction . . . . .	61
6.4 A Qubit Idea . . . . .	66
7 DESIGNER FERMION LATTICES	71
7.1 Methods . . . . .	72
7.2 One-body results . . . . .	73
7.3 Many-body results . . . . .	75
7.4 Conclusions . . . . .	80
8 CONCLUSIONS AND OUTLOOK	81
A MY PUBLICATIONS	82
B SLATER-KOSTER HOPPINGS	83
C QUANTUM SPIN HALL	86
C.1 Homogeneous multilayers . . . . .	86
The Model . . . . .	86
C.1.1 Calculation of the $Z_2$ invariant . . . . .	90
C.1.2 Edge states . . . . .	90
C.1.3 Heterogeneous multilayers . . . . .	93
D REAL SPACE MAPPING OF TOPOLOGICAL INVARIANTS USING ARTIFICIAL NEURAL NETWORKS	97
D.1 Introduction . . . . .	97
D.2 Method . . . . .	99
D.2.1 Artificial Neural Networks . . . . .	99
D.2.2 Correlation functions with the Kernel Polynomial method	102

D.3	Topological invariants with supervised learning . . . . .	104
D.3.1	One dimensional topological superconductor . . . . .	105
D.3.2	Two dimensional Chern insulator . . . . .	108
D.4	Conclusions . . . . .	111
E	ABOUT THE UNITS	113
E.1	Magnetic moment . . . . .	113
E.2	Exchange coupling . . . . .	113
E.3	Hyperfine coupling . . . . .	114
E.4	Electric Field Hamiltonian . . . . .	114
F	A COMPLETE LIST OF MY PUBLICATIONS	115

# Acronyms

---

<b>SK</b>	<i>Slater-Koster</i>
<b>DOS</b>	<i>Density of States</i>
<b>DFT</b>	<i>Density Functional Theory</i>
<b>TB</b>	<i>Tight-Binding</i>
<b>QHE</b>	<i>Quantum Hall Effect</i>
<b>QSH</b>	<i>Quantum Spin Hall</i>
<b>QSHI</b>	<i>Quantum Spin Hall Insulator</i>
<b>SOC</b>	<i>Spin-Orbit Coupling</i>
<b>TI</b>	<i>Topological Insulator</i>
$e^-$	electron
<b>TMD</b>	<i>transition metal dichalcogenide</i>
<b>2DM</b>	<i>Two Dimensional Materials</i>
<b>2D</b>	<i>Two Dimensional</i>
<b>1D</b>	<i>One Dimensional</i>
<b>STM</b>	<i>Scanning Tunneling Microscope</i>
<b>FBZ</b>	First Brillouin Zone
<b>CNP</b>	Charge Neutrality Point
<b>LL</b>	Landau Levels
<b>KPM</b>	Kernel Polynomial Method

# 1

## Introduction

The initial goal of this thesis was the exploration of graphene based nuclear spin qubits, very much inspired in the proposal for nuclear spin qubits in Silicon by B. E. Kane,<sup>1</sup> in 1988. In the original paper the proposed system consists of P donors on a Si matrix. The P donors have a nuclear spin  $I = 1/2$ . The control between the electronic and nuclear spin (for each P donor) was proposed via electric gating and a combination of external microwave and radio frequency pulses. Our plan was to explore an implementation of a similar system in a completely different material: hydrogenated bilayer graphene. Nevertheless, in the process of studying the spin interactions among qubits we thought of another application for this platform, namely, analog quantum simulation of fermionic lattice models that allows the study a broad class of emergent electronic properties and has the promise for not-so-long-term applications.

But let us start from the beginning. Every proposal for building qubits has to deal with two opposing requirements: the need for the qubits to be completely isolated from the environment and the need for them to interact quickly and strongly on demand so they can be read or written to.

Kane's proposal,<sup>1</sup> "A Silicon-based nuclear spin quantum computer" deals with the first requirement in the following way. The quantum information is to be stored in the nuclear spin of Phosphorus atoms inserted in a matrix of Silicon (Si :  $^{31}\text{P}$ ). The Si was selected for its abundance of spinless nuclear isotopes in addition to the huge industry behind it, ensuring the know-how to manipulate this material as needed. Once the host material was chosen, the options for donors were quite limited, in fact it turns out that the only shallow donor in Si with nuclear spin  $I = 1/2$  is Phosphorus<sup>2,3</sup> and, in particular, the isotope  $^{31}\text{P}$ . In addition, a number of studies show that its nuclear spin relaxation time can exceed 10 hours.<sup>2-4</sup>

When P dopants are introduced in Si, an electron is confined in the vicinity of the dopant. The extension of such state can be as large as hundreds of Ångströms so, if there are several dopants in the same area, the electronic states can act as an effective coupling among their nuclear spins.<sup>5</sup>

This approach takes advantage of the naturally weak interactions with the nuclear spin and the high tunability of the surrounding electronic states.

The processes to control the qubits depend upon implementations. In the original proposal it was required to have an electric gate on top of each of the dopants. The idea would be to deform the electronic cloud in the vicinity of the P nucleus, as shown in

[Fig. 1.1](#). The main effect of this deformation would be the increase/decrease the electronic density around the nucleus and with it the hyperfine interaction, resulting in a shift of the resonance frequency for the spin flip. The interaction between different qubits could be switched on and off using electric gating as well although its implementation requires, among other things, the dopants to be at a very specific distance (with atomic precision), which is definitely a challenge in this platform. Similarly the idea is to increase/decrease the electronic density in the inter-qubit space in order to allow/prevent the propagation of the spin information.

Another big challenge is the detection of the spin state at any given time of any of the components. Although there is not an ultimate answer for this problem, there are many ideas to work around it. The simplest option could be the use of a number of qubits all in parallel so the macroscopic magnetization could be measured. Also, if the nuclear spins are incorporated into an electronic device it is possible to infer the nuclear spin based on the electronic properties.<sup>6–11</sup> The most state-of-the-art implementation of this system has proven able to (destructively) read a single electronic spin state as well as read and manipulate single and double qubit systems.<sup>12–14</sup>

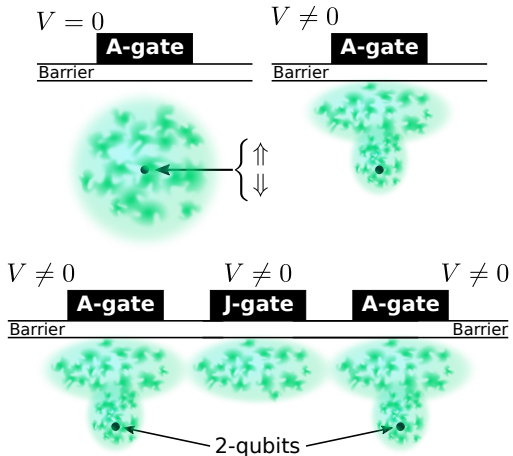


FIGURE 1.1: Sketch of the Kane's proposal for a silicon-based nuclear spin quantum computer. An electric gating  $A$  controls the hyperfine interaction by increasing/decreasing the electronic density around the nucleus, allowing the isolation of the nuclear spin on demand. Similarly, an inter-qubit gate allows the interconnection of different qubits.

## 1.1 A NUCLEAR SPIN BASED GRAPHENE QUANTUM BIT

Our proposal replaces the P dopants in Si by H adatoms on bilayer graphene. This system provides the same ingredients: a host with virtually no nuclear spin impurities,<sup>I</sup> a dopant with nuclear spin  $I = 1/2$  and a surrounding electronic spin  $S = 1/2$  spatially bounded to them.

The interaction with nuclear spin impurities in the host is a well known source of electronic spin decoherence for spin qubits. Therefore the small abundance of  $^{13}\text{C}$  with nuclear spin  $I = 1/2$  isotopes makes graphene a good choice for the host material.

The nuclear-electron interaction, known as the hyperfine coupling, is finite only for  $s$ -orbitals, and the  $1s$  level is the one binding the electron closest to the nucleus, making H a good candidate. At the same time, the chemisorption of the H adatom binds strongly its electron to the  $\pi$  electrons of graphene, removing most of it from the  $s$ -orbital, luckily the occupation of this orbital is highly tunable via electric gating. This tunability is a key element for this proposal since it is the mechanism that will allow us to switch on and off the interactions with the qubits.

The electronic states in graphene (and graphene bilayer) are known to be highly tunable. In particular, an external electric field would allow the control of their relevant properties such as the localization length.

The initial reason to consider bilayer graphene was the possibility of opening a band gap upon the application of an external electric field.<sup>15–23</sup> This conductor to insulator transition provides a handy knob to control the localization length of the electronic states which results in the control of its effective electron-electron interactions as well as the interactions with the nuclear spins.

Another advantage of using H adatoms on top of bilayer graphene over Si :  $^{31}\text{P}$  is that nowadays there are methods to place the H adatoms with atomic precision and in a reversible way.<sup>24–26</sup> Specifically around 20 H atoms have already been placed in a single sample and, in principle, there should be no physical limit since the process could be automatized for larger arrays.

The study of the tunable interactions in this system led us to the realization that H adatoms on bilayer graphene provide a framework where localized states can be placed at will and where the interactions among them are highly tunable upon the application of an external electric field. Such a system is the ideal playground to implement physical realizations of a wide variety of hamiltonians,

---

<sup>I</sup> The abundance of Carbon isotopes with nuclear spin  $I = 0$  is  $\sim 98.9\%$  (which could still be problematic, although that number for Silicon is  $\sim 92.2\%$ ) but, in principle, it should be possible to get isotopically pure Carbon.

the ultimate goal for analog quantum simulations. Our analysis show that by carefully choosing the placement of the adatoms (the distance and relative position among them) one can engineer the electron-electron interactions to explore both weakly and strongly interacting regimes.

This situation in which we can create localized electronic states at will and engineer the electron-electron interactions is specially appealing after the recent discovery of an unconventional superconducting phase in twisted bilayer graphene.<sup>27,28</sup> Even though it will not be discussed in the thesis, it is worth pointing out the similarities between our proposal and the newly found twisted bilayer graphene physics. In order to get superconductivity in twisted bilayer graphene two requirements are to be met. First, the twisting angle needs to take a very low (and particular) value. This requirement ensures the emergence of a Moire pattern which is responsible for the localization of electronic states in the boundaries between domains. These localized states result in the emergence of (almost) flat bands all over the Brillouin zone and very close to the Fermi energy. Second, the fine tuning of the filling factor is key to place the Fermi level in the middle of the flat bands and conveniently tune the electron-electron interaction.

In the case of twisted bilayers, the resulting phase diagram is quite similar to that of the cuprates family what may suggest a similar microscopic mechanism for superconductivity to appear. The big difference is that, while cuprates are a somewhat complex material, the chemistry of graphene has been very well known for a long time, and the behavior of the  $p$  orbitals (rather than  $d$  orbitals) is much simpler. The low energy effective model of graphene is probably the most studied in the history of Condensed Matter Physics so one may expect that studying the complex problem of unconventional superconductivity would be easier in this case.

Nevertheless, it looks like superconductivity will not give up its secrets so easily since, even though the low energy Hamiltonian of graphene is very well known, its extension to the twisted bilayer is not so easy. It is probably too soon to tell but the introduction of superconductivity in the graphene/2d-materials community may be a game changer for this hundred year old problem.

## 1.2 SCOPE OF THIS THESIS

Condensed Matter Physics is an immensely broad branch of Physics. It encompasses many different systems at different scales and with many different approaches. The same phenomenon can bridge the gape

It covers from the most applied ideas of metrology From deeply mathematical and theoretical ideas bridging the

This thesis sits on the theoretical side and is mainly computational. It approaches mostly graphene-based systems from a theoretical point of view, most often using numerical methods. Through out the whole thesis the driving force has been sometimes the possibility of interesting results, regardless their “immediate” utility, and some times the possibility of real world application in the near/mid future. This approach, midway between fundamental research and real world applications, offers a privileged position to explore a number of interesting topics without loosing touch with experimental reality.

This thesis revolves around graphene and graphene-based systems, with a special focus on the applications of a particular case: bilayer graphene. One could say that the scientific community may have gone through an “interest bubble” involving graphene and, as a consequence, it has been advertised as a miraculous material with the potential to change the world as we know it. I will not address the controversy of the almighty properties of graphene but I would like to briefly address the graphene hype within the scientific community. In order to have a somewhat quantitative description of the graphene hype I have analyzed the book of abstracts of the APS March Meeting since 2005 until 2019.<sup>II</sup> The analysis counts the number of abstracts containing a given term (or groups of terms) and normalizes the count to the total number of abstracts that year. This quantity is a very rough estimate, of course, but the resulting count is arguably related to the interest of the condensed matter community on a certain topic.

The case of graphene, first block of bars in Fig. 1.2, is very interesting, since one can see its raise since (almost) its discovery and the beginning of its decay. This trend is a strong indicator of a possible interest bubble, but I would like to point out the trend over the years of the terms next to it in Fig. 1.2 : topolog[ical], 2d, dirac, quantum-,spin-,anomalous-hall, dichalcogenides, MoS<sub>2</sub>, WS<sub>2</sub>, WSe<sub>2</sub><sup>III</sup>. All of these terms are undoubtedly related to graphene and clearly they show a steadily growing trend.

Graphene itself is very interesting and it probably deserves all the fame and attention that it gets, but I would argue that the importance of graphene lies in the fact that it has become the gateway for many other materials and even research branches.

---

II notice that 2018 is missing since I could not find the pdf for the full book of abstracts. Also, 2020 edition was canceled, but the book of abstracts was available in advance.

III the terms in grey are grouped during the counting process

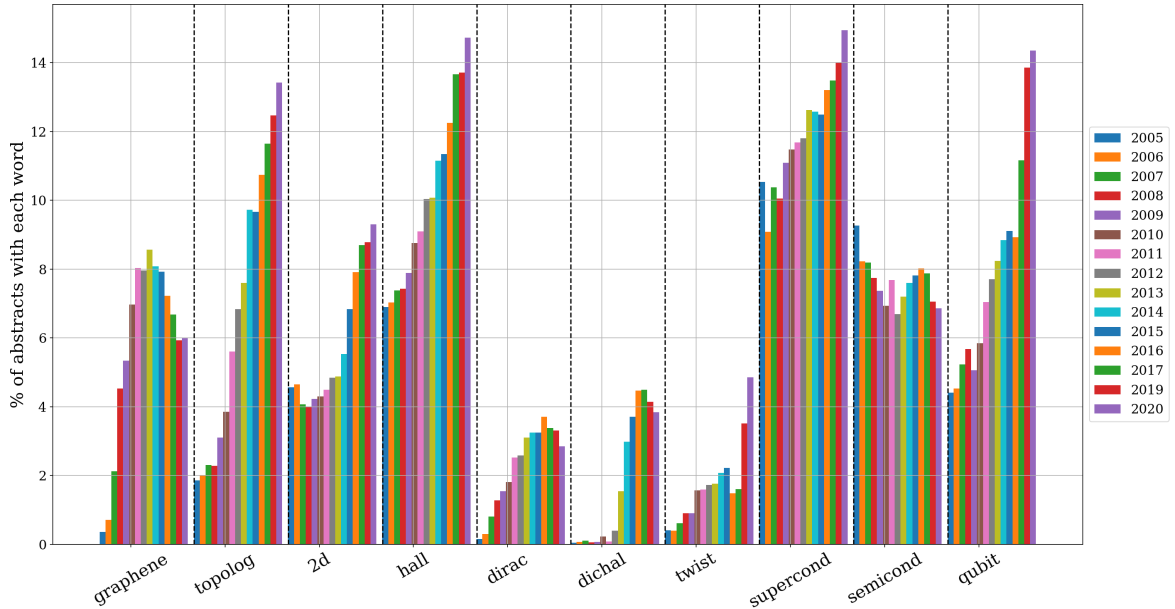


FIGURE 1.2: Evolution through out the years of different topics at the APS March Meeting. The plot was done by counting the number of abstracts containing a given word and normalizing it by the total number of abstracts in the conference. Note that the bars are placed in chronological order for each item.

The understanding of graphene has been the spark to start the race of two dimensional materials research. *Two Dimensional Materials (2DM)* are a very interesting family of materials both form an applied point of view and from the perspective of fundamental research. On one hand, any industry-related property (conductance tunability, magnetism...) becomes instantly interesting just because its 2D nature ensures smaller sizes and possibly cheaper products. On the other hand their 2D nature place them right in the frontier between the classical and quantum regime: they are macroscopic (sometimes reaching millimeters) but being one atom thick there are non negligible quantum effects all over the place, what makes the fascinating from the fundamental physics point of view. Since the discovery of graphene many other bidimensional materials have been synthesized: MoS<sub>2</sub>, WSe<sub>2</sub>, MoTe<sub>2</sub>, BN, CrI<sub>3</sub>, NbSe<sub>2</sub>, TaS<sub>2</sub>, MnBi<sub>2</sub>Te<sub>4</sub>... each with their unique set of properties and its list of possible applications in the rapidly growing field of Quantum Technologies. Some of these materials will be mentioned during the thesis, but graphene will be the common thread.

The rest of this thesis is structured as follows. Chapter 2 and Chapter 3 review the basic properties of graphene and bilayer graphene respectively, as well as most of the methods of calculation used along the thesis.



Chapter 4 is based on the publication [29] and it explores a number of properties of  $sp^3$  defects on graphene.

Chapter 5 expands onto the effects of  $sp^3$  defects on bilayer graphene.

Chapter 6 explores the tunability of the hyperfine coupling

Chapter ?? studies the possibilities of H adatoms on bilayer graphene as a platform to perform analogue quantum simulations.

# Graphene

# 2

This chapter aims to provide a self-contained introduction to the methods we use to model graphene as well as some of its most interesting/relevant properties. Specifically, I present the tight binding models that are used throughout the thesis. A more extended description of these methods and properties can be found in several reviews since graphene is one of the most studied materials in history.<sup>30–39</sup> Even before its experimental discovery, extensive research was devoted to it.<sup>40–47</sup> All the basic properties have been discussed profusely, yet, for the sake of completeness, I will make a brief recap of all the properties relevant for the rest of this thesis.

Graphene consists of a two-dimensional array of carbon atoms arranged in a honeycomb structure<sup>48</sup> like the one shown in Fig. 2.2 (a,b).

It has a peculiar band structure featuring two pairs of opposing cones touching exactly at the Fermi level. There are two main characteristics to highlight from this configuration, first, that the pairs of cones meet in a single point at the Fermi energy, and second, that the dispersion of the band structure is exactly linear for low energies.

This band structure is very unusual since it is different from both conductors and insulators. On the one hand it has available states for conduction infinitesimally close to the Fermi level (like a metal) but, on the other hand, it has no Fermi surface (like a semiconductor or an insulator). For this reason it is usually defined as a zero-gap semiconductor.

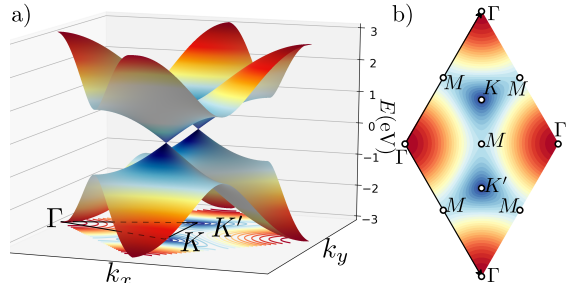


FIGURE 2.1: a) Band structure of graphene over the whole Brillouin Zone. Notice the cones in the  $K$  and  $K'$  points. b) Contour plot over the Brillouin Zone marking the high symmetry points.

The linear dispersion of the band structure is responsible for the strong modulation of the electric conductivity upon the application of an electric field. This phenomenon, usually known as field effect, is due to the strong doping induced via electric gating, which moves the Fermi level across the cones resulting in an important increase of the carriers density available for conduction which can be either electrons or holes since the band structure is symmetric around the Fermi Energy (electron-hole symmetry).

The linear dispersion is of special interest not only for the condensed matter community but also for the high energy. The electrons subjected to this linear dispersion are mathematically equivalent to having massless spin 1/2 particles obeying the Dirac's equation. This equivalency is quite straightforward from the analytical calculation of the tight-binding and is explored in detail later on.

Another consequence of the band structure is that the observed *Quantum Hall Effect* (QHE)<sup>49–56</sup> is different from the one in conventional semiconductors on 3 counts: first, it shows symmetric Landau Levels (LL) for electrons and holes; second , it has a "zero" LL, third, the quantization pattern has an extra 1/2 that arises from the non-trivial Berry phase of Dirac electrons

Graphene is expected to be a *Topological Insulator* (TI),<sup>57</sup> meaning that when all the interactions are taken into account, particularly the *Spin-Orbit Coupling* (SOC), the described linear dispersion is supposed to open a small gap, in the order of a few  $\mu\text{eV}$  although not measured experimentally, possibly due to temperature smearing and device precision. This gap nonetheless is not a standard insulating band gap. In finite samples the band structure would appear gaped everywhere, but two conducting channels would appear on the edges of the sample. This conducting states, spatially bounded to the edge of the system, are the so-called topological edge states and are known to be robust against any perturbation (that does not close the gap by breaking time-reversal symmetry).

Appendices C and D are two of my published papers which expand on these topics. The first explores the topological character of few-layer-graphene exploring the proximity effect of different materials. The second explores the bulk-edge correspondence<sup>58</sup> using neural networks to estimate the topological phase of some systems based only on a subset of the density matrix corresponding to the bulk region.

## 2.1 BASIC DEFINITIONS

Unless otherwise stated, we will consider that the unstrained atomic distance between carbon atoms is  $d_{\text{C-C}} = a = 1.4 \text{ \AA}$  in accordance with literature.<sup>30,36,59</sup>

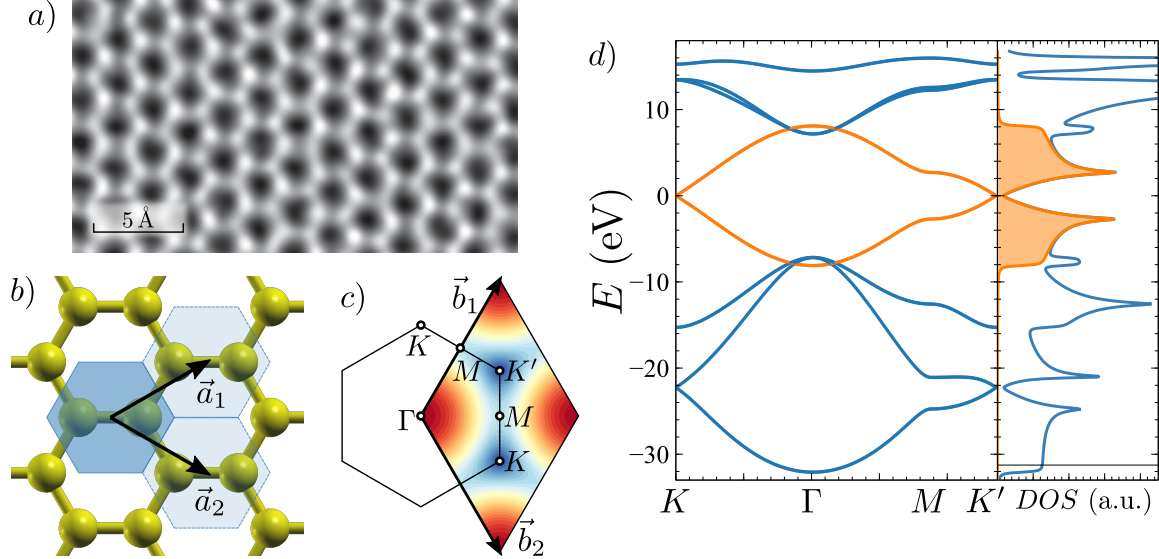


FIGURE 2.2: *a)* STM image of graphene taken from ref.<sup>48</sup> *b)* Cartoon depiction of the atomic structure of graphene using the lattice vectors defined in eq. 2.2 and the Wigner-Seitz cell. *c)* Reciprocal vectors  $\vec{b}_i$  and two representations of the FBZ. *d)* Band structure and DOS of graphene calculated in the tight-binding approximation (details later in the text).

The honeycomb structure is not a Bravais lattice so, in order to describe the system in terms of Bloch functions, we have to choose a unit cell and the appropriate lattice vectors to tessellate the space. Naturally there are infinite possibilities to do so, but the simplest one is that depicted in Fig. 2.2 b). It consists of two atoms per unit cell and a triangular lattice. We will consider the following atomic positions:

$$\vec{r}_a = \frac{a}{2}(-1, 0, 0) \quad ; \quad \vec{r}_b = \frac{a}{2}(1, 0, 0), \quad (2.1)$$

The lattice vectors that define the triangular Bravais lattice are, then:

$$\vec{a}_1 = \frac{a}{2}(3, \sqrt{3}, 0) \quad ; \quad \vec{a}_2 = \frac{a}{2}(3, -\sqrt{3}, 0) \quad (2.2)$$

This geometry defines a hexagonal Wigner-Seitz cell (blue region on Fig. 2.2 b)) with area  $\sim 5.1 \text{ \AA}^2$ . The reciprocal lattice vectors are depicted in Fig. 2.2 c) and can be easily calculated using the relation:<sup>60</sup>  $\vec{a}_i \vec{b}_j = 2\pi\delta_{ij}$ . Notice that the

canonical First Brillouin Zone (FBZ) shown in Fig. 2.2 c) is an hexagon (just like the Wigner–Seitz cell) but nothing changes if we use the colored rhomboidal region instead, which is much more convenient for computational calculations.

Once the atomic and lattice structure is clear, we turn to the electronic properties. Carbon atoms have 6 electrons allocated in five orbitals distributed in the layers with quantum number  $n \in \{1, 2\}$ . The first two electrons are in the  $1s$  level, two more in the  $2s$  level and finally another two electrons ( $e^-$ ) in the three  $2p$  levels (Fig. 2.3). Since the orbitals  $n = 1$  are doubly occupied and

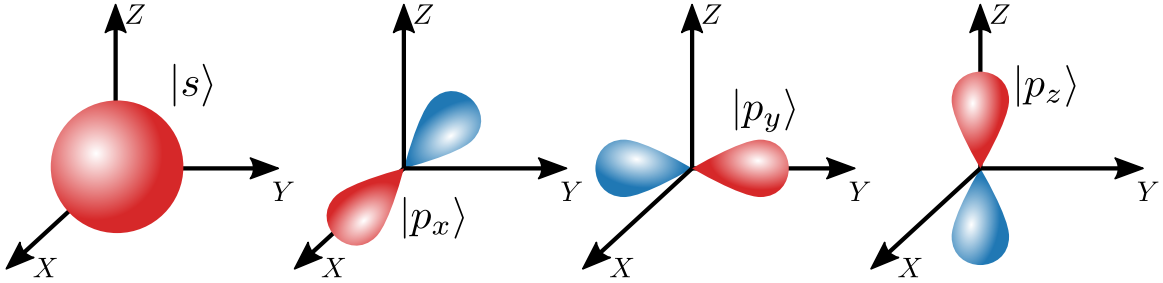


FIGURE 2.3: Cartoon depiction of the hydrogenoid orbitals involved in the graphene chemical and physical properties. The color of the orbitals shows the parity of the orbital what will be relevant when building tight-binding models.

far down in energy, there is no need to consider them. The  $2s$  level is also full, but they show a strong hopping with neighbouring  $p$  orbitals which are around the Fermi energy so we will consider their contribution. The  $2p$  orbitals are the closest to the Fermi level, hence they will play a major role in the chemistry of graphene.

With this description of the system we can build a basis which will have four orbitals per Carbon atom:

$$\mathcal{B}_4 = \{|\phi_s^1\rangle, |\phi_{p_x}^1\rangle, |\phi_{p_y}^1\rangle, |\phi_{p_z}^1\rangle, \dots, |\phi_s^n\rangle, |\phi_{p_x}^n\rangle, |\phi_{p_y}^n\rangle, |\phi_{p_z}^n\rangle\} \quad (2.3)$$

where the superscript points out the atom and the subscript shows the corresponding orbital. The bands calculated in the *Tight-Binding* (TB) approximation resulting from this description are shown in Fig. 2.2 d). We will delve in the physical properties later on, but for now it should suffice to point out the linear dispersion in the  $K$  and  $K'$  points around the Fermi energy (taken always as  $E_F = 0$  eV) as well as the decoupling of the two bands involved in the low energy regime. These two bands (colored in orange) are composed exclusively by  $p_z$  orbitals as it can be seen in the *Density of States* (DOS) (side panel of Fig. 2.2 d)).

In many cases it is enough to describe the two bands closest to the Fermi energy since the phenomenon at hand is restricted to the low energy region. In those cases we will reduce our basis and consider only the  $p_z$  orbitals, resulting in the basis:

$$\mathcal{B}_1 = \{|\phi_{p_z}^1\rangle, |\phi_{p_z}^2\rangle, \dots, |\phi_{p_z}^n\rangle\} \quad (2.4)$$

There are a number of ways to build a *Tight-Binding* (TB) Hamiltonian. When using the single orbital basis eq. 2.4 the hopping parameters are a single scalar and it is enough to fit the band width to estimate it, but for a more complex description using the four orbital basis eq. 2.3 the estimation of the parameters is not so easy. In the next section we show the details for the Hamiltonian models used all along this thesis.

## 2.2 SLATER-KOSTER TIGHT-BINDING MODEL

In general, the hopping parameters are an input in any *Tight-Binding* (TB) model. They are usually calculated by fitting eigenvalues (and possibly eigenfunctions) obtained from *Density Functional Theory* (DFT) calculations. Another way to calculate the hopping parameters is to project the DFT eigenfunctions into a basis of localized atomic orbitals so the interpretation in terms of hydrogenoid orbitals is easier.

As a system grows complex, more and more parameters are needed to describe it. In fact, the number of hoppings grows with the size of the basis,  $n_B$ , as  $\sum_i^{n_B} i$ . Nevertheless since the number of different orbitals is finite and a larger basis means only a more complex arrangement of orbitals, one could expect that not every parameter is completely independent from the others. The SK approximation<sup>61</sup> takes into account the symmetry of the atomic orbitals to reduce the number of parameters needed since some of them are related by rotations or other symmetry operations.

In the TB approximation the two-center hopping integrals,<sup>60,62</sup>

$$t_{\phi_1-\phi_2} = \langle \phi_1(\vec{r}) | H'(\vec{r}, \vec{r}') | \phi_2(\vec{r}') \rangle$$

express the probability of an electron to transition between two orbitals, due to the inter-atomic interactions contained in  $H'$ . In the SK apprcimation these integrals are encoded in a set of constants:  $V_{\alpha\alpha'm}$ , where  $\alpha$  and  $\alpha'$  label the orbitals and  $m$  refer to the component of angular momentum along the line between the center of the two orbitals. Two examples of these constants,  $V_{sp\pi}$  and  $V_{sp\sigma}$ <sup>I</sup>, are shown in Fig. 2.4 a).

---

I Notice that in graphene  $V_{sp\pi}$  automatically vanishes because of the symmetry of the orbitals.

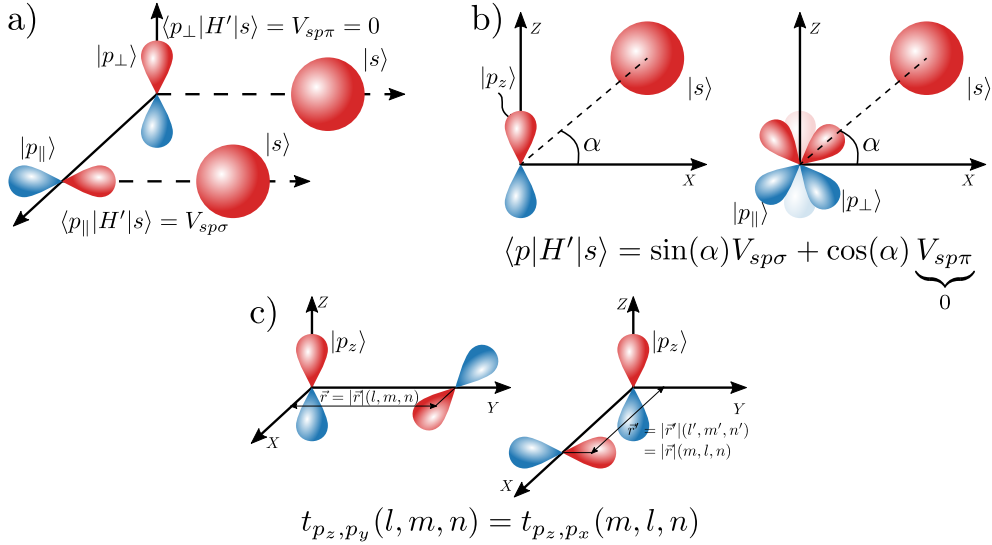


FIGURE 2.4: a) Definition of the parallel and perpendicular hoppings. Notice that  $V_{sp\pi} = 0$  because of the symmetry of the orbitals (integral of the product of an even and an odd function). b) Decomposition of a  $p_z$ - $s$  hopping in terms of its parallel and perpendicular projections. c) These two hoppings must have the same value regardless of the definition of the axes. This is the way *Slater-Koster* (SK) hoppings are derived from one another.

It is important to notice that the radial information, i. e. the distance between atoms, is enclosed in the SK parameters  $V_{\alpha\alpha'm}$ , while the angular dependence, i. e. the atomic positions, provide the functional dependencies in the SK model. For instance, if we focus on the hopping between two  $p_x$  orbitals<sup>61</sup> separated by a distance  $\vec{r} = |\vec{r}|(l, m, n)$ :

$$t_{p_x-p_x}(\vec{r}) = t_{p_x-p_x}(l, m, n) = l^2 V_{pp\sigma}(r) + (1 - l^2) V_{pp\pi}(r) \quad (2.5)$$

The radial information (distance between atoms) will be encoded in the numerical values of  $V_{pp\sigma}$  and  $V_{pp\pi}$  while the geometrical information of the lattice will be contained in the factors  $l^2$  and  $(1 - l^2)$ .

Most of the time the distance dependence of the parameters can be ignored, but as a rule of thumb one can consider that the SK parameters will decrease as the distance between the orbitals increases. The exact ratio depends on the orbitals and the crystalline structure, and different approximations can be found in the literature,<sup>63</sup> but  $V_{\alpha,\alpha'm}(r) \sim 1/r^5$  is a standard estimation.

The SK description of the TB hopping integrals allows the formulation of every hopping in terms of a few parameters which encode the distance between orbitals while preserving the angular information in the analytical formulation which has been reproduced from the original publication in appendix B.

By projecting the hopping integrals into its parallel and perpendicular components (see Fig. 2.4 b)) we reduce the number of parameters needed to account for all possible hoppings. For instance, we only need two parameters:  $V_{pp\sigma}$  and  $V_{pp\pi}$  in order to express all six  $p - p$  hoppings.

This description of the hopping parameters also accounts for the symmetry of the orbitals. For instance Fig. 2.4 c) shows the relation between the hoppings  $t_{p_z,p_x}$  and  $t_{p_z,p_y}$ . If we forget about the labels in the axis, we can realize that these two hoppings are in fact equivalent since one can be obtained as a rotation of the other.

If we define the unitary vector  $\hat{r} = \vec{r}/|\vec{r}|$  and its components  $\hat{r} = (l, m, n)$  we can see that

$$t_{p_z,p_x}(l, m, n) = t_{p_z,p_y}(m, l, n) \quad (2.6)$$

notice that the change in the arguments is equivalent to perform a rotation of the vector  $\vec{r}$  of  $-\pi/2$  around the  $Z$  axis as depicted in Fig. 2.4 c).

The SK model exploits this kind of transformations in order to calculate every possible hopping, which has been done in appendix B.

### 2.2.1 *Slater-Koster versatility*

#### *Angular dependence*

An example of the versatility of decoupling the angular and radial dependencies can be shown in the following gedankenexperiment. Let us consider graphene and let us displace vertically a little bit one of the sublattices<sup>II</sup> so we end up with a slightly distorted graphene in which not all the atoms are in the same plane. This shift out of the plane has an important effect in the band structure since it breaks the mirror symmetry that kept the  $p_z$  orbitals isolated from every other orbital. This mixing of the  $p_z$  manifold with all the other orbitals happens mainly at  $\Gamma$  and it can be seen both in the band structure and in the DOS.

---

<sup>II</sup> If it boggles your mind you can shift all the atomic positions to keep the C-C distance as  $a = 1.4 \text{ \AA}$

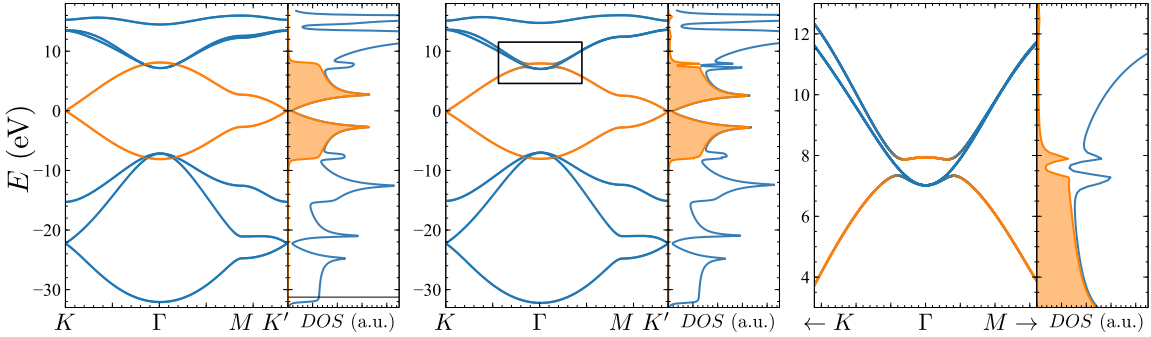


FIGURE 2.5: a) Pristine graphene band structure and DOS. b) Buckled graphene band structure and DOS. c) zoom around the  $\Gamma$  point where the  $\sigma$ -orbitals hybridize with the  $\pi$ -manifold.

This simple example shows how easy it is to account for geometric distortions using the SK model. Notice that the buckling used in this example is quite similar to that naturally occurring in other materials such as 2-D Bismuth crystals.

### *Other materials*

Once we have the machinery to build SK hamiltonians, simply by changing the SK parameters we can describe different materials. In this section we compare graphene, bismuth and  $h$  – BN as simple examples where the SK description works well.

In order to describe **graphene**, different sets of parameters can be found in the literature.<sup>64–66</sup> Nevertheless some of the parameters used here have been fitted from DFT calculations. The SK parameters in eV used for graphene are:

Hopping	$V_{ss\sigma}$	$V_{sp\sigma}$	$V_{pp\sigma}$	$V_{pp\pi}$	On-site	$s$	$p_x$	$p_y$	$p_z$
C – C	-7.76	8.16	7.48	-2.7	C	-8.8	0.0	0.0	0.0
C – H	-6.84	7.81	–	–	H	-2.5			

(2.7)

where the hoppings with a hypothetical H atom have been included for later convenience.

The description of  **$h$  – BN** is quite similar to that of graphene, it suffices to add a different on-site energy for the B and N atoms ( $E_B = -E_N = 2.5$  eV) while keeping the inter-atomic hoppings similar to those of graphene.

**Bismuth** is a little bit more complex since an accurate description requires up to third neighbor hoppings (and spin-orbit coupling as well, which we will neglect for the moment). The SK parameters, taken from [67] are:

Hopping	$V_{ss\sigma}$	$V_{sp\sigma}$	$V_{pp\sigma}$	$V_{pp\pi}$	On-site	$s$	$p_{x,y,z}$
1	-0.608	1.32	1.854	-0.6	Bi	-10.906	-0.486
2	-0.384	0.433	1.396	-0.344			
3	-	-	0.156	-			

(2.8)

The respective band structure of all these materials is shown in Fig. 2.6. For all panels, the color,  $\mathcal{C}$  represents the weight of the  $p_z$  orbital in each state:

$$\mathcal{C}_\alpha = \langle \psi_\alpha | \mathcal{O}_{p_z} | \psi_\alpha \rangle$$

where  $\mathcal{O}_{p_z}$  is the  $p_z$  projector operator and  $|\psi_\alpha\rangle$  are the Hamiltonian eigenfunctions.

$$H|\psi_\alpha\rangle = E_\alpha|\psi_\alpha\rangle \quad ; \quad |\psi\rangle = \sum_i c_i |\phi_i\rangle \quad \text{for} \quad |\phi_i\rangle \in \mathcal{B}_4$$

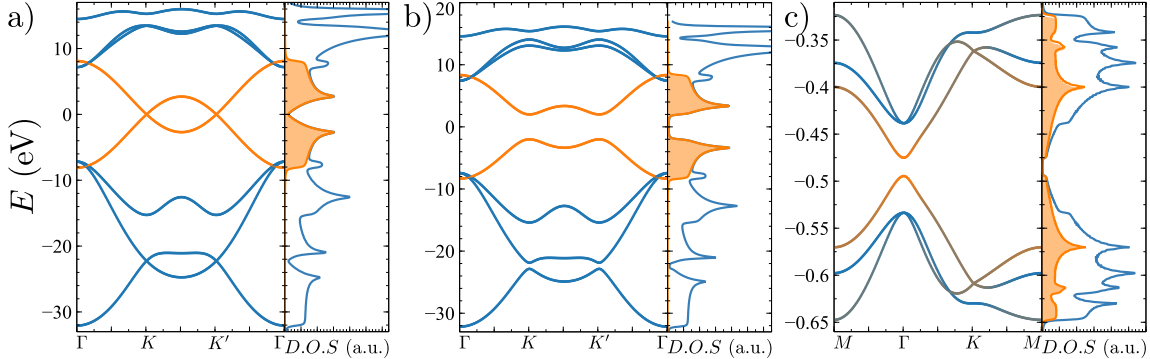


FIGURE 2.6: a) Graphene bands in the SK approximation, with  $s$ ,  $p_x$ ,  $p_y$ ,  $p_z$  orbitals for the C atoms. The color denote the  $p_z$  component of each state. It can be seen that the  $p_z$  orbital are decoupled from the rest of the orbitals. b)  $h$  – BN band structure, similar to that of graphene, but with a gap open due to the difference in the on-site energies between the B and N atoms. c) Bismuth band structure, since its atomic structure is buckled, the  $p_z$  orbital is not decoupled from the others as it can be seen by the smooth change in color of the central bands.

These examples show that the SK model provides a simple and versatile framework to capture a wide range of phenomena. It will be specially useful to capture structural deformations.

### 2.3 BASIC PROPERTIES

We are going to use a TB model in the SK approximation with four orbitals per carbon atom to describe graphene. The band structure obtained with this model is shown in Fig. 2.7 .

The first thing to notice about the graphene bands is the orbital distribution of the bands. As mentioned before, the  $p_z$  orbitals are responsible for the central bands, crossing the Fermi energy ( $E_F = 0.0$  eV). Due to the mirror symmetry of the system (with respect to the atomic plane), every hopping between the  $\sigma$ -orbitals and  $p_z$  vanishes exactly (see the definition of  $V_{sp\sigma}$  in Fig. 2.3 a)). The presence of *only*  $p_z$  orbitals around the Fermi energy makes it possible to describe the system solely with these orbitals.

The second thing to notice is that around the Fermi level, the band dispersion is linear. In particular, the band structure forms two pairs of cones in the  $K$  and  $K'$  points of the FBZ. This famous feature, dubbed the Dirac Cones is responsible for many of the interesting properties of graphene

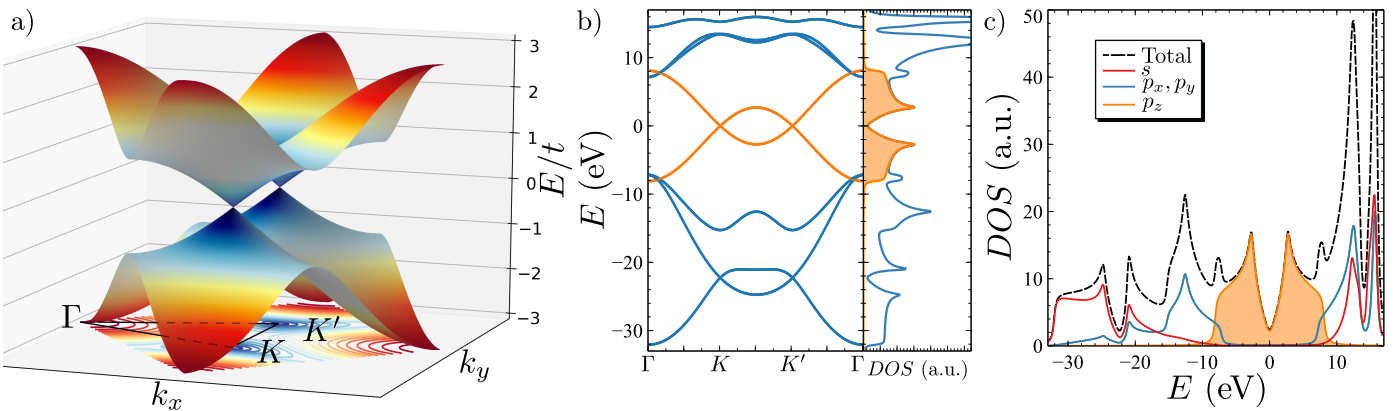


FIGURE 2.7: a) 3D representation of the  $p_z$  bands of graphene. Notice the two cones in the center of the FBZ. b) Band structure of graphene and DOS. c) DOS of graphene by orbital. Notice that the  $p_x$  and  $p_y$  contributions are degenerate.

In fact it is an easy exercise to calculate the band dispersion analytically. The Hamiltonian (already in the  $k$ -space) is:

$$H(\vec{k}) = H_0 + V_1 e^{-i\vec{k}\vec{a}_1} + V_2 e^{-i\vec{k}\vec{a}_2} + V_1^\dagger e^{i\vec{k}\vec{a}_1} + V_2^\dagger e^{i\vec{k}\vec{a}_2} \quad (2.9)$$

where  $\vec{a}_i$  are the lattice vectors described in eq. 2.2 and, in the one orbital basis  $\mathcal{B}_1$  described by eq. 2.4 , can be written as

$$H_0 = \begin{pmatrix} \varepsilon_A & t \\ t & \varepsilon_B \end{pmatrix} ; \quad V_1 = V_2 = \begin{pmatrix} 0 & 0 \\ t & 0 \end{pmatrix} \quad (2.10)$$

which allows us to rewrite eq. [eq. 2.9](#) as

$$H(\vec{k}) = \begin{pmatrix} \varepsilon_A & tf(\vec{k}) \\ tf^\dagger(\vec{k}) & \varepsilon_B \end{pmatrix} ; \quad f(\vec{k}) = 1 + e^{-i\vec{k}\vec{a}_1} + e^{-i\vec{k}\vec{a}_2} \quad (2.11)$$

where we have assumed that the hopping integral between two coplanar  $p_z$  orbitals is real. We have explicitly added a different on-site energy  $\varepsilon_{A/B}$  for each of the sublattices

Finding the eigenvalues of  $H(\vec{k})$  we obtain

$$E(\vec{k}) = \frac{\varepsilon_B - \varepsilon_A}{2} \pm \sqrt{\frac{\varepsilon_A^2 + \varepsilon_B^2}{4} - \frac{\varepsilon_A \varepsilon_B}{2} - 4(\varepsilon_A \varepsilon_B - t^2 f(\vec{k}) f^\dagger(\vec{k}))} \quad (2.12)$$

yet in graphene these parameters vanish:  $\varepsilon_A = \varepsilon_B = \varepsilon = 0$  so the dispersion for the eigenvalues of the Hamiltonian:

$$E(\vec{k}) = \pm \sqrt{4t^2 f f^\dagger} = \pm 2|tf(\vec{k})| \quad (2.13)$$

## 2.4 OTHER HAMILTONIAN TERMS

The Hamiltonian of graphene has been used as a toy model to describe many other materials since their Hamiltonian can be obtained as some modification of that of graphene. Here we explore some of the most commonly used Hamiltonian terms.

### 2.4.1 Mass

If we were to consider not graphene but some other material with the same structure but different on-site energies for each sublattice, a so-called “mass” term would have to be introduced. This term appears in the description of  $h - BN$  and even can be included in the proper description of graphene to account for some proximity effect.

The main effect of such a term is to open a trivial gap at the Dirac points as it was shown in the  $h - BN$  bands [Fig. 2.6 b](#)).

### 2.4.2 Zeeman

The application of an external magnetic field usually has several effects in a material. While a lot of interesting Physics is developed around the formation of Landau levels, we will restrict our study to the simpler case of the Zeeman

splitting of the energy levels. This effect consists of a symmetric splitting of up ( $\uparrow$ ) and down ( $\downarrow$ ) spins, resulting in a vertical shift the bands for each spin flavor.

### 2.4.3 Spin-Orbit coupling

The *Spin-Orbit Coupling* (SOC) is a relativistic interaction that can be interpreted in classical terms (allowing the existence of spin in classical physics) as the interaction between the spin of the electron and the electrostatic potential of the nucleus.

In most of this section we are going to use the four orbital basis eq. 2.3 with the geometry of Fig. 2.2 b), also described in the first section of the chapter. In this basis there are two atoms per unit cell and four orbitals per atom, so our Hamiltonian would be a  $8 \times 8$  matrix. When interactions concerning the spin are taken into account, the basis needs to be doubled and we choose the following order to do so:

$$\mathcal{B}_4^s = \{|\phi_{s\uparrow}^1\rangle, |\phi_{s\downarrow}^1\rangle, |\phi_{p_x\uparrow}^1\rangle, |\phi_{p_x\downarrow}^1\rangle, |\phi_{p_y\uparrow}^1\rangle, |\phi_{p_y\downarrow}^1\rangle, \dots, |\phi_{p_z\uparrow}^n\rangle, |\phi_{p_z\downarrow}^n\rangle\} \quad (2.14)$$

So the SOC Hamiltonian term can be written as follows:

$$H_{SO} = \lambda_{SO} \vec{L} \vec{S} = \lambda_{SO} [L_x S_x + L_y S_y + L_z S_z] = \lambda_{SO} \left[ L_z S_z + \frac{1}{2} (L^+ S^- + L^- S^+) \right] \quad (2.15)$$

just by taking into account the relations

$$S^+ = S_x + iS_y \quad ; \quad S^- = S_x - iS_y$$

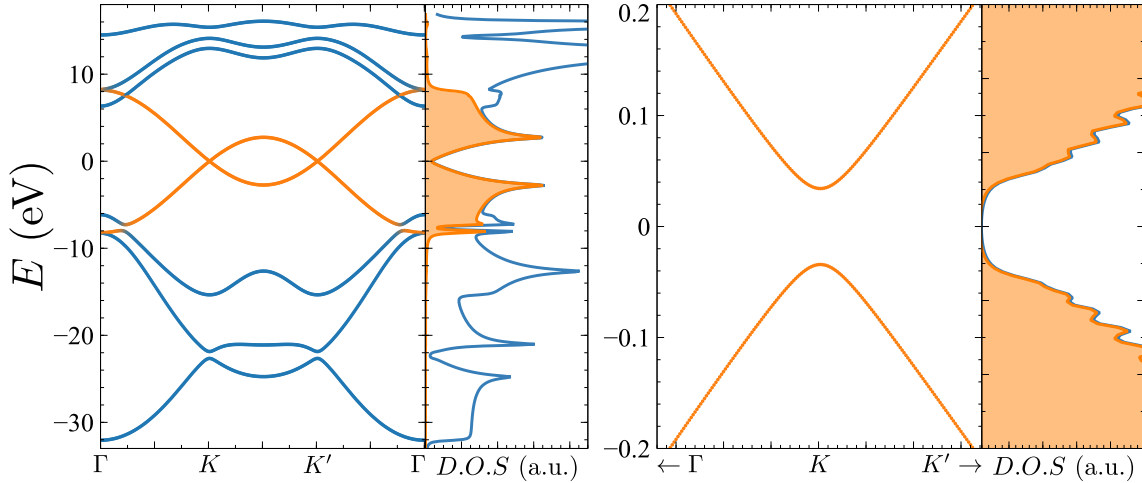


FIGURE 2.8: a) Graphene band structure in the presence of SOC. The gap due to SOC is not visible at this scale but the mixing of the  $p_z$  orbital with the  $\sigma$ -bands becomes apparent near  $\Gamma$ . b) Zoom to the surroundings of the Dirac point. A gap is open in the band structure turning graphene into a topological insulator. The spikes in the DOS are just an artifact of the calculation due, mainly, to the limited precision in the k-space integration.

This term is responsible for the opening of a band gap at the  $K$  points turning graphene into a TI. This term is known to be equivalent to having a second neighbor imaginary hopping in the  $p_z$  manifold.<sup>45,68,69</sup> This term induces a non-trivial Berry phase which gives rise to its topological behavior. This term is at the core of the *Quantum Spin Hall* (QSH) effect.

#### 2.4.4 Electric field and Rashba

An electric field has several effects that will be discussed extensively along the thesis. It should suffice for now to discuss briefly the orbital consequences. When an external electric field perpendicular to the material is applied the atomic orbitals get deformed, breaking the mirror symmetry that protects the  $\pi$ -manifold. The breaking of this symmetry opens an effective hopping channel for mixing  $s$  and  $p_z$  orbitals.

Another effect, alongside the SOC, is the appearance of a spin-flip channel via the following process: an  $\uparrow$  electron in a  $p_z$  can transition to a  $s$  orbital in the same atom via rashba hopping, then to a  $p_{x/y}$  orbital centered in a neighboring atom, which is connected via SOC with a  $p_z$  with spin  $\downarrow$ .

Following the calculations in<sup>70</sup> we can see that the relation between the applied electric field and the effective intra-atomic Rashba follow the equation:

$$\lambda_R = \frac{e\mathcal{E}z_0}{3V_{sp\sigma}}\xi \quad ; \quad \lambda_{SOC} = \frac{|E_s|}{18V_{sp\sigma}^2}\xi^2 \quad (2.16)$$

where  $\xi \sim 6$  meV is the atomic carbon spin-orbit coupling strength which for a typical electric field of  $\mathcal{E} \sim 50$  V/300 nm result in an effective Rashba coupling  $\lambda_R \sim 0.011$  meV and the SOC  $\lambda_{SOC} \sim 0.0011$  meV.

These terms, are in the scale of  $10^{-2}$  meV while the gap open can reach up to  $2.5 \cdot 10^2$  meV so we will neglect these interactions from now on.

If we consider bilayer graphene, the application of an electric field has another important effect. It shifts the on-site energy of each layer which results in an opening of a gap in the band structure. This results in a very useful feature that will be exploited throughout the thesis.

# Graphene Bilayer

# 3

---

In this chapter I present a summary of the main electronic properties of graphene bilayers, as described with tight-binding models introduced in the previous chapter. Graphite is made out of weakly bounded graphene layers which, incidentally, is the main reason why it is such an exfoliable material. When graphene is obtained by exfoliation it is very common to find regions where not one but two or more layers are extracted. We will focus now in the cases in which just two layers are isolated.

There are only two ways to stack two graphene layers in a commensurate way keeping only two atoms per unit cell. The first option is to align directly one layer on top of the other, so every atom in one layer is connected to an atom from the other layer (Fig. 3.1 a). This is the so-called *AA*-stacking. The other option is to have the top layer shifted by one atomic position as shown in Fig. 3.1 c). The later stacking, commonly called Bernal stacking or *AB*-stacking, is the most common one according to both experiments and *Density Functional Theory* (DFT) calculations.<sup>71–73</sup>

In both stackings the overall band structure (see Fig. 3.1 b,d)) is quite similar since the interlayer interaction is around one order of magnitude weaker than any intralayer hopping. At first glance it may seem that both stackings result in a very similar band structure. The main differences happen around the  $K$  ( $K'$ ) points as it is shown in Fig. 3.1 e).

In order to understand these band structures we can consider the adiabatic formation of bilayer graphene (or  $n$ -layer graphene, for that matter) starting with two layers of graphene infinitely apart and bringing them together. We will use the following basis to describe such a system:

$$\mathcal{B}_1 = \{|\phi_{1A}\rangle, |\phi_{1B}\rangle, |\phi_{2A}\rangle, |\phi_{2B}\rangle\} \quad (3.1)$$

where the numbers label the layer and the letters the sublattice.

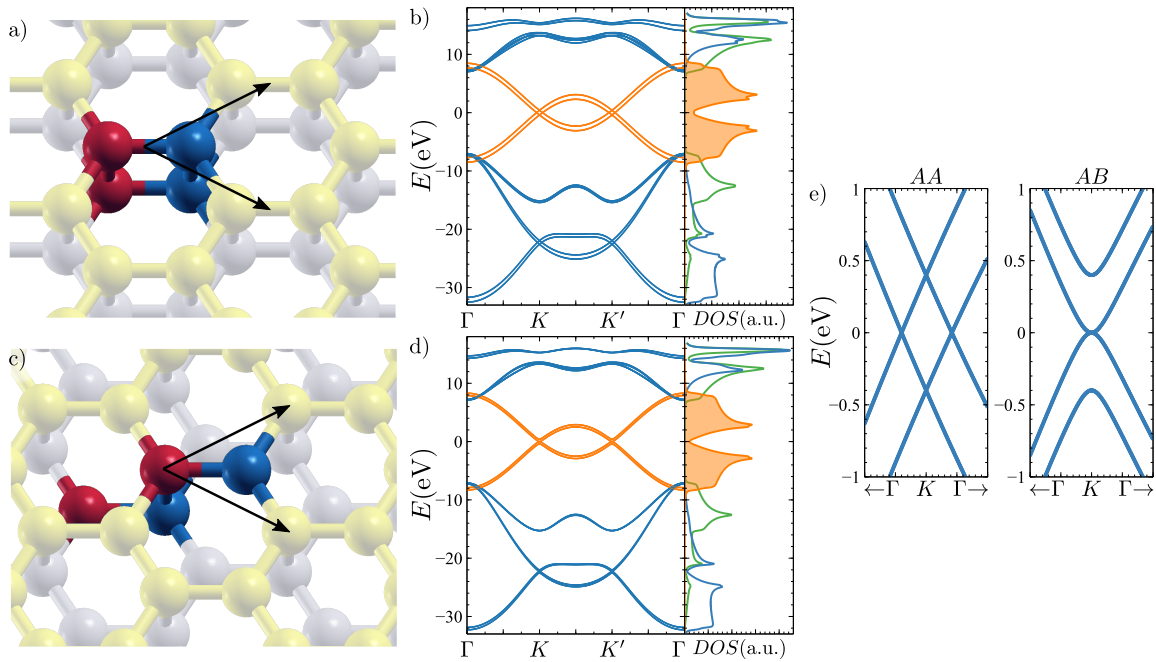


FIGURE 3.1: a,b) Cartoon depiction of the atomic structure of bilayer graphene in *AA*-stacking and band structure of *AA*-stacking respectively. c,d) Cartoon depiction of the atomic structure of bilayer graphene in *AB*-stacking and band structure of *AB*-stacking respectively. e) Comparison of the *AA* and *AB* stackings in the band structure around the *K* point.

Initially there is no hopping between the layers, but as they are brought together a finite hopping appears. We will simulate this adiabatic process including a factor  $\eta \in [0, 1]$  in the interlayer hoppings.

Since the two layers are infinitely apart, we can consider no interaction between them, hence we can describe the Hamiltonian of the system at the initial moment as two disconnected sectors of the same Hamiltonian, equivalent to the limit  $\eta \rightarrow 0$  in eq. [eq. 3.2](#). The Hamiltonian in the one orbital basis<sup>I</sup>  $\mathcal{B}_1$  reads:

$$H^{AA} = \begin{pmatrix} 0 & tf & \eta t' & 0 \\ tf^\dagger & 0 & 0 & \eta t' \\ \eta t' & 0 & 0 & tf \\ 0 & \eta t' & tf^\dagger & 0 \end{pmatrix} ; \quad H^{AB} = \begin{pmatrix} 0 & tf & 0 & 0 \\ tf^\dagger & 0 & \eta t' & 0 \\ 0 & \eta t' & 0 & tf \\ 0 & 0 & tf^\dagger & 0 \end{pmatrix} \quad (3.2)$$

where  $f = f(\vec{k})$  retains all the  $k$ -dependence of the Hamiltonian.

<sup>I</sup> When a more complex basis is used, all the *Slater-Koster* (SK) parameters will be scaled by the same factor so that the interlayer hopping among  $p_z$  orbitals is  $t' = 0.4$  eV in accordance with the literature.<sup>30</sup>

When  $\eta = 0$  the band structure is just that of graphene, but twofold, so at the  $K$  point there are 4 degenerate states.

For  $\eta > 0$  we will restrict ourselves to analyze the Hamiltonian at the  $\vec{k} = K$  point. In this point the  $\vec{k}$  dependence vanishes  $f(K) = 0$ . So the complete Hamiltonian [eq. 3.2](#) reads:

$$H^{AA}(K) = \eta \begin{pmatrix} 0 & 0 & t' & 0 \\ 0 & 0 & 0 & t' \\ t' & 0 & 0 & 0 \\ 0 & t' & 0 & 0 \end{pmatrix} ; \quad H^{AB}(K) = \eta \begin{pmatrix} 0 & 0 & 0 & 0 \\ 0 & 0 & t' & 0 \\ 0 & t' & 0 & 0 \\ 0 & 0 & 0 & 0 \end{pmatrix} \quad (3.3)$$

In the  $AA$ -stacking, every atom interacts with another atom from the other layer it is obvious from [eq. 3.3](#) that there will be no states in  $K$  at  $E = 0$  but rather two degenerate states at  $E = \pm t'$ .

In the  $AB$ -stacking only one of the atoms of each layer interacts via  $t'$ , at the  $K$  point two states will remain at  $E = 0$ , while the other will be shifted to  $E = \pm t'$ .

Since the  $AB$ -stacking is the most common one, and the most useful for our goals, we will focus the rest of the discussion in this kind of stacking.

### 3.1 BASIC DEFINITIONS

The description for the Bernal stacking is not much different from that of graphene: the with lattice vectors described by [eq. 2.2](#), hence the First Brillouin Zone (FBZ) is the same. The main difference is that the minimal basis now has four atomic positions.

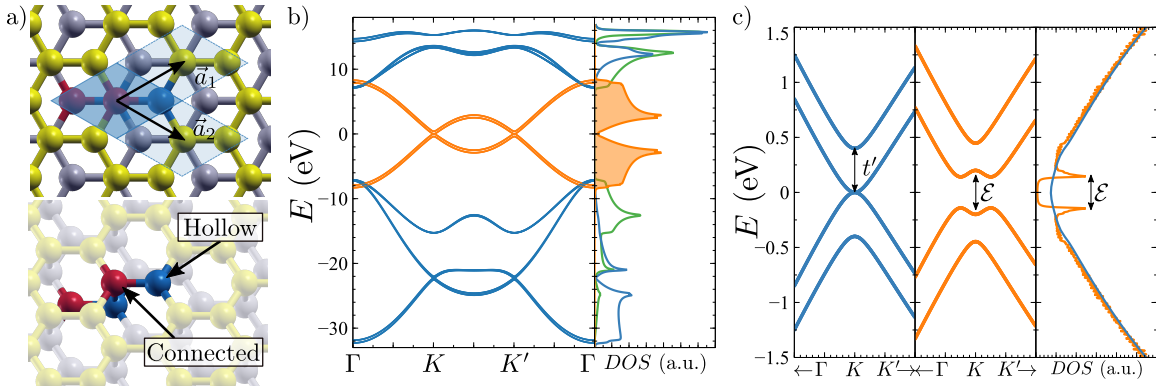


FIGURE 3.2: a) Cartoon depiction of the atomic structure of bilayer graphene using the lattice vectors defined in eq. 2.2 . b) Band structure of bilayer graphene. Notice the c) Comparison of the band structure and *Density of States* (DOS) in the presence of an external electric field.

In bilayer graphene the  $p_z$  manifold is no longer decoupled from the other orbitals since there are hopping processes between the  $p_z$  orbitals in one layer and the  $s$  orbitals in the other layer. Nevertheless the  $p_x$  and  $p_y$  still have no direct hopping with the  $p_z$  orbitals. While it is true that the symmetry protecting the  $p_z$  manifold is broken in this system, the fact remains that at low energy and around the  $K$  points the  $p_z$  description is enough (and exactly at the Dirac points it is an exact description).

### 3.2 ELECTRIC FIELD

It was early on discovered that the band structure of bilayer graphene changes dramatically in the presence of an external electric field.<sup>15–23</sup> The application of an electric field has several effects in the electronic structure of the system.

The most obvious effect is the different shift of the on-site energies for each layer. This effect breaks the bipartite-ness of the system and results in a tunable band gap as reported by many experiments.

Another effect is the possible doping of the system. By simply gating bilayer graphene we would be introducing a lot of carriers resulting in huge filling factors. This problem/feature can be address and, in fact, used to our advantage by using dual-gating rather than a single gate as we will see in the following sections.

Finally, the last effect is the appearance of a Rashba-like term due to the deformation of the atomic orbitals which could open both  $s - p_z$  hoppings and a spin flip channel (when combined with the *Spin-Orbit Coupling* (SOC)).

### 3.2.1 Gap opening

The effect of an electric field in the electronic structure is just a layer-dependent shift of the on-site energies of the atomic orbitals. In particular, in the basis eq. 3.1, the Hamiltonian at  $\vec{k} = K$  can be written as

$$H(K) = H^{AB}(K) + \mathcal{E}\Lambda = \begin{pmatrix} \mathcal{E} & 0 & 0 & 0 \\ 0 & \mathcal{E} & t' & 0 \\ 0 & t' & -\mathcal{E} & 0 \\ 0 & 0 & 0 & -\mathcal{E} \end{pmatrix} \quad (3.4)$$

where  $\Lambda$  is the layer operator and  $\mathcal{E}$  the strength of the electric field. From this equation it is clear that at the Dirac points there will be two states at  $E = \pm\mathcal{E}$  and two other states at  $E = \pm\sqrt{\mathcal{E}^2 + t'^2}$ , resulting in a gap  $\Delta = 2\mathcal{E}$ . Nonetheless the actual gap of the system occur not exactly at  $K(K')$  but in its vicinity, although the value is quite close to  $\Delta$  and its dependence with  $\mathcal{E}$  is the same.

This is a trivial gap although it is known that there is a finite Berry curvature of opposite sign in each of the valleys, and one could even define a valley-dependent Chern number<sup>74,75</sup>  $\mathcal{C} = K \operatorname{sgn}(\mathcal{E})$  being  $K = \pm 1$  the valley number. For this reason bilayer graphene is known as a weak topological insulator although, in fact, the spectrum is always gaped.

In particular, a band gap is open at the Dirac points as shown in Fig. 3.2 c). Along with this effect, there are other processes not captured by the model, for instance a strong redistribution of the charge will take place in the system, polarizing the two layers in opposition to the applied electric field. This screening process has been addressed in the literature showing that its main effect is a Hartree renormalization of the gap.<sup>15,76</sup> While these effects are certainly not negligible we can adopt an empirical approach based on the experimental observation<sup>18,19</sup> of a gap up to  $\Delta = 250$  meV, regardless of the real voltage required to achieve it.

### 3.2.2 Electric control of the charge density

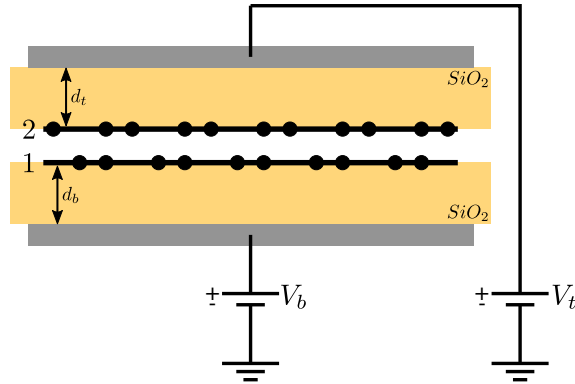


FIGURE 3.3: Schematics of dual gating.

The application of external fields will result, in general, in a modification of the charge density of graphene, governed by the Gauss' law:

$$\vec{\nabla} \vec{D} = \rho - \rho_0 = \rho_f \quad (3.5)$$

where  $D = E/\epsilon$ , where  $E$  is the electric field and  $\rho$  is total charge density,  $\rho_0$  is the bounded charge density so that  $\rho_f$  is the free charge density.

The dual-gating setup can be considered as an infinite parallel plate capacitor, hence, the electric field only has  $z$  component, hence the divergence of the displacement results in a derivative which can be discretized:

$$\vec{\nabla} \vec{D} = \frac{\partial D}{\partial z} = \frac{D_t - D_b}{d_z} = \rho_f = e \frac{N}{V} \Rightarrow D_t - D_b = e \delta n \quad (3.6)$$

where  $N$  and  $V = Adz$  are the number of electrons and volume respectively ( $A$  is the area), and  $\delta n$  is the bidimensional density of electrons.

In order to calculate the potential difference between the two graphene layers, we can consider simply the average of the electric field inside the capacitor:

$$\Delta V = \langle \vec{E} \rangle \Delta z = \frac{E_t + E_b}{2} \Delta z = \frac{\Delta z}{2} \left( \frac{D_t}{\epsilon_t} + \frac{D_b}{\epsilon_b} \right) \quad (3.7)$$

where  $\Delta z$  is width of the graphene bilayer and  $\epsilon_t$  and  $\epsilon_b$  are the electric permeability of the top and bottom dielectrics.  $D_t$  and  $D_b$  are (the  $z$ -component of) the displacement fields in the top and bottom regions.

$$D_t = \frac{\epsilon_t}{d_t} (V_t - V_t^0) \quad ; \quad D_b = \frac{\epsilon_b}{d_b} (V_b - V_b^0) \quad (3.8)$$

where  $V_{t/b}^0$  are the off-set potential required to have charge neutrality, usually referred to as Charge Neutrality Point (CNP).

Equations eq. 3.6 and eq. 3.7 show that by choosing the appropriate  $V_t$  and  $V_b$  we can independently change the carrier density of the system and the gap opened in the band structure.

### 3.3 TOPOLOGY AND KINK STATES

Similar to the monolayer case, in bilayer graphene the SOC opens a gap in the band structure at the  $K(K')$  points. This gap, in principle, could also have the same topological nature and indeed each of the layers present edge states, but these edge states are susceptible to gap opening under spin-mixing perturbations<sup>77</sup> giving them a “weaker” topological character. In particular, since the edge states are not Kramers-protected against backscattering, any hopping process involving the SOC once and inter-layer  $p_z$ - $s$  hopping twice is guaranteed to open a gap. This topic is discussed in appendix C.

There are other interesting scenarios leading to “edge” states in this system, though. The electric field,  $\mathcal{E}$ , is known to induce a valley-dependent Chern number  $C = K \text{ sgn}(\mathcal{E})$ , where  $K = \pm 1$  labels the valleys<sup>74,75</sup> so when an electric field of different sign is applied in different regions of the system,<sup>74,78–81</sup> the interface becomes the frontier of two regions with a different value for their topological invariant. Transition from one to another is only possible by closing the gap, which is exactly what the edge-states do. This phenomenon has been experimentally observed,<sup>80</sup> and the calculation is not complex to make as we show in the following lines.

We consider a *Two Dimensional* (2D) sheet of bilayer graphene and apply an electric field  $\mathcal{E} > 0$  for atomic positions with  $x > 0$  and  $\mathcal{E} < 0$  otherwise as depicted in Fig. ?? a). Equivalently we can consider the following Hamiltonian term:

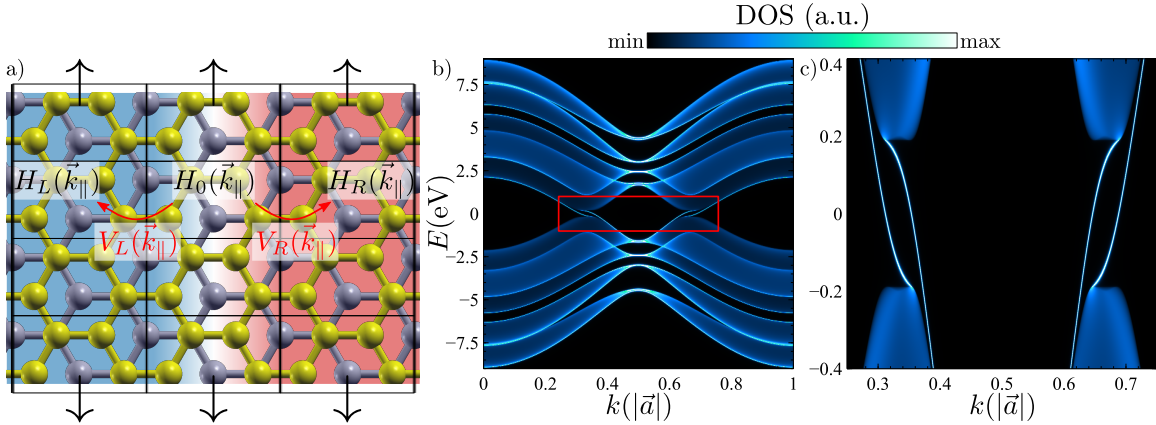


FIGURE 3.4: a) schematic of the system hosting kink states. b) DOS over the whole Brillouin Zone. c) Zoom around the Dirac cones.

$$H(x < 0) = \begin{pmatrix} \mathcal{E} & 0 & 0 & 0 \\ 0 & \mathcal{E} & 0 & 0 \\ 0 & 0 & -\mathcal{E} & 0 \\ 0 & 0 & 0 & -\mathcal{E} \end{pmatrix} ; \quad H(x > 0) = \begin{pmatrix} -\mathcal{E} & 0 & 0 & 0 \\ 0 & -\mathcal{E} & 0 & 0 \\ 0 & 0 & \mathcal{E} & 0 \\ 0 & 0 & 0 & \mathcal{E} \end{pmatrix} \quad (3.9)$$

Naturally, the wave functions of the conduction/valence states will be opposed in the two asymptotic limits of  $x \rightarrow \pm\infty$ , and when they approach  $x = 0$  they should somehow reverse so both ends and meet smoothly in the middle.

We will consider this  $2D$  system as an infinite collection of *One Dimensional* ( $1D$ ) systems coupled by some hopping. Each of this  $1D$  systems is infinite itself and it can be defined a  $k$ -moment along its axis:  $k_{\parallel}$ , and the hopping between these **1D!** (**1D!**) systems will also be  $k_{\parallel}$ -dependent.

With such a system we can write the Green's function for the interface:

$$G(E, k_{\parallel}) = \frac{1}{E + i\epsilon - H_0(k_{\parallel}) - \Sigma_R(k_{\parallel}) - \Sigma_L(k_{\parallel})} \quad (3.10)$$

where  $\epsilon$  is a small analytic continuation and each self-energy  $\Sigma_{\alpha}$  with  $\alpha \in \{L/R\}$  can be calculated by solving iteratively the coupled equations:

$$\begin{aligned} \Sigma_{\alpha}(E, k_{\parallel}) &= V_{\alpha}(k_{\parallel})g_{\alpha}(E, k_{\parallel})V_{\alpha}^{\dagger}(E, k_{\parallel}) \\ g_{\alpha}(E, k_{\parallel}) &= \frac{1}{E - H_{\alpha}(k_{\parallel}) - \Sigma_{\alpha}(E, k_{\parallel})} \end{aligned} \quad (3.11)$$

Once the self-energies are converged and the Green's function is calculated, the DOS can be obtained as usual:

$$\rho(E, k_{\parallel}) = \frac{-1}{\pi} \text{Im} [G(E, k_{\parallel})] \quad (3.12)$$

The resulting DOS depends both on the parallel moment  $k_{\parallel}$  and the energy at which we are looking, so the resulting graph is not to be considered as a X-Y plot but rather as a colormap for the energy-momentum with more (less) states.

The anticipated result is clearly seen in Fig. 3.4 b), where we can see the four edge states crossing the otherwise gaped spectrum.

### 3.4 SPIN PROXIMITY

Ever since the synthesis of graphene there has been a race to be able produce  $2D$  materials with different properties. A major milestone has been the synthesis of CrI<sub>3</sub>, a two dimensional ferromagnetic insulating material.<sup>82–84</sup>

This section is a brief summary of our publication [85] where we consider the proximity effect of  $\text{CrI}_3$  on bilayer graphene. In particular we consider bilayer graphene sandwiched by two layers of  $\text{CrI}_3$  as shown in Fig. 3.5 a), with the possibility of having the upper and lower  $\text{CrI}_3$  layers in a parallel (FM) or antiparallel configuration (AF).

This system shows a very different low energy spectrum depending on the relative orientation of the magnetic layers. In particular, in the AF configuration the bilayer graphene develops a gap becoming an insulator while for the FM configuration there is a Fermi surface and the conductance remains finite. This mechanism acts as an effective valve which can allow or prevent the flow of spin current.

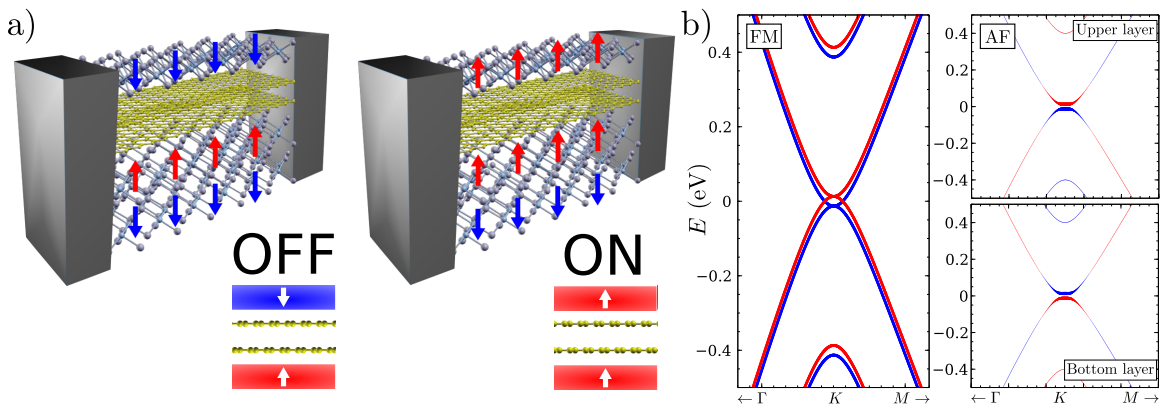


FIGURE 3.5: a) Scheme of the proposed system in the two possible configurations: antiparallel (AF) when the upper and lower  $\text{CrI}_3$  layers are antiferromagnetically aligned and parallel (FM). In the FM configuration there would be conduction through the bilayer graphene. In the AF configuration there is a gap in the spectrum. b) Band structure of the toy model for the system, the color denotes the spin, in the AF case the size of the dots is proportional to the layer polarization (the states are very layer and spin polarized in the top and bottom of the valence and conduction bands).

The realistic system ( $\text{CrI}_3$ -BG- $\text{CrI}_3$ ) is very complex. Close to the Fermi Energy four bands coming mostly from the  $d$  orbitals of the Cr meet the “Dirac parabola” of the bilayer graphene. The details of the DFT calculations can be checked in the published paper,<sup>85</sup> but we will restrict ourselves now to the minimal toy model that reproduced the physics observed in the real system.

Our toy model focuses on the effective Hamiltonian for the bilayer graphene, so our starting point will be the usual Hamiltonian eq. 3.2 . The effect of a magnetic layer in its proximity would appear in the Hamiltonian as a spin-

dependent on-site energy shift. For simplicity rather than duplicating the size of the Hamiltonian we will keep a  $4 \times 4$  Hamiltonian but make it spin-dependent. The effective Hamiltonian for the spin channel  $\sigma$  then reads:

$$\mathcal{H}_\sigma(\vec{k}) = \begin{pmatrix} \eta\sigma\frac{\Delta}{2} & tf(\vec{k}) & 0 & 0 \\ tf^*(\vec{k}) & \eta\sigma\frac{\Delta}{2} & t' & 0 \\ 0 & t' & \sigma\frac{\Delta}{2} & tf(\vec{k}) \\ 0 & 0 & tf^*(\vec{k}) & \sigma\frac{\Delta}{2} \end{pmatrix} \quad (3.13)$$

where  $\Delta$  is the effective strength of the magnetization of the nearby  $\text{CrI}_3$  layer,  $\sigma$  is the spin and  $\eta$  is a parameter to switch between the FM ( $\eta = 1$ ) and AF ( $\eta = -1$ ) configurations.

The resulting bands for this Hamiltonian are shown in Fig. 3.5 b) with the color representing the spin of the electrons. For the sake of readability, in the AF case, band structure of each layer has been separated and the size of the points has been made proportional to the layer polarization, showing that the top of the valence band and bottom of the conduction band are both spin and layer polarized in each of the layers.

The nature of the gap open by the proximity of the  $\text{CrI}_3$  layers is very similar to the case of the electric field.

The spin-valve function of this system becomes apparent when considering the possibility of pinning down the magnetization of one of the  $\text{CrI}_3$  layers (for instance, as shown in Fig. 3.5 a), by proximizing it with another  $\text{CrI}_3$  layer) and flipping the other with an external magnetic field. By flipping one of the  $\text{CrI}_3$  layers we could transition from the conducting FM band structure to the insulating AF one.

Analogously to previous section we can think of a scenario in which there is a domain wall between two AF regions with opposite magnetizations.

**Extracted from paper**



In the case of the spin valve in the AF state, this leads to Chern numbers that are both spin and valley dependent:

$$C = K\sigma \quad (3.14)$$

Based on eq. 3.14 we can anticipate<sup>74,75</sup> the emergence of one-dimensional spin-dependent chiral in-gap states in domain walls separating two antiferromagnetic domains with opposite magnetizations [Fig. 3.6 b)]. In order to verify this, we compute the momentum resolved density of states of a domain wall along the zigzag direction as illustrated in Fig. 3.6 b)

The domain wall is assumed to be abrupt, preserving spin collinearity. The calculation is done for a system with translational invariance along the wall direction, and embedded between two semi-infinite gaped graphene bilayer planes,

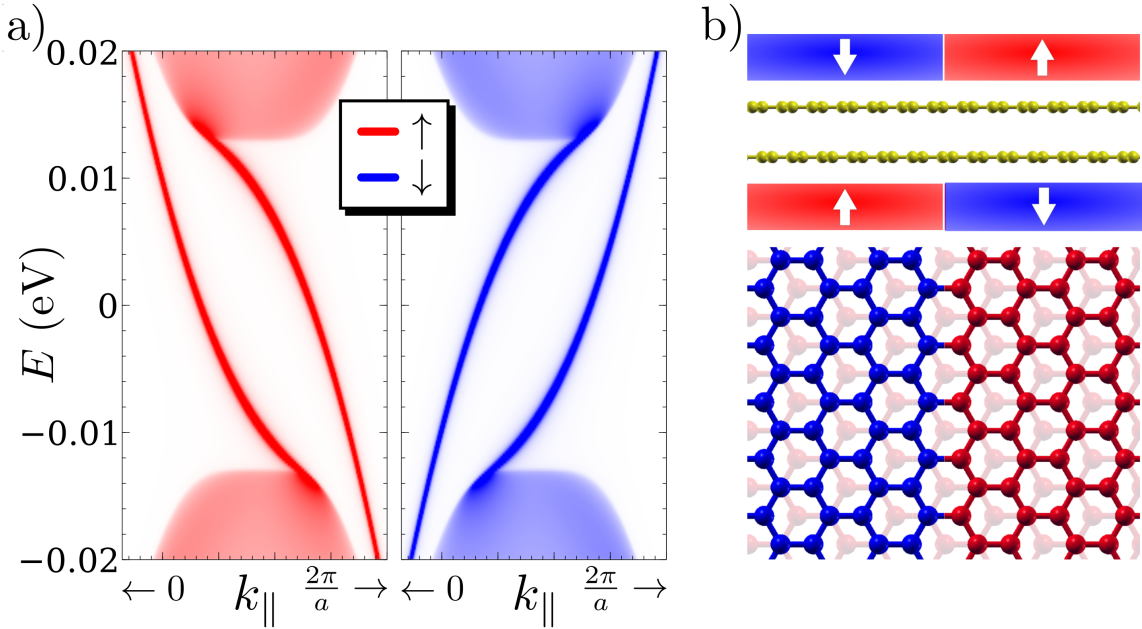


FIGURE 3.6: a) Up and down channels for the kink states. Since the interface presents a zigzag edge both Dirac cones lie on top one another, the separation by spin helps distinguish both channels. b) Sketch of the system.

using a Green's function technique.<sup>86</sup> Both domains are insulating, but at each valley the Chern number is opposite for a given spin direction. Thus, a domain wall along the zigzag direction, that preserves the valley, features two chiral 1D in-gap states per valley and per spin [see Fig. 3.6 a)]. It is interesting to note that, for a given valley, the states are spin chiral and therefore back-scattering requires either spin mixing, or intervalley scattering. A non-collinear domain wall might result in spin mixing

Until here

# Anomalous magnetism of $sp^3$ defects on graphene 4

---

So far we have reviewed the properties of both graphene and graphene bilayer. It is time now to study the effects of the addition of chemisorbed adatoms which bond strongly with the  $p_z$  orbitals of the C atoms. This chapter follows our paper on the “Anomalous magnetism in hydrogenated graphene”.<sup>87</sup>

The addition of an impurity atom into an otherwise non-magnetic crystal can result in the formation of local magnetic moments. It is one of the central problems in condensed matter physics,<sup>88</sup> although it is well understood in a couple of scenarios.

In the case of metals, the appearance of local moments is controlled by the addition energies of the impurity levels and their broadening, due to quasi-particle tunneling in and out of the impurity,<sup>88,89</sup> which depends on the *Density of States* (DOS) at the energy of the localized level.

In the case of insulators and semiconductors, the impurity level lies inside a gap. As a result, the unpaired electronic spin behaves like a paramagnetic center with  $S = 1/2$ .<sup>90</sup>

Graphene is usually referred to as a zero-gap semiconductor, meaning that it does not have a Fermi surface like metals do, but it also does not have a gap like semiconductors do. This middle point between metal and semiconductor makes graphene as a very peculiar system. For instance, very early on it was proposed that, in the dilute regime where only a few atoms are chemisorbed, hydrogenated graphene could create  $S = 1/2$  local moment<sup>91–96</sup> associated with the formation of an  $E = 0$ , or mid-gap, state that hosts an unpaired electron, turning graphene into a magnetic material with spin-dependent transport properties suitable for spintronics.<sup>97–100</sup> In contrast, in the dense limit, where

most of the C atoms are hydrogenated, it leads to the opening of a large band-gap.<sup>24,101</sup> In addition, recent *Scanning Tunneling Microscope* (STM) experiments<sup>25</sup> match the computed theoretical DOS as a function of both energy and position, that shows a split resonance close to the Dirac point, which could be indirect evidence for local moment formation.

#### 4.1 ADATOM VS. VACANCY

When atomic hydrogen is chemisorbed in graphene it forms a strong covalent bond between the  $p_z$  orbital and the hydrogen  $s$  orbital. This bond results in the appearance of a pair of bonding-antibonding states which lies far from the Fermi energy, roughly at  $E = \pm t_{H-C} \sim \pm 8\text{ eV}$  (see Table 2.7). When interested in low energy phenomena, only the  $p_z$  orbitals are relevant as seen in chapter 2. Using such a description, graphene is reduced to a honeycomb lattice (triangular lattice + 2-atom basis), with one orbital per atom. If we focus on the energy levels of graphene, upon chemisorption, one of the states originally at  $E = 0$  will be shifted into a combination of states at  $E \sim \pm 8\text{ eV}$  effectively removing it from the lattice of  $p_z$  sites.

In other words, in the low energy limit, the chemisorption of hydrogen atoms is equivalent to having vacancies in the honeycomb lattice formed only by the  $p_z$  orbitals. This picture is widely accepted and experimentally supported.,<sup>94,102–105</sup> and it is valid not only for chemisorption of atomic hydrogen, but for a large variety of other  $sp^3$  adsorbates.<sup>96</sup> Notice that these vacancies are simply vacancies in the  $p_z$  manifold and not real vacancies in graphene (i.e. missing atoms). The real vacancies bring along huge changes and deformations in the lattice that affect the whole spectrum of the system.

Keeping a 4-orbital description of the system would keep the bonding-antibonding states available for study, but the computational overhead is not worth it when we just want to study effects near the Fermi level.

$sp^3$  defects have also structural consequences. In particular it is well known both theoretically and experimentally that this bonding pulls the C atom away from its plane, forcing what is called a  $sp^3$  deformation, hence the name. This local lattice distortion induced by the  $sp^3$  hybridization enhances the effect of the spin-orbit interaction.<sup>106,107</sup> This has been proposed as the explanation for the observation of large spin Hall angles in hydrogenated graphene.<sup>108</sup> Resonant scattering with the zero mode resonance has also been considered as a source of enhanced quasi-particle spin relaxation in graphene.<sup>109–111</sup>

## 4.2 A VACANCY IN GAPLESS GRAPHENE

In gaped graphene structures, such as graphene with a spin-orbit gap,<sup>112</sup> graphene nanoribbons,<sup>94</sup> or a planar aromatic hydrocarbon molecules, the formation of an in-gap  $E = 0$  state due to  $sp^3$  functionalization trivially leads to a local moment formation with  $S = 1/2$ , very much like it happens for acceptors and donors in semiconductors. The zero energy state is singly occupied by one electron that occupies a bound state. The rest of this chapter is devoted to study the case of a  $sp^3$  chemisorption in infinite, pristine, gapless graphene. In that situation, the formation of a local moment is not warranted. Whereas the  $E = 0$  state appears exactly at the energy where the DOS vanishes, a finite DOS due to the Dirac bands is infinitesimally close, and its wave function, described with  $\psi \propto \frac{1}{x \pm iy}$  is a quasi-localized non-normalizable state.<sup>102</sup> The DOS of the resonant state diverges at  $E = 0$  and hence lacks a Lorentzian line-shape. This situation is genuinely different from conventional magnetic impurities in metals, that are coupled to a bath with finite DOS and show conventional Lorentzian line-shapes and it is also different from the situation in which the resonant state lies inside a proper gap.

The common approach to this problem usually relays in the use of supercells, where translational symmetry is preserved.<sup>25, 91, 93, 95, 113, 114</sup> Hence, this method does not directly study the desired system but rather it considers a periodic array of defects, in the hope that for big enough cells one could consider each defect as isolated. Actually, in this case the bands of such a system will always present a gap with an impurity band in it. Such a band, at half filling, will always result in a quantized  $m = 1\mu_B$  magnetic moment since all the valence bands would be doubly occupied but only one of the two states in the gap would be occupied.

While this approach has been proven very useful in many studies, it does not strictly solve the problem of a single impurity in an otherwise pristine graphene sheet.

To tackle this problem we use two different methodologies. On the one hand, we make a Green's function description of the defected region embedded into an infinite pristine crystal which yields an exact description, but results in computationally relatively expensive calculations. On the other hand, we use the Kernel Polynomial Method (KPM) which allows the calculation of spectral properties for huge systems (800000 atoms) in a computationally efficient way, but has the drawback of lower resolution in energy.

### 4.3 METHODS

In the following, we describe graphene with a one orbital tight-binding model as described by the basis eq. 2.4. Electron-electron interactions are described within the Hubbard approximation. Thus, the energy scales in the Hamiltonian are the first neighbor hopping  $t$  and the Hubbard on-site repulsion  $U$ . When an external magnetic field is introduced it is considered to be an in-plane magnetic field  $B$  coupled only to the spin degree of freedom. The effect of  $sp^3$  hybridization is included by the removal of both a site in the honeycomb lattice and one electron, as discussed above.

We use two different techniques to tackle the problem of a single impurity in pristine graphene. The first one consists in the calculation of the (exact) Green's function for a region close to the defect by means of the Dyson equation, using an embedding method described below. The second one is the Kernel Polynomial Method (KPM), that allows the calculation of spectral properties of extremely large systems with minimal computational effort.

#### 4.3.1 *The embedding technique*

We first present a general method to study single impurities in infinite systems, from now on referred as embedding technique.<sup>115</sup> Since a single defect in an infinite system breaks the translational symmetry, we cannot use a Bloch description. Instead, we describe the system in terms of Green's functions, making use of the Dyson equation.

We start by dividing the system into two regions, a central unit cell  $A$  containing the defect, and the rest of the system  $B$ , containing everything else, as depicted in Fig. 4.1 (b). The Hamiltonian of the whole (infinite) system can then be written in terms of the two separated contributions, one arising from each isolated region,  $H_0$ , and the other arising from the coupling between the two regions  $W$ :

$$H = H_0 + W = \begin{pmatrix} H_A & 0 \\ 0 & H_B \end{pmatrix} + \begin{pmatrix} 0 & V_{AB} \\ V_{BA} & 0 \end{pmatrix} \quad (4.1)$$

The Green's function corresponding to region  $A$  can be written (exactly) as:

$$G_A(E) = \frac{1}{E + i\eta - H_A - \Sigma_{AB}(E)} \quad (4.2)$$

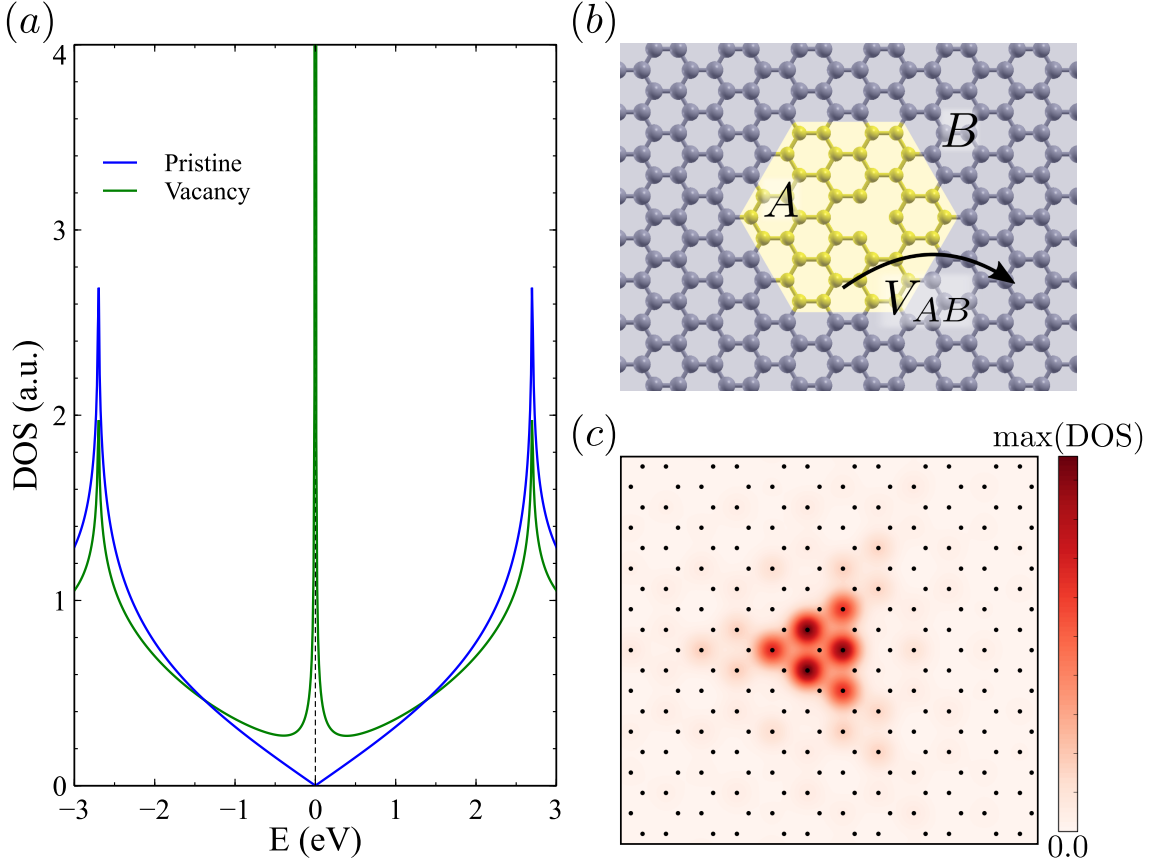


FIGURE 4.1: (a) Total density of states of a single vacancy in an infinite graphene sheet. A divergence in the density of states appears at  $E = 0$  when the vacancy is introduced. (b) Scheme of the division of the system into a defected unit cell and a pristine environment. (c) Local Density of States for the zero energy state related to a vacancy in graphene. Side by side we can compare the calculations for two unit cells with different geometry. The vacancy is depicted as a white circle. As expected the spatial distribution of this state is located in the 3-6 closest atoms to the vacancy.

where the *embedding self-energy*  $\Sigma_{AB}$  can be calculated from the Green's function of region  $B$ :

$$\Sigma_{AB}(E) = V_{AB} g_B(E) V_{BA} \quad \text{with} \quad g_B(E) = \frac{1}{(E + i\eta - H_B)} \quad (4.3)$$

For numerical reasons  $\eta$  has to be finite but we checked that the results do not depend on its exact value. We found that  $\eta = 0.001$  offers a good combination of precision in energy while keeping the convergence time of the Dyson equation reasonable. In general the Green's function  $g_B(E)$  for region  $B$  is not straightforward to calculate, as  $g_B(E)$  describes the Green's function of

an infinite system without translational symmetry, on account of the missing region  $A$ . However, the calculation of  $\Sigma_{AB}$  is made possible when we consider two facts. First,  $\Sigma_{AB}$  does not depend on whatever is in region  $A$ , second, equation eq. 4.2 holds true for a pristine system with translational invariance, that permits to compute  $G_A(E)$ , and evaluate  $\Sigma_{AB} = E - H_A - (G_A(E))^{-1}$ .

The evaluation of  $G_A(E)$  is now done by dividing the infinite pristine crystal system into periodic supercells  $A'$  of the same size and shape as the defect region  $A$ . The Green's function of region  $A'$  in the perfect crystal can thus be calculated by integrating the  $\vec{k}$ -dependent Green's function in the whole Brillouin zone

$$G_{A'}(E) = \frac{1}{(2\pi)^2} \int_{\text{BZ}} (E + i\eta - H(\vec{k}))^{-1} d^2\vec{k} \quad (4.4)$$

with  $\vec{k}$  the Bloch wavevectors and  $H(\vec{k})$  the Bloch Hamiltonian for the pristine host crystal. The final expression for the self-energy  $\Sigma_{AB}$  reads:

$$\Sigma_{AB}(E) = E + i\eta - H_{A'} - \underbrace{\frac{1}{(2\pi)^2} \left( \int_{\text{BZ}} (E + i\eta - H(\vec{k}))^{-1} d^2\vec{k} \right)^{-1}}_{1/G_{A'}(E)} \quad (4.5)$$

where  $H_{A'}$  describes a region with the same dimensions than the original defective region  $A$ , but without the defect(s). This is a general procedure and can be applied for multi-band Hamiltonians. As long as the dimensions of the pristine and the defected Hamiltonian are the same, it can deal with more than one defect without computational overhead. Notice that this method does not require the analytic evaluation of the host crystal Green's function necessary in a recently proposed method,<sup>116</sup> and can be applied to a very large class of systems, including superconductors.<sup>117</sup>

The combination of equations eq. 4.2 and eq. 4.5 allows the computation of the Green's function of the defective area,  $G_A$ , embedded in an otherwise pristine crystal as shown in Fig. 4.1. The DOS of an atom  $i$  in region  $A$  can then be calculated from the imaginary part of the Green's function as

$$\rho_i(E) = -\frac{1}{\pi} \text{Im} [G_{i,i}(E)] \quad (4.6)$$

where  $G_{i,i}$  is the diagonal matrix element  $(i, i)$  of the Green's function. Summing over the contributions from all atoms  $i$  in region  $A$ , the total DOS of region  $A$  is obtained.

In Fig. 4.1 we show the results of the method for the case of a single vacancy in the honeycomb lattice. Fig. 4.1 (a) shows the density of states both for pristine

graphene, that shows the characteristic  $\rho \propto |E|$  around the Dirac point,<sup>118</sup> and for the defective case, that presents a diverging zero energy resonance. The embedding method permits also the calculation of the local density of states as shown in Fig. 4.1 (c), where we show the map of the density of states evaluated at  $E = 0$ , finding that the main contribution for this state comes from the 3-6 nearest neighbors to the vacancy that belong to the sublattice opposite to the one of the missing site.<sup>94, 102–105</sup> Of course, for the case of a non-interacting single vacancy, this problem can be dealt with using the standard T matrix theory.<sup>104, 112, 119</sup> The embedding method shows its added value when it comes to treat several vacancies or when interactions are included, as we discuss now.

#### 4.3.2 Mean field Hubbard model

The Hubbard term acting on every site  $i$  reads:

$$H_U = U \sum_i n_{i,\uparrow} n_{i,\downarrow} \quad (4.7)$$

where  $n_{i\sigma}$  is the standard number operator for site  $i$  with spin  $\sigma$ . Exact solutions of this model are, in general, not possible to obtain so that we use a mean field approximation:

$$H_U \approx \sum_i U \left[ \langle n_{i,\uparrow} \rangle n_{i,\downarrow} + \langle n_{i,\downarrow} \rangle n_{i,\uparrow} - \langle n_{i,\downarrow} \rangle \langle n_{i,\uparrow} \rangle \right] \quad (4.8)$$

where  $\langle n_{i,\sigma} \rangle$  stand for the expectation values of the number operators computed with the eigenstates of the mean field Hamiltonian. Of course, this is a non-linear problem that is solved self-consistently. Here, this is done in combination with the two dimensional embedding technique, which is formally similar to the one dimensional case.<sup>120</sup> In this approach, the occupations in the external region  $B$  are frozen to  $\langle n_{i,\uparrow} \rangle = \langle n_{i,\downarrow} \rangle = \frac{1}{2}$ . In contrast, the expected values of the defective cell are calculated by self-consistent iteration.

In a first step, we assume a random guess spin polarization and then compute the expected values of the spin operators  $\langle n_{i,\sigma} \rangle$  by integrating the DOS up to the Fermi energy

$$\langle n_{i,\sigma} \rangle = \int_{-\infty}^{E_F} \rho_\sigma(E) dE \quad (4.9)$$

which defines a new Hamiltonian for region  $A$ ,  $H_A \rightarrow \bar{H}_A + H_U^{MF}$ , including the mean field Hubbard term.<sup>94, 121</sup> Notice that the numerical integration of eq. 4.9 is much more efficiently done in the complex plane using Cauchy's integral theorem. Also it is important to notice that even when the Hamiltonian for the region  $A$  will change over the self-consistent iterations the self-energies will

not since they do not depend on what is inside of said region. This procedure is iterated until a self-consistent solution is found.

There is a trade off between computational cost, due mainly to the size of the region  $A$ , and the accuracy of the description of the semi-localized nature of the induced magnetism. The role of the chosen size for region  $A$  is discussed bellow.

Finally, the magnetic moment is calculated as the difference of the expected values of each spin densities.

$$\langle m(i) \rangle \equiv g\mu_B \frac{\langle n_{i,\uparrow} \rangle - \langle n_{i,\downarrow} \rangle}{2} \quad (4.10)$$

#### 4.3.3 The kernel polynomial method

The Kernel Polynomial Method (KPM)<sup>122</sup> is a spectral method that allows to calculate spectral properties of very large matrices without explicit diagonalization or inversion of the matrix. This makes the method especially suitable for very large systems described by sparse Hamiltonians, as is the case for the first neighbor hopping model for the honeycomb lattice, considered here. In our case, we set up the Hamiltonian for an extremely large graphene island, with a single vacancy in the center.

The Chebyshev polynomials form a complete basis in the function space, so that they can be used as a basis to expand any well behaved function  $f(x)$  for  $x \in (-1, 1)$ . The method consists in expanding the density of states in  $N$  Chebyshev polynomials  $T_n(x)$ , that are calculated using  $T_0(x) = 1$ ,  $T_1(x) = x$  and the recursive relation

$$T_{n+1}(x) = 2xT_n(x) - T_{n-1}(x) \quad (4.11)$$

valid for  $x \in (-1, 1)$ .

The first step in the method is to scale the Hamiltonian  $H \rightarrow \bar{H} = \sum_k \bar{E}_k |k\rangle \langle k|$  so that all the eigenstates  $\bar{E}_k$  fall in the interval  $\bar{E}_k \in (-1, 1)$ . The density of states as a function of the scaled energy, at site  $i$ , is expressed as

$$\rho_i(\bar{E}) = \frac{1}{\pi\sqrt{1-\bar{E}^2}} \left( \bar{\mu}_0 + 2 \sum_{n=1}^{N-1} \bar{\mu}_n T_n(\bar{E}) \right) \quad (4.12)$$

The coefficients  $\bar{\mu}_n$  are the modified coefficients of the expansion,

$$\bar{\mu}_n = g_n^N \mu_n \quad (4.13)$$

that are obtained using the Jackson kernel<sup>123</sup>

$$g_n^N = \frac{(N-n-1) \cos \frac{\pi n}{N+1} + \sin \frac{\pi n}{N+1} \cot \frac{\pi}{N+1}}{N+1} \quad (4.14)$$

that improves the convergence of the expansion. The original Chebyshev coefficients are calculated as a conventional functional expansion

$$\mu_n = \int_{-1}^1 T_n(\bar{E}) \sum_k \delta(\bar{E} - \bar{E}_k) |\langle k | i \rangle|^2 = \langle i | T_n(\bar{H}) | i \rangle \quad (4.15)$$

with  $|i\rangle$  the wave function localized in site  $i$ . Importantly, the second equality in eq. (4.15) relates  $\mu_n$  to an expression where the eigenstates  $|k\rangle$  of  $H$  are absent. Thus, diagonalization of  $H$  is not necessary and the computation of the  $\mu_n$  coefficients only requires calculating an overlap matrix element involving  $T_n(H)$ . The Chebyshev recursion relation allow to write down the  $\mu_n$  coefficients in term of the overlaps with the vectors  $|\alpha_n\rangle$

$$\mu_n = \langle \alpha_0 | \alpha_n \rangle \quad (4.16)$$

generated by the recursion relation

$$\begin{aligned} |\alpha_0\rangle &= |i\rangle \\ |\alpha_1\rangle &= \bar{H}|\alpha_0\rangle \\ |\alpha_{n+1}\rangle &= 2\bar{H}|\alpha_n\rangle - |\alpha_{n-1}\rangle \end{aligned} \quad (4.17)$$

In our case, we will choose a state,  $|i\rangle$ , localized in the first neighbor of the carbon with the hydrogen ad-atom. To calculate the previous coefficients we only need matrix vector products, so that the scaling is linear with the size  $L$  of the system, in contrast with the  $L^3$  scaling for exact diagonalization. Our calculations are performed in a graphene island with 800000 atoms, taking a expansion with  $N = 10000$  polynomials.

#### 4.4 NON INTERACTING ZERO TEMPERATURE MAGNETIZATION

In this section we study the spin polarization in the neighborhood of a  $sp^3$  defect, driven by an external in-plane magnetic field coupled to the electronic spin, at zero temperature and in the non-interacting limit  $U = 0$ . In a gapped graphene system, this problem is straightforward. At  $T = 0$ , the spin density would be dominated by the contribution of the only singly occupied state, the  $E = 0$  mid-gap state, whose wave function we denoted by  $\psi_0(i) \equiv \langle i | \psi_0 \rangle$ . The zero temperature magnetization in an atom  $i$  would be given by:

$$m_i(B) = g\mu_B \left( \Theta(B) - \frac{1}{2} \right) |\psi_0(i)|^2 \quad (4.18)$$

where  $B$  is the magnitude of the magnetic field,  $\Theta(B)$  is the step function,  $g \simeq 2$  is the gyromagnetic ratio and  $\mu_B$  is the Bohr magneton. The local

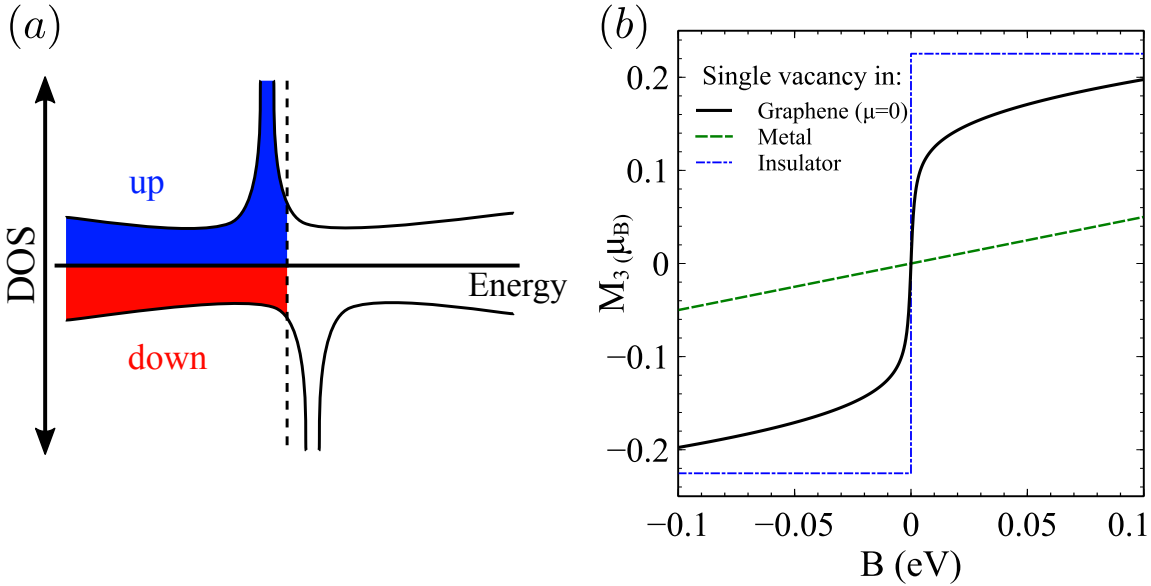


FIGURE 4.2: (a) Sketch for the Zeeman split DOS associated to graphene with an individual  $sp^3$  functionalization. Panel (b) shows the magnetization of the first 3 neighbors of the defect as a function of the applied magnetic field for a hydrogen atom in a graphene quantum dot (blue) and a single hydrogen atom in pristine graphene (black), the green line is the result for a conventional metal, modeled by graphene with the chemical potential well above the Dirac point.

magnetization  $m_i$  is stepwise constant, and discontinuous at  $B = 0$ ,  $m_i(0^+) - m_i(0^-) = g\mu_B|\psi_0(i)|^2$ . It is apparent that the total moment  $M = \sum_i m_i$  integrates to  $M = \pm \frac{g\mu_B}{2}$  on account of the normalization of the wave function of the mid-gap state. This result holds true as long as the Zeeman energy  $\mu_B B$  is smaller than the gap of the structure.

We now study what happens in the case of infinite pristine graphene, for which there is no gap, and we cannot define a normalized zero energy state. For that matter, we compute the density of states of the system using the Green's function embedding approach. This method is trivially adapted to include the Zeeman splitting that introduces a rigid spin dependent energy shift  $\pm\mu_B B$ . This symmetric shift allows the expression of all the spectral functions for each of the spin channels in terms of the spinless Green's function,  $G^\sigma(E) = G(E - \sigma\mu_B B)$ , with  $\sigma = \pm 1$ .

The results for the magnetization of the three first neighbors of a  $sp^3$  defect in an otherwise pristine graphene are shown in Fig. 4.2 for a single  $sp^3$  defect in two scenarios. A gapped finite size graphene hexagonal island with armchair edges, resulting in the expected step-wise response, a single defect in otherwise pristine

gapless graphene. In both cases we plot the magnetization of the three atoms closest to the vacancy,  $M_3 = \sum_{i=1}^3 m_i$ , that gives the dominant contribution to the defect-induced local moment. The result for the paramagnetic response of a metal is included in Fig. 4.2 for comparison with a standard case.

The most prominent feature of the obtained results is the fact that the  $M_3(B)$  curve is not stepwise constant for the defect in infinite graphene, in marked contrast with the case of the defect in a gapped system. This difference shows the qualitatively different behavior of the zero mode in gapless infinite graphene, compared to the standard case of an in-gap truly localized state. The *continuous variation* of the magnetic moment can be related to the fact that the zero mode has an intrinsic line-width that reflects the lack of a gap to host a true localized state.

#### 4.5 FINITE TEMPERATURE SUSCEPTIBILITY

We now discuss the effect of temperature on the non-interacting  $m(B)$  curve. The only effect of temperature is to smear out the occupation of the one-particle levels, so that the expected value of the local magnetization has to include now excited states.

To calculate the magnetization in a site  $i$  as a function of the magnetic field and the temperature we just need to compute the difference in the occupation of the spin-up and spin-down density of states weighted with the Fermi-Dirac distribution function. Thus, the local magnetic moment is given by  $m_i = g\mu_B \langle s_z(i) \rangle$  with

$$\langle s_z(i) \rangle = \frac{1}{2} \int_{-\infty}^{\infty} [\rho_{i\uparrow}(E) - \rho_{i\downarrow}(E)] f(E, T) dE \quad (4.19)$$

where  $f(E, T)$  is the Fermi Dirac distribution and  $\rho_{i\sigma}(E)$  is the spin resolved density of states. The resulting magnetization of the three closest atoms,  $M_3$  is shown in Fig. 4.3 (a), computed with two different approaches, the embedding method for a single  $sp^3$  defect in infinite graphene and the KPM for a single defect on a finite size island with a very large number of atoms. It is apparent that both methods give identical results in the chosen range of temperatures.

In order to highlight the anomalous behavior of the magnetic moment associated to an individual  $sp^3$  defect, we focus on the spin susceptibility, defined as

$$\chi(T) = \left. \frac{\partial m(T)}{\partial B} \right|_{B=0} \quad (4.20)$$

For  $T = 0$  the results of the previous section show that this quantity diverges, both for the gapped and gapless cases. Here we study the dependence of  $\chi(T)$

as a function of temperature  $T$ . For a conventional local moment, the zero field susceptibility follows the Curie law  $\chi(T) \propto T^{-1}$ . This result holds true, based on very general considerations, for any spin governed by the Hamiltonian  $g\mu_B \vec{S} \cdot \vec{B}$  as well as any classical magnetic moment  $\vec{M}$  governed by the interaction energy  $-\vec{M} \cdot \vec{B}$ . In particular, the Curie susceptibility of a single electron in an in-gap level will follow a Curie law.

Numerical derivation of the results of Fig. 4.3 (a) allows the calculation of  $\chi(T)$ , shown in Fig. 4.3 (b) in a Log-Log representation. It is apparent that the spin susceptibility for the  $sp^3$  defect on graphene *does not follow* the Curie law. In particular, we obtain a high temperature power law dependence  $\chi \propto T^{-\alpha}$ , with  $\alpha \sim 0.77$ , in comparison with the conventional  $\alpha = 1$ . This exponent reflects, again, the anomalous nature of the  $sp^3$  local moment in infinite graphene, in marked contrast with the behavior of the same chemical functionalization in a gapped graphene structure. Interestingly,  $\chi(T)$  has been measured<sup>124</sup> for defective graphene obtaining a Curie law dependence, probably because the samples used are in fact nanoflakes with small confinement gaps that permit the existence of in-gap states with quantized spins.

Further insight into the magnetic properties of this system is obtained by considering the dependence of the magnetic susceptibility as a function of the graphene chemical potential, that could be modified by gating doping,<sup>125</sup> as shown in Fig. 4.3 (c,d). The maximal local susceptibility is obtained at half-filling and small temperatures where it monotonically decreases both with temperature and doping. In comparison, in the case of slightly doped samples, the magnetic susceptibility can either increase or decrease as a function of the temperature, showing a maximum at a doping-dependent temperature. The previous behavior can be understood as a crossover from the impurity in an insulator to the metallic regime. Importantly, the local maximum implies that graphene doping introduces an energy scale that determines the temperature for the impurity-metal crossover. In the case of heavily doped samples ( $\mu = 81$  meV), the susceptibility grows monotonically with temperature, signaling the conventional metallic regime.

## 4.6 EFFECT OF INTERACTIONS

We now study the effect of electron-electron interactions in the formation of local magnetic moments associated to the  $sp^3$  functionalization. A single unpaired electron in an in-gap energy level has a spin  $S = 1/2$  (equivalent of a magnetic moment  $m = 1\mu_B$ ). In the current study this is not the case, the  $E = 0$  resonance is embedded in a region with finite DOS (except in just one

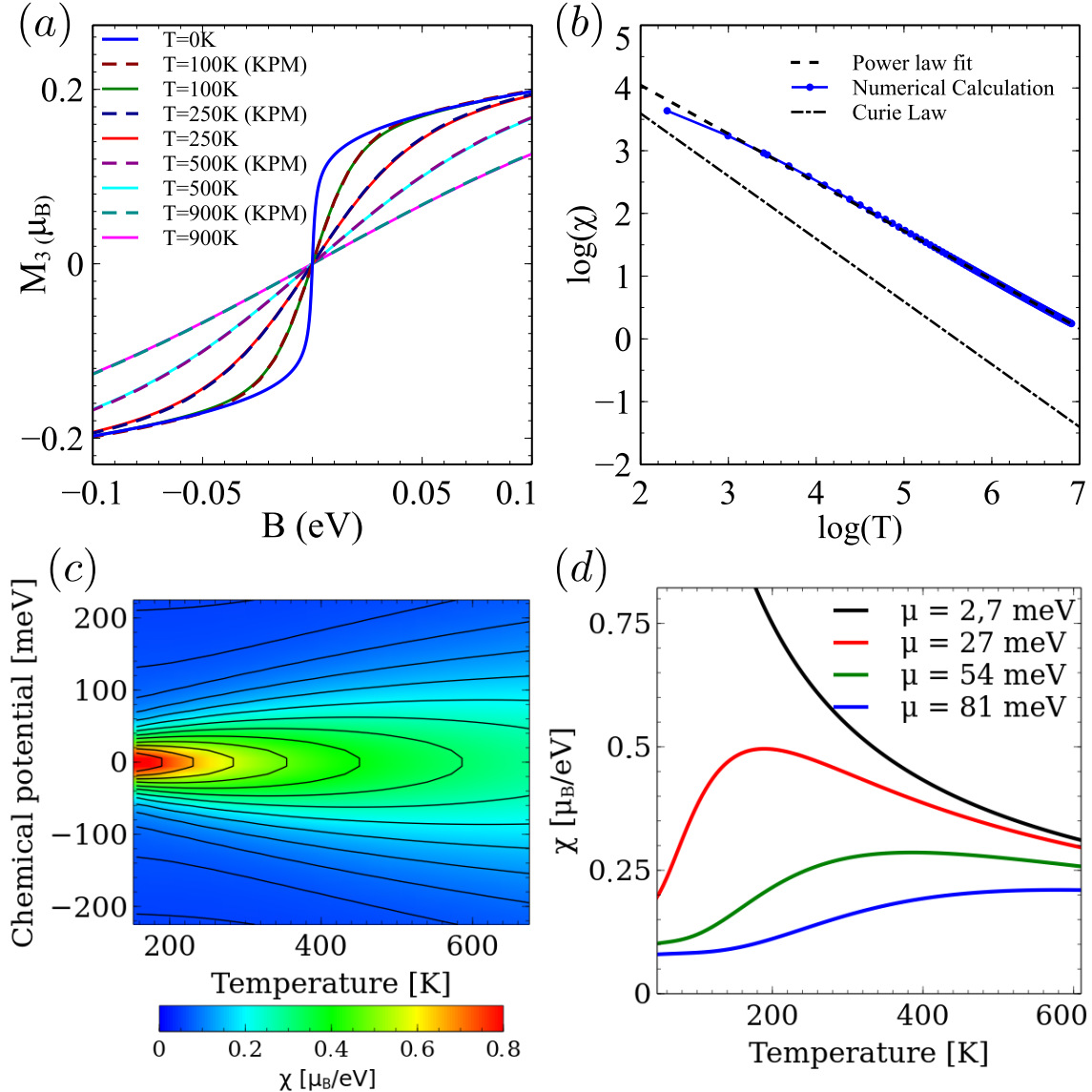


FIGURE 4.3: (a) Magnetization of the first 3 neighbors of the vacancy as a function of the applied magnetic field for different temperatures, dashed lines are calculated using the KPM and continuous lines are calculated using the embedding method. (b) Temperature dependence of the susceptibility in comparison with Curie's Law. (c-d) Dependence of the susceptibility with the doping and the temperature, showing that for some values of  $\mu$  there is a non-monotonous behavior of the susceptibility with temperature.

point, the Dirac energy) and the existence of an emergent magnetic moment follows the Stoner criterion  $U\rho(E_F) = 1$ . For graphene with a single  $sp^3$  defect the diverging nature of  $\rho(E)$  at  $E = 0$ , the presence of arbitrarily small

interactions gives rise to a local moment. However, because of the coupling of the mid-gap state to a continuum of states (the linear bands of graphene) it is not obvious a priori whether or not the local moment should have a quantized  $S = 1/2$  spin. In the following we address this issue, using the mean field approximation for the Hubbard model and the embedding technique as discussed in previous sections. The Hubbard model, while is not certainly the complete description of such a system, offers a simple model to gain an insight on the possible magnetic solutions for the systems.

#### 4.6.1 Local magnetic moment

In general, the results of the mean field calculation yield a non-zero magnetization above rather small values of  $U$ . However, the integrated local moment  $M = \sum_{i \in A} m_i$  is far below the quantized value of  $M = 1\mu_B$ . A characteristic snapshot of the magnetization density computed for a simulation cell with 162 atoms within the mean field Hubbard model is shown in Fig. 4.4 (a). The dominant magnetic moments appear in the sublattice opposite to the one of the defect, but small contributions of opposite sign appear in the same sublattice. The influence of the coupling to infinite graphene is neatly shown in a calculation where we artificially tune the intensity of the interaction between the central simulation cell  $A$ , and the rest of graphene. For that matter, we define the following modified full Green's function

$$\widetilde{G}_A^\lambda(E) = \frac{1}{E + i\eta - \widetilde{H}_A - \lambda_\Sigma \Sigma_{AB}(E)} \quad (4.21)$$

where  $\lambda_\Sigma \in [0, 1]$  is a control parameter that smoothly interpolates between limit where the region  $A$  is decoupled ( $\lambda_\Sigma = 0$ ) from the rest of the universe, quantum dot regime, and the infinite-crystal regime ( $\lambda_\Sigma = 1$ ).

As it is shown in Fig. 4.4 (b), in the quantum dot regime  $\lambda_\Sigma = 0$  the magnetic moment is quantized  $M = 1\mu_B$ . However, as soon as the unit cell is coupled to the rest of the graphene,  $\lambda_\Sigma \neq 0$ , the magnetic moment rapidly becomes non-quantized, with an evolution that depends on the size and geometry of the region  $A$ .

As soon as  $U$  is larger than a small critical  $U \simeq 0.01t$ , magnetic solutions are obtained and we find that the non integer nature of the magnetic moment holds for a wide regime of electronic interactions  $U$ . The net magnetic moment is an increasing function of  $U$  as well as the size of the central region,  $N_C$ , Fig. 4.4 (c,d). Even for the largest simulation cells, with up to 288 sites, the total magnetic moment remains clearly below  $1\mu_B$ . However, a representation of the total moment as a function of  $N_C^{-1}$ , not shown, makes it hard to predict whether

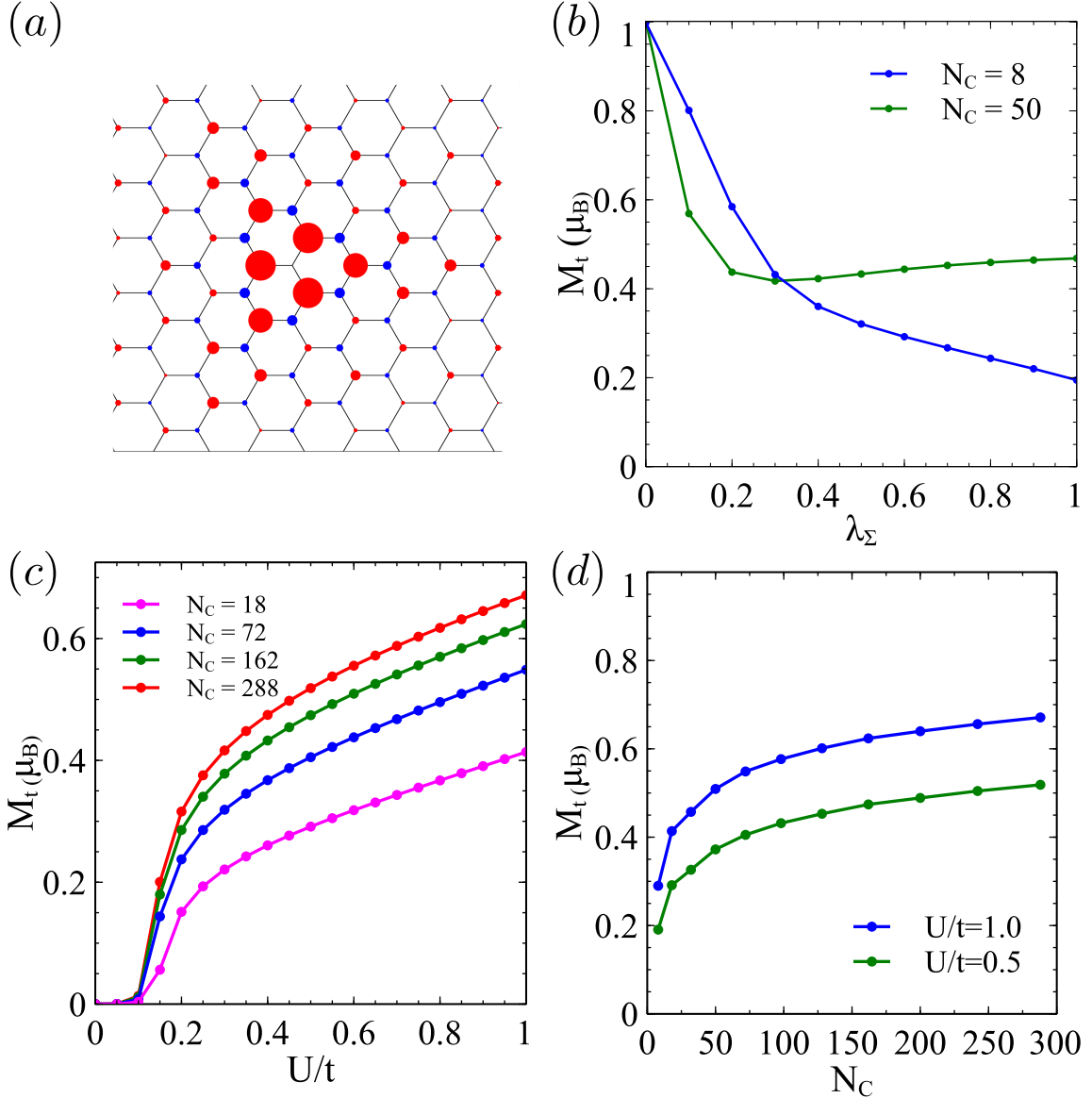


FIGURE 4.4: (a) Magnetization of an individual  $sp^3$  functionalized system, calculated within the mean field Hubbard approximation. (b) Total magnetization of the defected region as a function of its coupling to the rest of the otherwise pristine system. (c) Total magnetization of the defected region as a function of the Hubbard  $U$  for different sizes of the unit cells. (d) Total magnetization as a function of the size of the unit cell for two  $U$  values, notice that the magnetization is far from the expected  $m = 1\mu_B$  value.

or not the extrapolation to an infinite cell would recover the quantized value. Whereas it might be that the magnetic moment is quantized, our calculations emphasize the rather extended nature of this object.

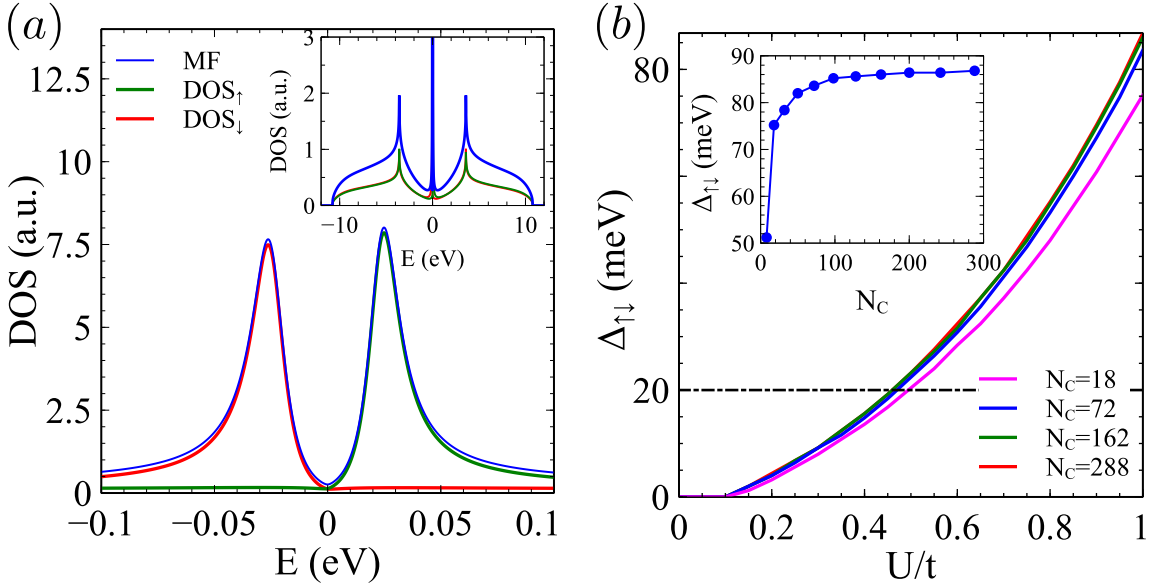


FIGURE 4.5: (a) total and spin-resolved DOS for the Hubbard model. (b) spin splitting,  $\Delta$  as a function of the Hubbard interaction  $U$  and, in the inset, as a function of the size of the unit cell.

#### 4.6.2 Spin splitting

Our magnetic self-consistent solutions spontaneously break symmetry and result in spin-split density of states, shown in Fig. 4.5. Importantly, the interacting DOS does not have any integrable singularity, as it happens for the  $U = 0$  case at  $E = 0$ . Summing over spin projections, the total density of states still shows electron-hole symmetry. However, the spin-resolved DOS is split, so for one spin projection the resonance is below the Fermi energy, while for the other one is above, which accounts for the net magnetization. We define the spin splitting,  $\Delta$ , as the difference in energy between these two resonances. We find that  $\Delta$  has a super-linear dependence on the Hubbard interaction  $U$ , as shown in Fig. 4.5 (b). This reflects the fact that the spin splitting is linear both in  $U$  and in the magnetic density  $m$ , which is also an increasing function of  $U$ . These results depend weakly on the size of the defective region,  $A$ , in the embedding calculation (inset of Fig. 4.5 (b)).

We now address the connection between the DOS in Fig. 4.5(a), that shows two spin-split peaks around the Fermi energy, and the STM  $dI/dV$  spectra reported by González *et al.*<sup>25</sup> Whereas the experimental  $dI/dV$  curve also shows two peaks, the interpretation of the experimental observations<sup>25</sup> requires some caution. The spin-split peaks in the mean field calculation arise from

the breaking of the spin symmetry. This band splitting does indeed occur in ferromagnetic systems large enough to keep the magnetization frozen along a given direction that defines a spin quantization axis that permits the definition of the spin orientation of the spin-split bands. The quantum fluctuations of this mean field picture can be safely neglected for a large enough magnetic moment, but this is definitely not the case of a system that, at most, has  $S = 1/2$ .

Therefore, the origin of the two peaks observed in the experiments<sup>25</sup> is *not* the spin splitting of the graphene energy levels, in line with the discussion Gonzalez *et al.*<sup>25</sup> A more correct interpretation of the split peaks is the following. The STM  $dI/dV$  is proportional to the spectral function of the surface, in this case, graphene. The spectral function of a localized level has two peaks, associated to the addition  $E > E_f$  and removal  $E < E_f$  of an electron in the system. Their energy difference is a measurement of the *addition energy* of the system, i.e., the Coulomb repulsion between the host localized electron and a second additional electron injected in the system. When the addition energy is larger than the temperature, as in the experiment, the system is in the so called Coulomb-Blokade regime. This entails the existence of an unpaired spin, very much like in the Anderson model<sup>88</sup> and does not preclude the emergence of Kondo effect at very low temperatures. The proper treatment of the addition energies in this system would involve solving the single impurity problem of a resonance in a Dirac bath in a many body framework,<sup>113,126,127</sup> which is out of the scope of the present work.

Finally, for a truly localized level with wave function  $\phi_0$ , described with the Hubbard model, both the addition energy and the mean field spin-splitting are roughly given by  $U \sum_i |\psi_0(i)|^4$ . Therefore, even if the spin-splitting of the mean field theory is conceptually different from the addition energy observed experimentally, these two quantities roughly described by the same formula.

#### 4.6.3 Localization

Our calculations show that magnetic moment associated to a hydrogen ad-atom is delocalized in more than 250 carbon atoms. In this sense, our calculations highlight the anomalous nature of the resonance due to a single  $sp^3$  impurity in contrast to the phenomenology in gapped systems. This behavior arise from the special condition of the DOS, (null only in exactly one point) and the absence of an energy scale able to confine the  $E = 0$  resonance.

It is worth noting that in real graphene some effects not captured by the first neighbor Hubbard model that can play a relevant role. First, the existence of second neighbor carbon hopping breaks electron-hole symmetry and shifts

the vacancy state away from  $E = 0$ . Second, single hydrogenation introduces an effective on-site energy in the carbon atom that is actually finite, although rather large, which also leads to a displacement of the resonance away from zero energy. Third, non-local electronic interaction in graphene may have a sizable effect on the magnetic moment. And finally, spin-orbit coupling would open a gap of around  $0.03\text{meV}$ .<sup>128</sup> Whether any of the previous perturbations would be capable of moving the system to the conventional quantum dot regime would require a careful study with a first principles Hamiltonian, which is out of the scope of the present work.

#### 4.7 CONCLUSIONS

We have addressed the problem of the local moment formation induced by an individual  $sp^3$  functionalization in graphene, with chemisorbed atomic hydrogen as the main motivation. We model this within the single orbital Hubbard model, so that the functionalization is modeled as a vacancy in the honeycomb lattice. We have shown that the magnetic moment in this system departs from the conventionally accepted  $m = 1\mu_B$  picture. This relates to the fact that the lack of a gap in graphene prevents the existence of a standard in-gap state that can host an unpaired electron. Our calculations show that the local moment induced by  $sp^3$  functionalization in otherwise gapless and pristine graphene give rise to specific signatures in the magnetic response of the system, such as a non-Curie temperature dependence and a non-linear (and non-monotonic for some doping values) magnetic susceptibility. We have also shown by means of mean-field calculations that the resulting magnetic moment is non-quantized in the whole regime explored. Our results should pave the way for future work treating many-body spin fluctuations beyond mean field theory<sup>113, 126, 127</sup>

# $sp^3$ defect in Biased Bilayer Graphene

5

---

When a single vacancy is placed in graphene bilayer (or graphene, for that matter), the translational invariance is broken, so its description in terms of Bloch functions is not possible. The previously introduced embedding technique (see 4.3) provides a workaround in which we consider the defective part of the system to be restricted to a limited region while the rest of the system remains pristine. This approach is quite computationally expensive and while it provides a way to calculate the Green's function, it is not possible to obtain the wave function which will be necessary later on.

In order to retain the wave function information we are going to consider a finite hexagonal island with armchair edges. We will consider a big enough island so we can neglect the edge effects. The largest island will be 50.6 nm in diameter, containing 131772 atoms. Such a system will be our playground to explore the behavior of a single vacancy when an external electric field is applied.

## 5.1 A NOTE ON THE GEOMETRY

When only one vacancy is considered, it will be placed at the (hollow) atomic position closest to the center of the island in order to maximize the distance to the edges.

When two vacancies are considered, they will be placed as separated as possible from the edges, as shown in Fig. 5.1 b). This configuration (rather than placing one in the center, for instance) allows the study of a wider range of the

angle,  $\alpha$  and distance  $d$ . When more than two vacancies are considered, they will be placed in the vertices of a regular polygon centered in the island.

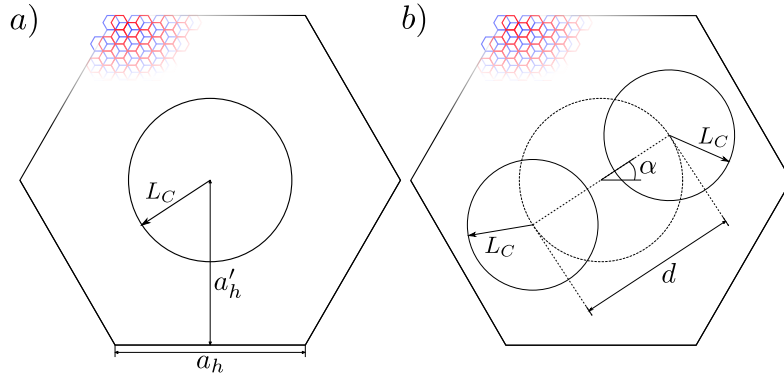


FIGURE 5.1: a) and b) show sketches of the position of the vacancies and relevant geometric information. In the upper left corner the real atomic structure is shown using blue for the lower layer and red for the upper one. The length  $L_C$  is the typical size of the in-gap state.

In the case of graphene monolayer, every atomic position is equivalent, so regardless of the position in which the adatom is introduced, the physical effect will be the same. This is not the case for AB-stacked bilayer graphene. In each layer one of the sublattices is connected to atoms of the other layer, while the other sublattice lays on hollow spaces.

## 5.2 TWO TYPES OF VACANCIES

There are two inequivalent sites to place an adatom in AB-stacked bilayer graphene shown in Fig. 5.2 a) and d). Depending on where the  $sp^3$  defect is placed we will refer them as being in a “hollow” or a “connected” site. The physics of the connected sites is explored elsewhere<sup>129</sup> and we will not study it any further than analyze the spectrum

As it is expected, in such a system the confinement gap decreases linearly with the area of the island (quadratically with the side), as shown in Fig. 5.3 a). It is worth noting that this model is doomed to break down when the scale of the electric field is comparable to the confinement gap. We shall, then, stay clear of the small electric field regime in order to avoid finite size effects.

In order to calculate

We can calculate the spectrum of the system with and without a vacancy in order to compare both of them. Of course the full diagonalization of a  $131772 \times 131772$  Hamiltonian is, at the very least, challenging for any standard

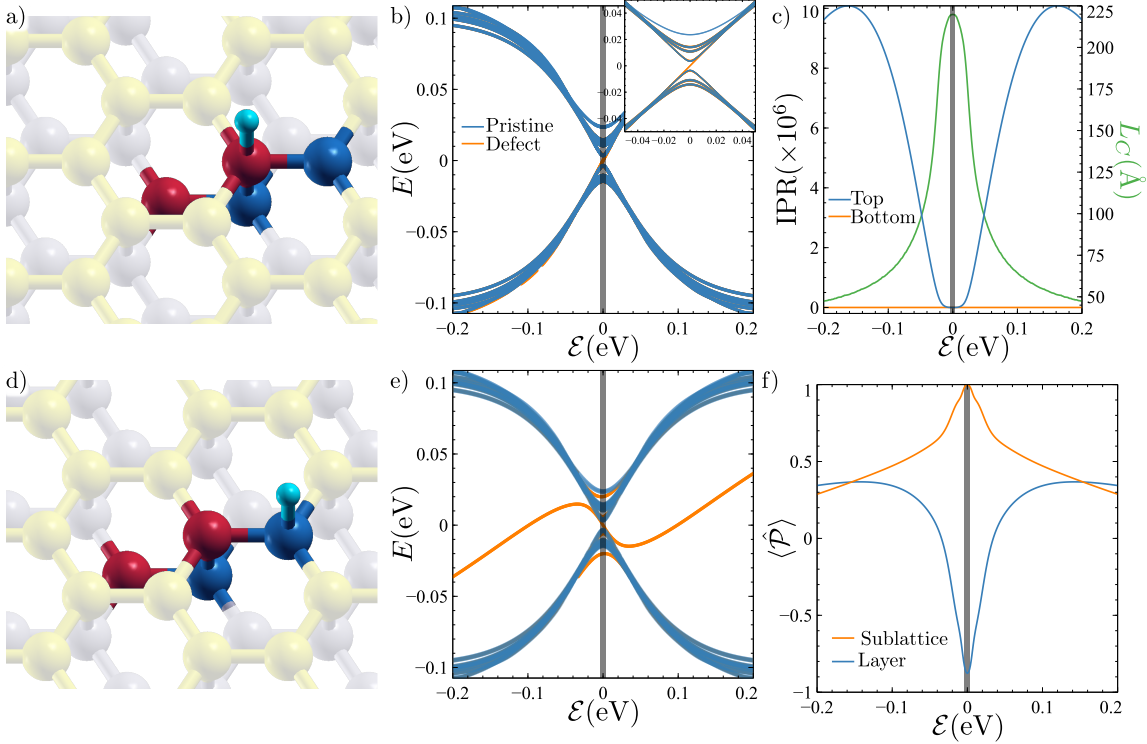


FIGURE 5.2: a,b) Evolution of the spectrum for adatom on a connected site. The in-gap state is shifted directly by the electric field with 100% sublattice and layer polarization, without noticing the bottom layer. Panels c-f) belong to an adatom on a hollow position. e) Evolution of the spectrum with the applied electric field. c) IPR and confinement length dependence on the electric field. f) Evolution of the layer and sublattice polarization as the system loses its bipartite character.

computer, so we will use Lanczos diagonalization<sup>130–132</sup> to obtain only the 9 eigenvalues closest to the Fermi energy.

As shown in Fig. 5.3 b) the main difference when the vacancy is introduced is that a state appears in the middle of the (confinement) gap. As a matter of fact there will appear as many in-gap states as vacancies are introduced.

When we analyze the in-gap state we see that it is 100% sublattice polarized, as predicted by the Lieb’s theorem.<sup>133</sup> Regarding the layer distribution, it is distributed in both layers but not equitably. Interestingly, the in-gap state has more spectral weight in **the layer that does not host the vacancy** and the bigger the island, the stronger this polarization is as shown in Fig. 5.3 d). We can check the spatial distribution of this state (see Fig. 5.3 c)) to see that it is actually quite localized in the top layer (red dots), but completely spread over the bottom layer (blue dots). The particular shape of the distribution of the bottom layer is strongly affected by the edges so it is not to be considered as a

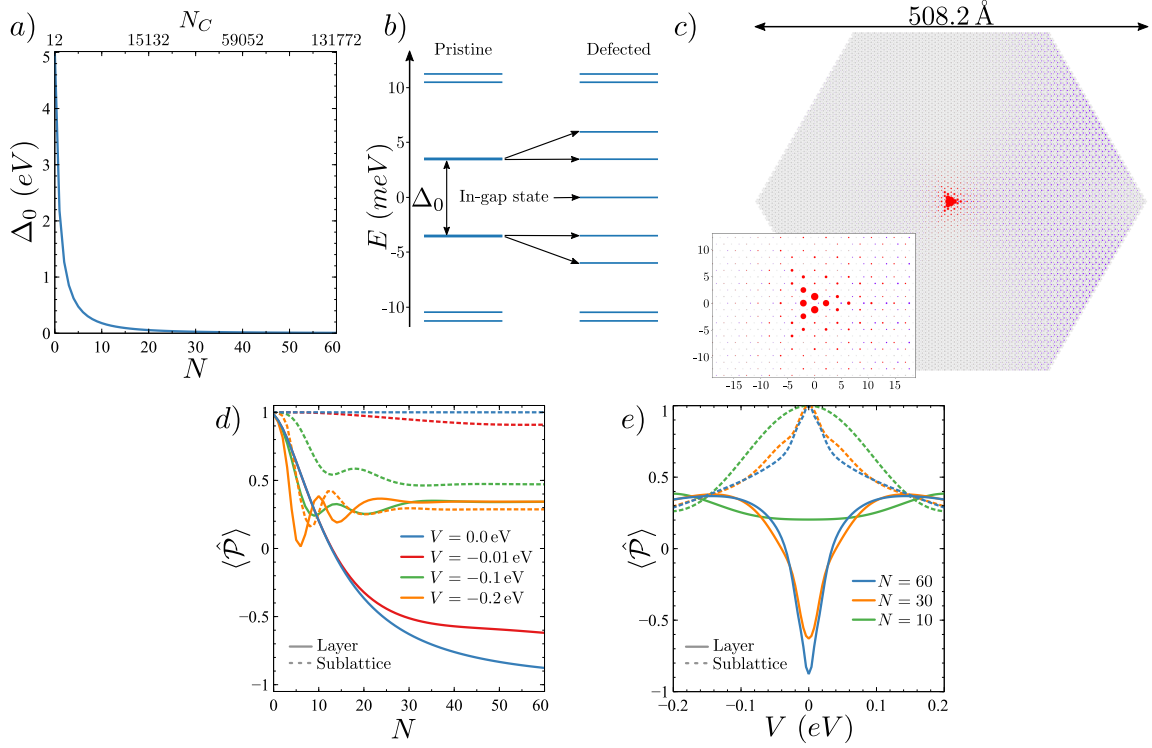


FIGURE 5.3: a) Confinement gap as a function of the size of the island (lower axis) and the number of carbon atoms  $N_C$  in the island (upper axis). b) Comparison of a pristine and a defected island, with a vacancy in the central hollow position. An in-gap state appears at zero energy. c) Spatial distribution of the in-gap state. It appears distributed in both the top (red dots) and bottom layer (blue dots). Notice that the state is strongly localized around the vacancy in the top layer (red) while it is spread throughout the bottom layer (blue). The spatial distribution of the bottom layer is affected by the finite size of the sample and its exact shape is but a minor detail. The inset shows a  $15 \times 10 \text{ \AA}$  zoom of the in-gap state around the vacancy. d) Dependence of the layer and sublattice polarizations with the size of the island. e) Evolution of the layer and sublattice polarizations with the electric field for islands of different size.

reliable result, nevertheless its spreading (calculated via IPR later) is consistent through different shapes and island sizes, and in accordance to the literature.<sup>129</sup>

### 5.2.1 Hollow sites

When an electric field is applied to bilayer graphene with a vacancy, the in-gap state will no longer be at zero energy. Instead, its position will shift with the electric field. As stated before, in a finite island we cannot define Bloch

vectors, so we do not have bands. Nevertheless we can plot the spectrum of the island for different electric fields next to each other, this way we can have a band-looking plot showing the smooth evolution of the energy levels with the external potential. In Fig. 6.4 we see the evolution of different properties

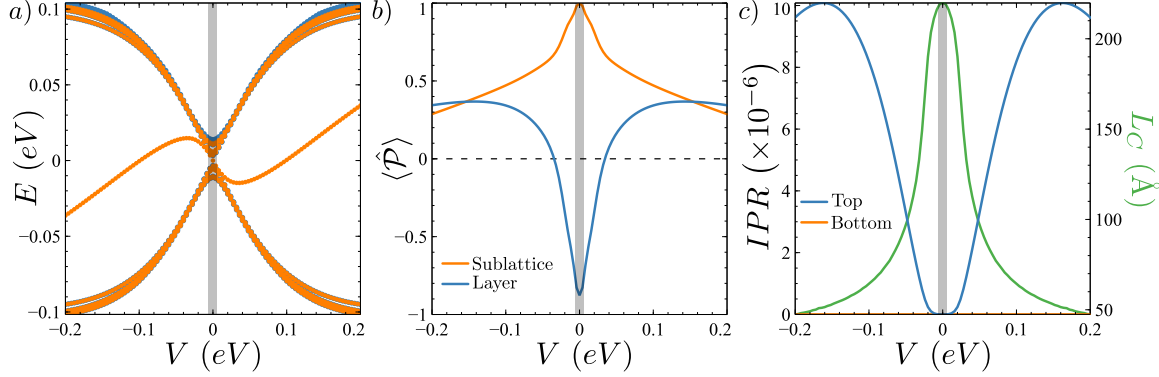


FIGURE 5.4: a) Evolution of the spectrum of an armchair island with the electric field. b) Sublattice and Layer polarization as a function of the electric field. c) Evolution of the IPR for the top (blue) and bottom layer (orange) and confinement length (green) with the electric field. Notice that the IPR for the bottom layer is very close to zero ( $IPR_b \sim 10^{-11}$ ) while the for the top layer it changes five orders of magnitude with the electric field, showing how much the in-gap state can be confined. Analogously the confinement length shows (right axis) that the state is spread all over the island for  $V = 0$  eV but it can be confined to  $\sim 50$  Å. The vertical gray strip in all panels shows the region where  $|V| \leq \Delta_0$ , where the edge effects can play a role.

with the electric field. Panel a) shows the deformation of the spectrum of the island with the electric field. The in-gap state appears consistently in the middle of the gap but its position does not change monotonously. There is an interplay between the charge polarization and the external electric field. As the electric fields becomes stronger, we can see that the in-gap state looses its initial polarization, Fig. 6.4 b), reaching a stable distribution between both layers and sublattices.

Another effect introduced by the electric field is the localization of the state. Fig. 6.4 c) shows the strong reduction of the confinement length,  $L_c$ , defined as:

$$0.98 = \int_{r_0}^{L_c} \Psi_0(r) dr \quad (5.1)$$

This non-standard definition gives an intuitive idea of how far from the vacancy (placed at  $r_0$ ) is most of the state (over 98% of it). It is interesting to notice that the inverse participation ratio, IPR, defined as:

$$|\Psi_0\rangle = \sum_{\beta} c_{\alpha} |\phi_{\alpha}\rangle \quad ; \quad \text{IPR} = \sum_{\alpha} |c_{\alpha}|^4 \quad (5.2)$$

behaves quite differently for the top and bottom layer. Let us keep in mind that the smaller the IPR, the more spread the state is, in the limit case in which a given state is equally spread over all the  $N$  available atoms, the IPR would be  $\text{IPR} = 1/N$ , while for a state localized in a single atom, it would be  $\text{IPR} = 1$ . For the bottom layer, the IPR is very small and it barely changes with the electric field. This shows an extended state no matter the applied electric field. That is not the case for the top layer. In the top layer the  $\text{IPR} \sim 0$  for very small electric fields, but it increases rapidly with the electric field, showing that the state gets quickly localized. This is also confirmed by looking at the confinement length (green line in Fig. 6.4 c) which begins at a huge value, comparable to the size of the island, and decreases to a few nanometers.

A first order perturbative calculation of the energy at which the in-gap state should appear yields

$$E_0(V) = V \langle \Psi_0 | \hat{L} | \Psi_0 \rangle \quad (5.3)$$

In order to understand the implications of this, let us consider a vacancy in the upper layer ( $\lambda_l = +1$ ). At  $V = 0.0 \text{ eV}$ , the in-gap state,  $\Psi_0$ , is quite layer-polarized:  $\langle \Psi_0 | \hat{L} | \Psi_0 \rangle \sim -0.8$ . When the electric field is switched on, the in-gap state shifts with a negative slope. Nevertheless the electric field opposes the starting polarization and eventually they cancel out, which results in a change of sign in the slope.

This behavior suggests a crossover between two interactions: the electric field and the kinetic terms. Let us study the effects of the interlayer coupling in this system.

### 5.2.2 Role of the interlayer coupling

Naively, one may expect the in-gap state to shift linearly with the electric field as, for instance, the conduction and valence states do. Nevertheless, the calculations show otherwise. For small electric fields (we will discuss this scale later on) the in-gap state moves in opposition to the electric field, as discussed in Fig. 6.4 a). For large electric fields the in-gap state does move linearly with the electric field, yet, the rate at what it does depends strongly on the interlayer

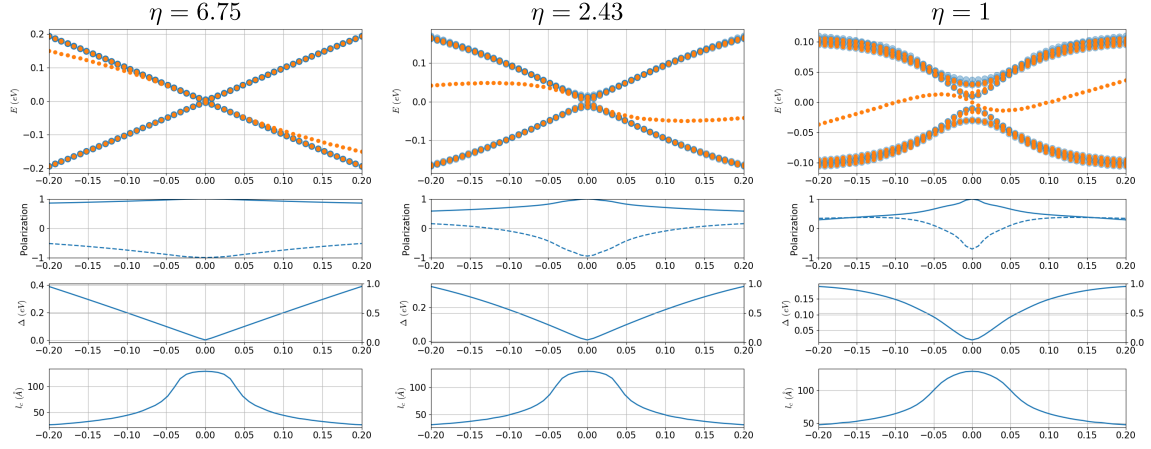


FIGURE 5.5: Evolution of the spectrum with the interlayer coupling. The left panel shows the spectrum if we consider interlayer interactions as strong as the intralayer ones. The right panel shows the realistic value and the central panel shows an intermediate situation.

coupling, as shown in Fig. 5.5 . We will consider the Hamiltonian of the system to be two graphene hamiltonians coupled by an interlayer interaction:

$$H = H_{L_1} + \eta H_{\text{inter}} + H_{L_2} \quad (5.4)$$

The intralayer  $\pi$ -hoppings are  $t = -2.7$  eV while the interlayer hoppings (which are  $\sigma$ -hoppings, due to the symmetry of the orbitals) are roughly  $t_{\text{inter}} = 0.4$  eV.  $\eta$  is an artificial adimensional parameter that will allow us to tune the interlayer coupling to study the behavior of the system. In this fashion,  $\eta = 1$  corresponds to normal, realistic GBL, while  $\eta = 0$  describes two decoupled graphene layers and, in particular,  $\eta = 6.75$  corresponds to having an *interlayer* coupling as strong as the *intralayer* one.

In order to understand the role of the interlayer coupling in the in-gap state, it is useful to plot the dependence of the layer polarization with the parameter  $\eta$ . We consider this parameter to range from 0.5 (slightly decouple) to 6.75 (strongly coupled so inter and intralayer hopping is the same).

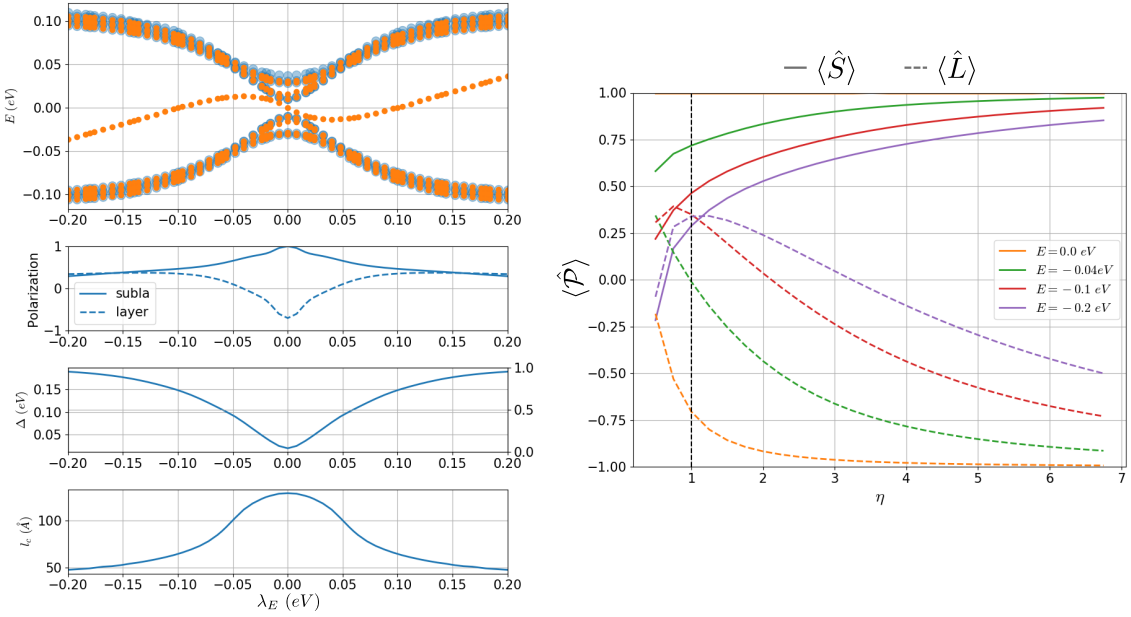


FIGURE 5.6: *a)* Evolution of different properties with the electric field. First panel shows the evolution of the spectrum, the second one shows the sublattice and layer polarizations, the third one plots the gap of the system and the forth one shows the confinement length. *b)* Evolution of the layer (dashed lines) and sublattice polarization (solid lines) with the interlayer coupling. Notice that at zero electric field,  $V = 0.0$  eV, the sublattice polarization remains constant at  $\langle \hat{S} \rangle = 1$ , as expected from the Lieb's theorem.

We can see that the electric field overcomes the interlayer contribution when the system reaches charge neutrality  $\langle \hat{L} \rangle = 0$ .

We can try to understand this step by step. When a H adatom is introduced (aka, a vacancy), one electron is localized in the vicinity of the defect. For an adatom chemisorbed on top of a C atom belonging to the sublattice -1 in the top layer (namely 1), the sublattice and layer polarization are:

$$\langle \hat{S} \rangle = 1 \quad ; \quad \langle \hat{L} \rangle = -0.7$$

This means that the in-gap state is completely sublattice polarized (as Lieb's theorem predicts) but it is only  $\sim 70\%$  layer polarized, meaning that the localized electron lives mostly **in the layer that does not contain the vacancy**.

If we artificially increase the value of the interlayer coupling we can see that the layer polarization consistently drops to lower values, showing that the in-gap state prefers to spread in the layer that does not contain the vacancy. Analogously, the evolution of the sublattice polarization also shows that the in-gap state gets more and more sublattice-polarized.

This behavior might be understood keeping in mind the behavior of a single vacancy in graphene. It is known that for a vacancy in graphene, the in-gap state is mostly concentrated in the three closest atoms. In graphene bilayer it happens that these three closest atoms are connected to the other graphene layer, so the stronger the interlayer coupling, the easier will be for the in-gap state to spread to the other layer.

What I do not understand is that the 3 atoms closest to the vacancy (containing most of the state at  $\eta = 0$ ) are connected to atoms of the opposite sublattice in the other layer, yet, the sublattice polarization seems to keep its expected flavor even when the interlayer coupling is heavily increased.

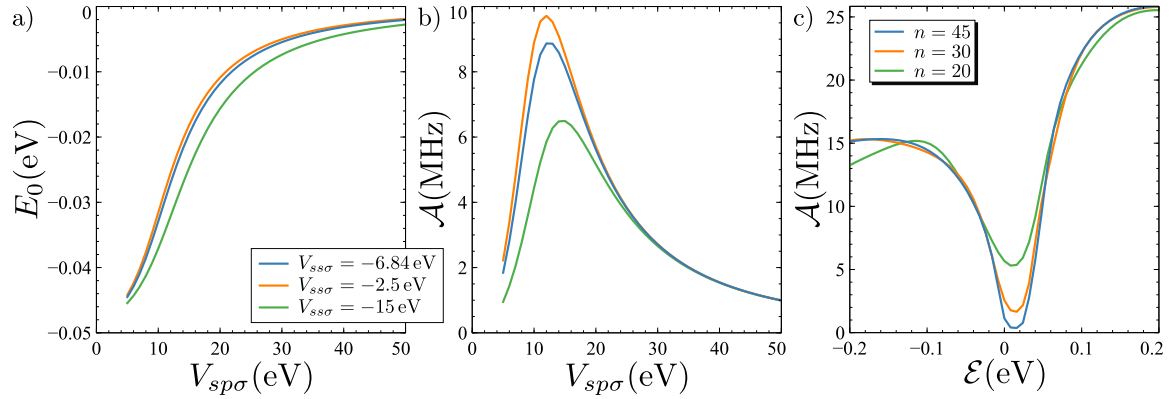


FIGURE 5.7: Change in the hyperfine coupling with the electric field.

# Hyperfine coupling

# 6

## 6.1 ADATOM IN THE SK-APPROXIMATION

While the model of an effective vacancy in the  $p_z$  manifold is very simple and useful, it lacks some ingredients that can also provide interesting physical effects.

We are going to discuss briefly here the implementation of this system in a *Slater-Koster* (SK) framework as described in previous chapters. This approximation will provide some insight in the physics of the other orbitals.

The most naive approach would be to use the SK parameters detailed in previous chapters (see table 2.7). These parameters were calculated for  $H$  atoms passivating the edges of graphene nanoribbons<sup>64</sup> where the main hybridization occurs with the  $\sigma$  orbitals of graphene. There is no good reason why these hoppings parameters should hold for an adatom on top of flat graphene. For the sake of the argument we will start with those values in order to spot the difference with the idealized one-orbital model, and then proceed to consider the hopping parameters as somehow free parameters that we can tune.

In a first approach we are going to neglect the well known  $sp^3$  deformation of the lattice and consider simply that the  $H$  atom has some hoppings to the  $C$  orbitals. Due to the symmetry of the problem, both the  $s$  and  $p_z$  orbitals will have a finite hopping with the  $s$  orbital while  $p_{x/y}$  will not. In the SK approximation, the effective hoppings will be governed by the parameters  $V_{ss\sigma}$  and  $V_{sp\sigma}$ .

When only one orbital per site is considered, graphene is a bipartite lattice. The effective removal of one of the sites results in the appearance of a zero energy state. In fact, Lieb's Theorem<sup>133</sup> determines that the imbalance in the number of sites of each sublattice equals the number of zero-energy states:  $N_Z = |N_A - N_B|$ .

The introduction of more orbitals in the description breaks the bipartite character of the lattice since the on-site energy of  $s$  and  $p$  orbitals is not the same. Even when, strictly speaking, Lieb's Theorem does not apply, the actual behavior does not change drastically. Usually, the introduction of an adatom will open a small gap and the states that appear are usually not at zero energy, but they do appear inside the gap. The confinement properties described in 4 do hold.

## 6.2 DEPENDENCE ON THE PARAMETERS

In Fig. 6.1 a) we show the differences in the spectrum when considering 1 and 4 orbitals per atom. The calculations were carried out by considering a big hexagonal island ( $N_C > 100000$ ) with armchair edges (passivated by  $H$  atoms when 4 orbitals are considered) and a single  $H$  adatom placed in its center. The main difference is the energy at which the in-gap state appears. Due to the symmetry of the orbitals and the symmetrical position of the adatom, there are only two finite hoppings,  $V_{ss\sigma}$  and  $V_{sp\sigma}$ , shown in Fig. 6.1 b). The energy of the in-gap state as a function of both parameters is shown in Fig. 6.1 . Notice the strong dependence with the  $V_{sp\sigma}$  parameter.

It is clear that in order to recover the 1-orbital intuition (in-gap state at  $E = 0$ ) and the experimental observations,<sup>25,113</sup> we require the limit  $V_{sp\sigma} \rightarrow \infty$ . The position of the in-gap state is the most obvious effect, but the composition of its wave-function can change other properties that we discuss in the next sections.

The experimental value for these parameters is difficult to infer, and even *Density Functional Theory* (DFT) calculations depend strongly on the system at hand, so we will consider a wide range of values and explore the resulting physics.

## 6.3 HYPERFINE INTERACTION

Functionalized graphene has many interesting properties.

There is an electronic spin  $S = 1/2$ , and a nuclear spin  $I = 1/2$  very close in space. A natural question is how big is the interaction between them. In particular, if this interaction were *big enough* and *tunable enough*, the system would have all the necessary ingredients to behave as a single qubit. This idea follows very closely the Kane's proposal for a silicon based nuclear spin qubit.<sup>1</sup> In this proposal Kane suggests that it would be possible to use the nuclear spin of Phosphorus dopants ( $^{31}P$ ) embedded in Silicon as qubits. The

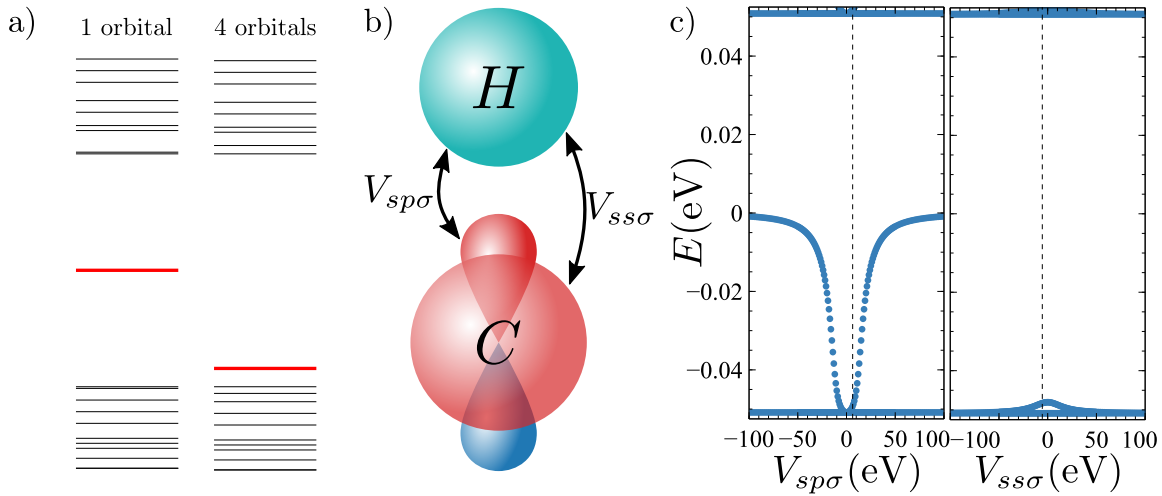


FIGURE 6.1: a) Comparison of the spectrum (sketch) of a graphene island using the vacancy in a one orbital model and an adatom in the SK approximation using the parameters in 2.7. Notice that the in-gap state appears close to the valence band rather than in the middle of the gap. b) Scheme of the hopping processes present in this kind of defects. c) Evolution of the spectrum of an armchair island for different SK parameters for the  $sp^3$  defect. Notice the strong dependence of the in-gap energy with  $V_{sp\sigma}$  especially comparing it with  $V_{ss\sigma}$ . The dashed lines show the value of the “naive” parameters in 2.7

interaction with the qubits would be mediated by the electronic states bounded to the impurity and it could be tuned via an external electric gate which would shift and deform the electronic cloud around the  ${}^{31}P$  to increase/decrease the hyperfine interaction, effectively switching on and off the interaction of the nuclear spin with the rest of the world. Similarly using an electric gate between two dopants it would be possible to tune the inter-qubit interactions. Let us address the “strong enough” requirement in the following section, leaving the tunability question for later chapters.

The hyperfine (HF) interaction arises when we consider the effect of the nuclear spin on the electron.

Apart from the interaction of the electron and the proton with the external magnetic field we have to take into account the interaction between them.

By introducing the potential vector  $\vec{A}_I$  (corresponding to the magnetic field created by the proton,  $\vec{\nabla} \times \vec{A}_I$ ) in the Hamiltonian and expanding to first order in this potential vector, we get the complete hyperfine Hamiltonian:<sup>134</sup>

$$H_{hf} = \frac{-\mu_0}{4\pi} \left[ \frac{q_p}{m_e R^3} \vec{L} \cdot \vec{M}_I + \frac{1}{R^3} (3(\vec{m}_e \cdot \hat{n})(\vec{m}_p \cdot \hat{n}) - \vec{m}_e \cdot \vec{m}_p) + \frac{8\pi}{3} \vec{m}_e \cdot \vec{m}_p \delta(\vec{R}) \right] \quad (6.1)$$

where  $\vec{L}$  is the orbital momentum of the electron,  $\vec{m}_e$  is the magnetic moment of the electron, and  $\hat{n}$  is the unit vector of the straight line joining the proton to the electron.

The first term in equation eq. 6.1 represents the interaction of the nuclear magnetic moment with the magnetic field created at the proton by the rotation of the electronic charge. If we are considering  $s$  orbitals this term will vanish since all the terms would include a factor like  $\langle n, 0, 0 | L | n, 0, 0 \rangle = 0$ , so we will drop this term from the discussion.

The second term represents the dipole-dipole interaction between the nuclear and electronic magnetic moments. Again for a *pure s* orbital this term would vanish as a consequence of the spherical symmetry of the orbital. Nevertheless, because of perturbations (from the crystal or external fields) a contribution from this term may become relevant. **review, and check the possible modification of  $\mathcal{A}$  due to this geometric deformation**

The third term is the so-called “contact term”, and it arises from the singularity at  $\vec{R} = \vec{0}$  of the field created by the magnetic moment of the proton. This contact term describes the interaction of the magnetic moment of the electron spin with the magnetic field inside the proton (considered as punctual). Notice that because of the presence of the delta function in this term, it will be proportional to the overlap of the wave function of the electron and the proton. This term will be the main contribution to the hyperfine interaction.

For the case of a free, isolated Hydrogen atom and for the  $1s$  orbital the calculation of the contact term can be done exactly:

$$H_{hf}^{contact} = \frac{-2\mu_0}{3} \frac{g_p \mu_n}{2} \frac{g_e \mu_e}{2} \langle 1, 0, 0 | \delta(\vec{R}) | 1, 0, 0 \rangle \vec{\sigma}_e \vec{\sigma}_p = \mathcal{A}_0 \vec{\sigma}_e \vec{\sigma}_p \quad (6.2)$$

where the notation for the kets is  $|n, l, m_l\rangle$ , with  $n$  the so-called principal quantum number,  $l$  the orbital angular momentum and  $m_l$  the third component of said angular momentum. The hyperfine coupling,  $\mathcal{A}_0$ , takes the value:

$$\frac{\mathcal{A}_0}{2\pi\hbar} = 1420 \text{ MHz} \quad (6.3)$$

Even when the hyperfine interaction appears with energy units in [eq. 6.2](#), it is commonly expressed in MHz, neglecting the  $2\pi\hbar$  factor. This is technically an abuse of language but widely used, so we will use it carelessly. For the sake of clarity the units have been detailed in [appendix E.3](#).

Notice that the contribution to the hyperfine contact term for  $p$  (or higher  $l$ ) orbitals vanishes since the wave functions of such orbitals vanish at the nucleus position, so the factor  $\langle n, l, m_l | \delta(\vec{R}) | n, l, m_l \rangle$  will always be zero.

In our case of interest,  $H$  adatoms, the hyperfine coupling will be quenched by the occupation of the  $s$  orbital of the  $H$ ,

$$\mathcal{A} = A_0 |\langle \phi_s | \psi \rangle|^2 \quad (6.4)$$

where  $|\psi\rangle$  is any of the eigenstates of the Hamiltonian and  $|\phi_s\rangle$  is the Hydrogen  $s$  orbital.

Of course other orbitals centered at the other atoms would also contribute to the hyperfine interaction (since the wave function does not vanish at the position of the nucleus), nevertheless the *Tight-Binding* (TB) approximation does not offer the tools to deal with the deformation of the orbitals what makes it impossible to estimate the evaluation of the orbitals at the  $H$  nucleus and comparison with DFT calculations show that this effect is not the main one for describing this physics.<sup>135</sup>

For the case of  $Si : {}^{31}P$  the hyperfine coupling in MegaHertz is<sup>14, 136</sup>  $\frac{\mathcal{A}}{2\pi\hbar} = 117 \text{ MHz}$

Since we do not have a reliable estimation of the SK parameters of the adatom, we will consider them as free parameters. In [Fig. 6.1](#) we saw the evolution of the spectrum as a function of the two SK parameters. Here we show both the energy of the in-gap state and the hyperfine coupling as a function of the  $V_{sp\sigma}$ , the main contributor.

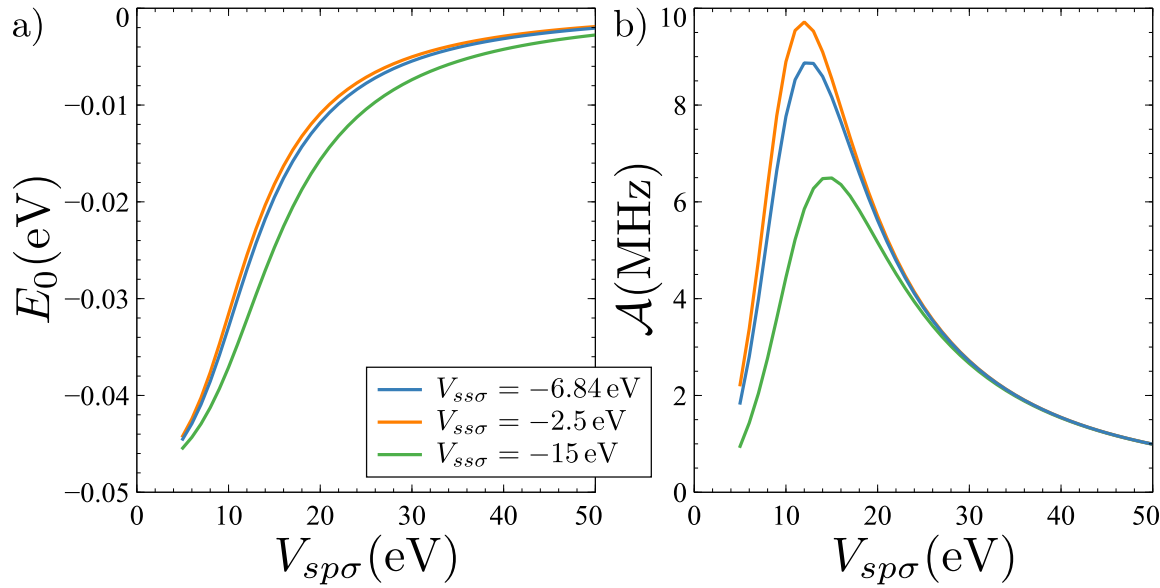


FIGURE 6.2: a) Dependence of the in-gap state arising from a single vacancy in graphene monolayer with the  $V_{sp\sigma}$  coupling for different  $V_{ss\sigma}$ . b) Hyperfine coupling with the  $V_{sp\sigma}$  coupling in a H adatom on top of graphene.

While the position of the in-gap state does not change a lot with the  $V_{ss\sigma}$ , the hyperfine coupling does present a significant variance with this parameter. This behavior is expected since the increasing the  $s - s$  hybridization would reduce the available  $H_s$  weight for the in-gap wave function.

The interesting

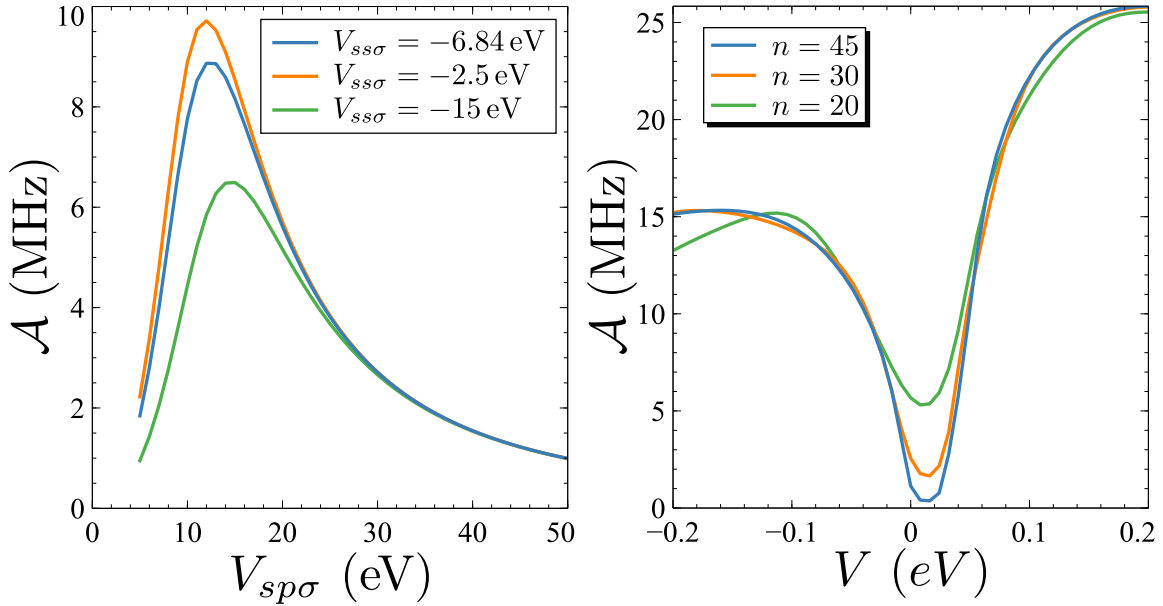


FIGURE 6.3: Hyperfine coupling as a function of SK parameter and electric field

## 6.4 A QUBIT IDEA

In this system we have all the ingredients from the Kane's proposal, so we can write the complete Hamiltonian for our nuclear qubit as a combination of the previous ones:

$$H = -g_e \mu_e \frac{1}{2} \vec{B} \vec{\sigma}^e - g_p \mu_p \frac{1}{2} \vec{B} \vec{\sigma}^p + A \vec{\sigma}^e \cdot \vec{\sigma}^p \quad (6.5)$$

First of all, we can make a quick estimation of the order of magnitude of each of these terms:

- Zeeman for the electron:  $g_e \mu_e \simeq -115.9 \frac{\mu\text{eV}}{\text{T}}$
- Zeeman for the proton:  $g_p \mu_p \simeq 0.176 \frac{\mu\text{eV}}{\text{T}}$
- Hyperfine: Assuming  $\mathcal{A} = 58 \text{ MHz} \Rightarrow \mathcal{A} \simeq 0.003 \mu\text{eV}$

We are stretching a bit the notation in the Hamiltonian eq. 6.5 since each of the terms is expressed in a different basis. Namely, each of the Zeeman terms act only in the electron **or** proton spin subspace but the hyperfine coupling has to be expressed in a 2-particle basis that have not been defined yet. To fix the notation we define the following 2-particle basis:

$$\mathcal{B} = \{|00\rangle, |01\rangle, |10\rangle, |11\rangle\} \quad (6.6)$$

where the first position of the ket corresponds to the electronic state and the second to the nuclear one.

In this basis the Pauli matrices are expressed as follows.

$$\begin{aligned} \sigma_x^e &= \begin{pmatrix} 0 & 0 & 1 & 0 \\ 0 & 0 & 0 & 1 \\ 1 & 0 & 0 & 0 \\ 0 & 1 & 0 & 0 \end{pmatrix} ; \quad \sigma_y^e = \begin{pmatrix} 0 & 0 & -i & 0 \\ 0 & 0 & 0 & -i \\ i & 0 & 0 & 0 \\ 0 & i & 0 & 0 \end{pmatrix} ; \quad \sigma_z^e = \begin{pmatrix} 1 & 0 & 0 & 0 \\ 0 & 1 & 0 & 0 \\ 0 & 0 & -1 & 0 \\ 0 & 0 & 0 & -1 \end{pmatrix} \\ \sigma_x^p &= \begin{pmatrix} 0 & 1 & 0 & 0 \\ 1 & 0 & 0 & 0 \\ 0 & 0 & 0 & 1 \\ 0 & 0 & 1 & 0 \end{pmatrix} ; \quad \sigma_y^p = \begin{pmatrix} 0 & -i & 0 & 0 \\ i & 0 & 0 & 0 \\ 0 & 0 & 0 & -i \\ 0 & 0 & i & 0 \end{pmatrix} ; \quad \sigma_z^p = \begin{pmatrix} 1 & 0 & 0 & 0 \\ 0 & -1 & 0 & 0 \\ 0 & 0 & 1 & 0 \\ 0 & 0 & 0 & -1 \end{pmatrix} \end{aligned} \quad (6.7)$$

Hence, our Hamiltonian for two qubits in the presence of an off-plane magnetic field,  $\vec{B} = (0, 0, B/2)$ , can be expressed as follows:

$$H = \underbrace{-g_e \mu_e \frac{1}{4} B \sigma_z^e}_{E} - \underbrace{g_p \mu_p \frac{1}{4} B \sigma_z^p}_{P} + A \vec{\sigma}^e \cdot \vec{\sigma}^p$$

$$H = \begin{pmatrix} B(E + P) + A & 0 & 0 & 0 \\ 0 & B(E - P) - A & 2A & 0 \\ 0 & 2A & B(-E + P) + A & 0 \\ 0 & 0 & 0 & B(-E - P) - A \end{pmatrix} \quad (6.8)$$

The eigenvalues of this matrix are the following irrelevant?:

$$\begin{aligned} E_0 &= -A - B(P + E) ; \quad v_0 = (0, 0, 0, 1) \\ E_1 &= A + B(P + E) ; \quad v_1 = (1, 0, 0, 0) \\ E_2 &= -\sqrt{A(5A + 2B(P - E)) + B^2(P - E)^2} \\ v_2 &= \left( 0, -\frac{A + B(P - E) + \sqrt{A(5A + 2B(P - E)) + B^2(P - E)^2}}{2A}, 1, 0 \right) \\ E_3 &= \sqrt{A(5A + 2B(P - E)) + B^2(P - E)^2} \\ v_3 &= \left( 0, -\frac{A + B(P - E) - \sqrt{A(5A + 2B(P - E)) + B^2(P - E)^2}}{2A}, 1, 0 \right) \end{aligned} \quad (6.9)$$

For now we will neglect the contribution of the proton and check the behavior of the eigenenergies of the system as a function of both the external magnetic field and the hyperfine coupling.

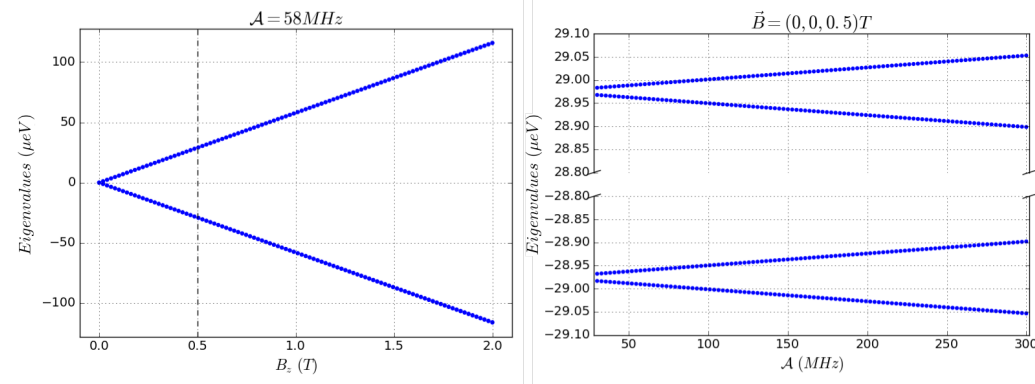


FIGURE 6.4: Evolution of the eigenvalues of the Hamiltonian eq. 6.5 with the magnetic field,  $B$ , and the hyperfine interaction,  $\mathcal{A}$ . The dashed line is used to indicate the magnetic field in the second figure

In figure 6.4 we can see that the energy levels are separated in two sets split by the electronic Zeeman splitting (remember that we are neglecting the proton Zeeman coupling here). The splitting within each of these sets is governed by the hyperfine coupling.

But as we said before, the hyperfine coupling and Zeeman coupling for the proton are in the same order of magnitude. When we include the proton Zeeman interaction the big picture is the same: two sets of levels split by the electronic Zeeman. But within each of these two sets there is a difference, depending on the magnitude of the magnetic field and the hyperfine coupling the ordering of the wave functions may change. *rephrase*

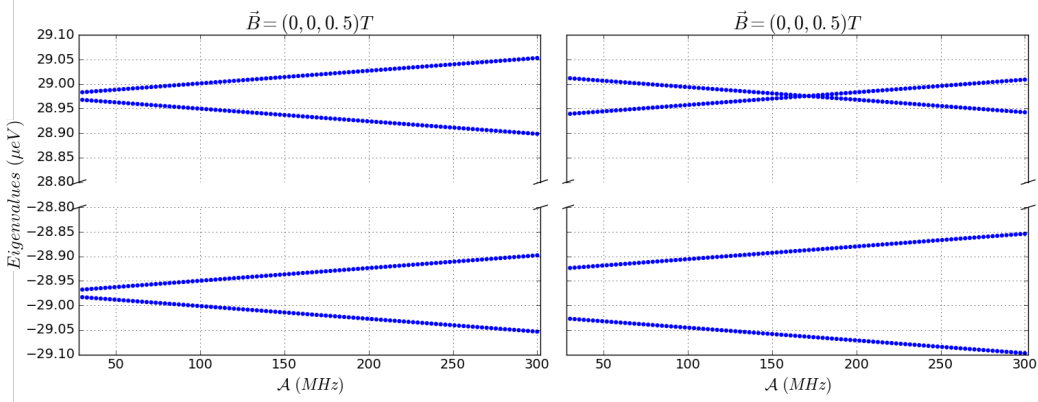


FIGURE 6.5: Comparison of the energy levels as a function of the hyperfine coupling. Panel *a*) neglects the Zeeman term for the proton, in panel *b*) we use the full Hamiltonian. (Both panels share the *Y* axis)

The level crossing that appears in figure 6.5 represents nothing more than the exchange of the wave functions as it can be seen in the analytical expression eq. 6.9 . In fact using these expressions we can get the expression for this level crossing:

$$\mathcal{A}_x = \frac{B}{2} \left( E \pm \sqrt{E^2 + 4EP} \right) \quad (6.10)$$

To clarify the meaning of this spectrum we make a schematic representation of the eigenfunctions, shown in figure 6.6. The left column in the table represents the wave functions neglecting the proton's Zeeman contribution. The two columns in the right do not neglect the proton's coupling, and show the cases of high magnetic field (or low hyperfine coupling) and low magnetic field (or high hyperfine coupling). It is clear that depending on the relative magnitude of the proton's Zeeman effect and the Hyperfine coupling the order of the wave functions may differ.

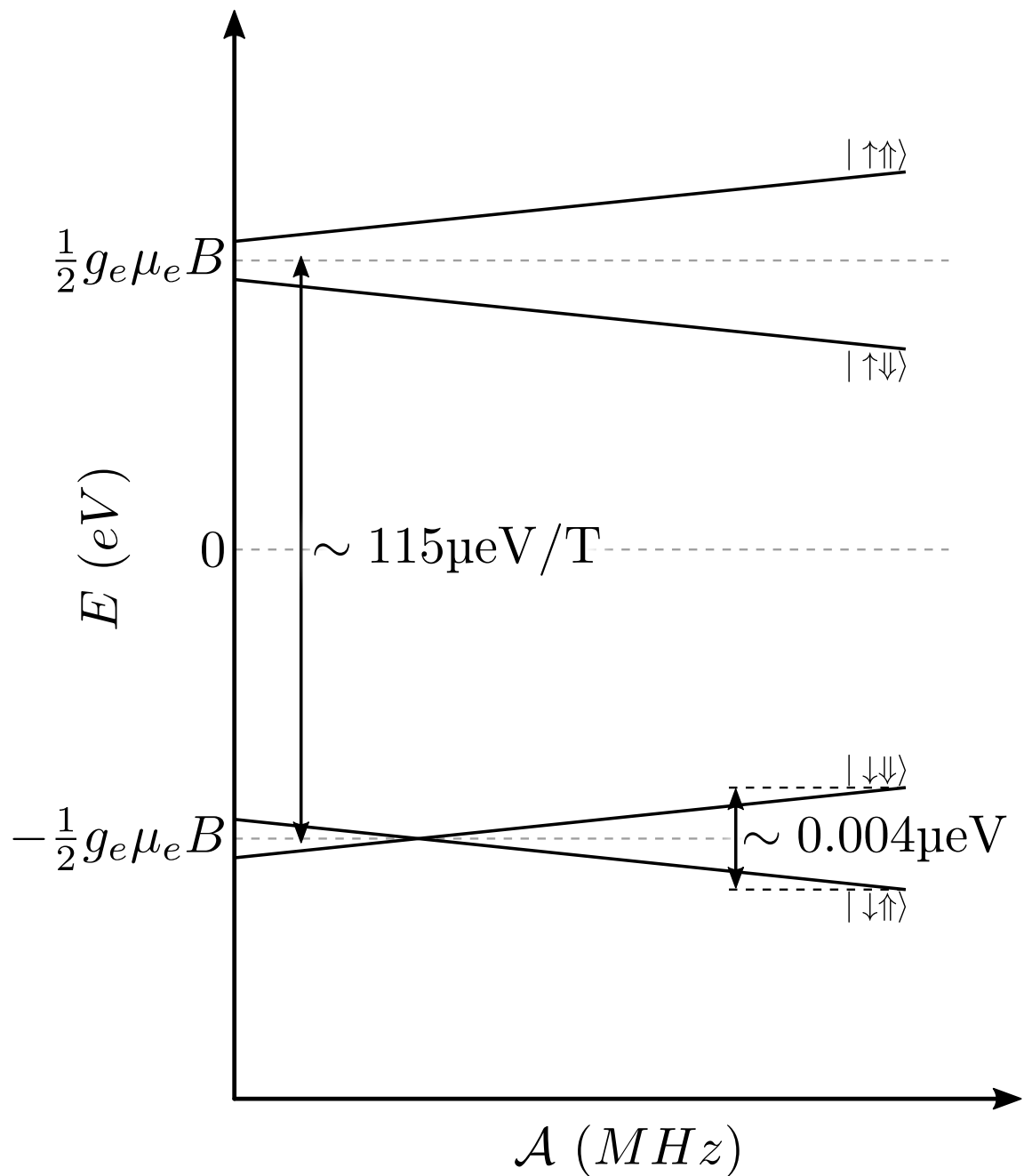


FIGURE 6.6: Sketch of the energy levels for the 1 Qubit Hamiltonian [eq. 6.5](#). The main splitting among the different states is mainly due to the electronic Zeeman terms. The lowest energy state is determined by the competition between the nuclear Zeeman splitting and the hyperfine interaction.

# Designer Fermion Lattices 7

---

The amazingly rich panoply of electronic phases that occur in solid state matter emerges from the interplay of kinetic energy of the electrons and the Coulomb interaction, both electron-electron and electron-ion. These energy scales are defined by the chemical composition and the crystal structure of each material. Physicists have been looking for strategies to create artificial lattices to confine fermions where the geometry and the energy scales can be tuned independently in order to explore emergent electronic phases escaping the dictatorship of chemistry. Examples of artificial lattices include optical traps for cold atoms,<sup>137</sup> arrays of quantum dots,<sup>138,139</sup> and surface adatoms.<sup>140–143</sup>

None of these approaches has reached yet the point where a systematic exploration of large scale lattices with non-trivial phases can be controlled in the quantum regime. Optical traps can create artificial lattices with one fermion per site, but the hopping and Coulomb repulsion energy scales are not much larger than temperature,<sup>137</sup> a requirement to observe non-trivial quantum behaviour. Gate defined quantum dot arrays can definitely avoid that problem,<sup>139</sup> but the largest quantum dot array reported so far has only 9 quantum dots.<sup>138</sup> *Scanning Tunnelling Microscope* (STM) has been used to arrange hundreds of carbon monoxide molecules<sup>140</sup> and thousands of chlorine atoms<sup>144</sup> on a copper surface, defining artificial lattices for electrons in surface states. However, this approach does not allow further electrical control of the carrier density and the electronic states have finite lifetimes on account of their coupling to the substrate.

Here we propose functionalized graphene bilayer with an electrically controlled band gap as a flexible and tunable platform to define both fermion and spin model Hamiltonians with a variety of 1D and 2D lattices with a highly tunable energy scales and filling factors. The building block of the model Hamiltonians are in-gap localized states, produced by  $sp^3$  functionalization of carbon

atoms in hollow sites (see Fig 7.1 a)). This can be achieved by atomic hydrogen chemisorption,<sup>25</sup> but there are many other molecules that produce the same effect.<sup>?</sup> Arrays of these point defects can be created with state of the art STM manipulation,<sup>25</sup> but self-assembly of  $sp^3$  molecular centers could be envisioned. Our calculations show that this platform permits to emulate a number of emblematic lattices (triangular, honeycomb, Kagome, rectangular) with tunable exchange and Coulomb energies, that implement Hubbard and Heisenberg interactions. We show that artificial lattices which realize model Hamiltonians can be created in graphene bilayer which allows the exploration of regimes that lead to the emergence of 2D spin-liquid phases, Mott transitions, quantized anomalous Hall phases, and fractionalized Haldane spin chains and correlated superconductivity.

Different aspects of our proposal have been independently verified experimentally. First, several experiments have demonstrated that an electric field opens up a gap as large as 250 meV in graphene bilayer.<sup>16, 18, 19</sup> Second, the generation of localized zero modes by  $sp^3$  functionalization has been demonstrated by hydrogen chemisorption in graphene,<sup>25</sup> together with the lateral manipulation of the hydrogen atoms, with atomic scale resolution.<sup>25, 145</sup> Last, but not least, the observation of correlated electronic phases in twisted graphene bilayer,<sup>28, 146</sup> that is believed to be associated to the formation of arrays of localized states in a moiré pattern, shows that graphene bilayers can indeed host strongly correlated phases. Here we propose to induce an array of states by chemical functionalization, which would permit to control the location of the bounded states.

## 7.1 METHODS

We consider Bernal stacked graphene bilayers, shown in Fig. 7.1 a). We use the standard single orbital tight binding model<sup>147</sup> and consider first neighbour intralayer hopping  $t = -2.7$  eV and first neighbour interlayer hopping  $\gamma = 0.4$  eV in accordance with the literature.<sup>30</sup>

The effect of  $sp^3$  functionalization is included by removal of a site in the lattice: the  $p_z$  orbital of the carbon atom forms a strong covalent bond with the functional group and is effectively removed from the  $p_z$  lattice. We revisit first the problem of a single  $sp^3$  defect in graphene bilayer,<sup>129</sup> focusing on the influence of an off-plane electric potential difference, denoted  $\mathcal{E}$ , which has been considered already in the literature.<sup>148</sup> In the upper layer of Bernal stacked bilayer graphene one of the sublattices is connected to the lower layer while the

other sublattice lay on *hollow* positions. We will consider only functionalization of atoms in hollow sites (see Fig 7.1 a)).

At zero electric field,  $\mathcal{E} = 0$ , pristine graphene bilayer is a zero gap semiconductor, with a degenerate conduction and valence band at the  $K$  and  $K'$  points of the Brillouin zone.<sup>147</sup> The  $sp^3$  functionalization creates a zero mode resonance,<sup>129,148</sup> as expected in any bipartite lattice with a gapless spectrum and with a missing site.<sup>133</sup> The application of an electric field opens up a gap in the pristine bilayer spectrum and, as we show below, the zero energy resonance becomes a bound state.

In order to study the single particle spectra of graphene bilayer with  $sp^3$  functionalizations we resort to Lanczos diagonalization<sup>130,132</sup> of the single-particle tight-binding model, due to the very large number of carbon sites. For instance, the island used in the calculations of Fig. 7.1 has  $N = 131772$  sites and a corresponding quantum confinement gap of  $\sim 7$  meV which becomes irrelevant when the gap induced by the electric field is much larger. The results of Fig. 7.1 c) show the evolution of the in-gap state as well as a few conduction and valence states as a function of the off-plane electric field. It is apparent that as the field is increased, a gap opens and the zero mode resonance stays inside the gap, becoming a bound state with a normalized wave function.

Importantly, the extension of the in-gap bound state induced by the  $sp^3$  functionalization can be electrically tuned. In Fig. 7.1 d) we show the confinement length of the in-gap state as a function of the electric field calculated as the minimal radius which contains  $> 98\%$  of the in-gap wave function. The extension of the in-gap state is controlled by the size of the energy gap, as shown in the inset of Fig. 7.1 d). This result that can be obtained analytically as well.<sup>148</sup> This is an important resource in order to control the extension of the in-gap states, and hence the overlap among defects. This will be one of the key ingredients to control the energy bandwidth in artificial lattices and the effective Hubbard repulsion.

## 7.2 ONE-BODY RESULTS

We now study the single particle states of artificial arrays of  $sp^3$  functionalization. We have considered two geometries: triangular and honeycomb, although many other structures, such as Kagome and rectangular, are possible by functionalization of the hollow sublattice of the top layer. The calculation is carried out using a supercell with one (triangular) or two (honeycomb)  $sp^3$  defects. As expected, we obtain as many in-gap bands as  $sp^3$  defects in the unit cell. The corresponding in-gap energy bands for triangular and honeycomb artificial lat-

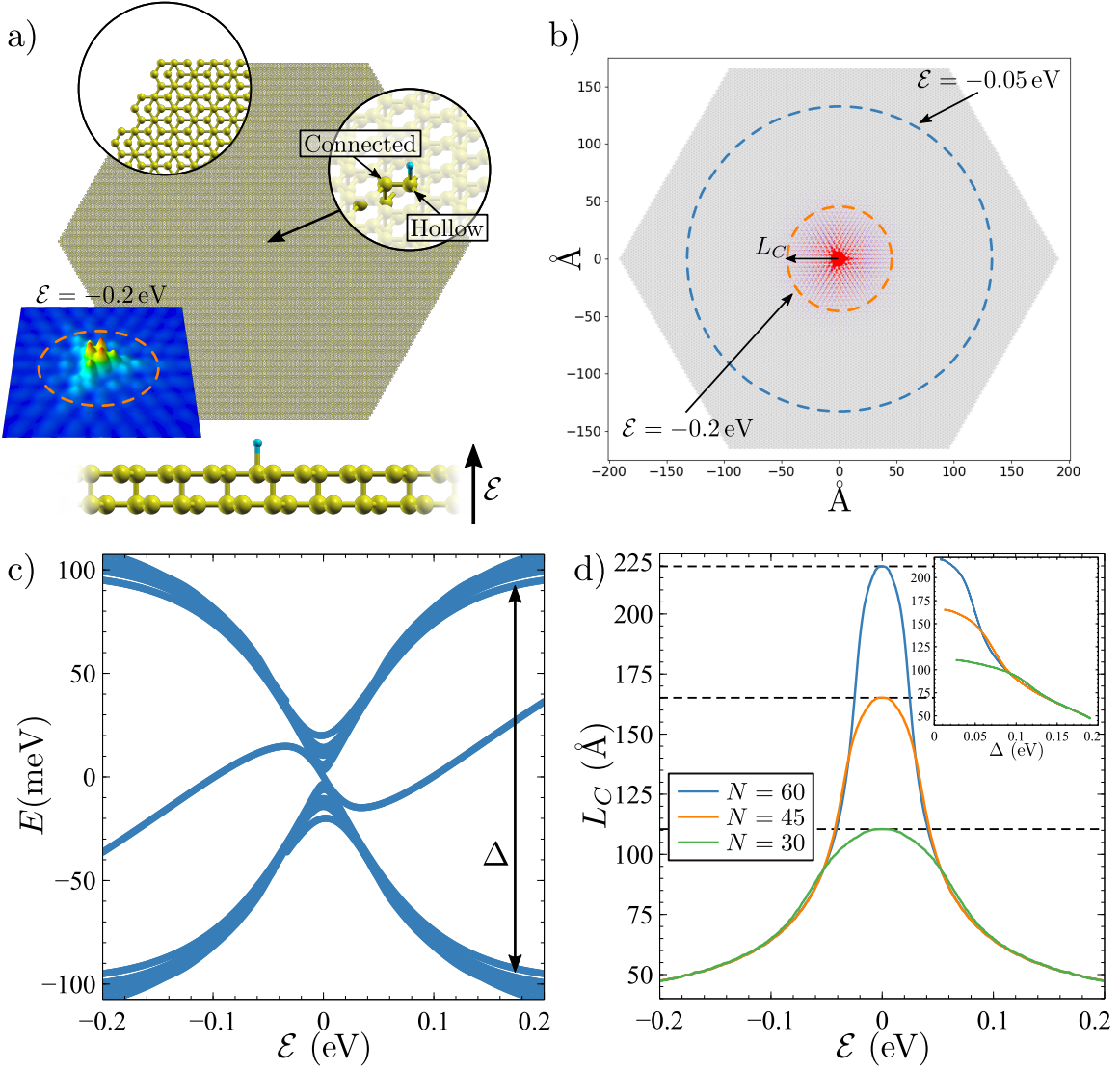


FIGURE 7.1: a) A bilayer graphene flake with armchair edges and a chemisorbed H adatom in the presence of an electric field is suggested as a platform to realize a number of fermionic models. The building blocks of these models are the electronic states localized around the  $sp^3$  as shown in the 3-D simulation of the local density of states. b) Spatial distribution of the in-gap state created by a  $sp^3$  defect in bilayer graphene in the presence of an electric field  $\mathcal{E} = -0.2 \text{ eV}$ . The two dashed lines show the confinement length for two values of the electric potential difference. c) Evolution of the 12 eigenenergies closest to  $E = 0$  with the electric field. d) Confinement length  $L_C$  as a function of the electric field for different size islands. The dashed horizontal lines mark the maximal  $L_C$  as given by the island size.

tices with different electric fields are shown in Fig. 7.2, for two different values of the off-plane electric field.

The in-gap bands can be perfectly fitted to tight-binding models for the triangular and honeycomb lattice with hopping up to third neighbours. These energy bands arise because, in the presence of an electric field, the  $sp^3$  in-gap states are no longer sublattice polarized. Therefore, adjacent in-gap states can hybridize, leading to the formation of in-gap bands. The size of the unit cell determines the distance between the point defects and the electric field determines the extension of the bound states. Thus, both the density of defects and the electric field determine the bandwidth which is in the range of 10 meV for the cases shown in Fig. 7.2.

The results of Figs. 7.1 and 7.2 show that functionalization of gapped graphene bilayer with ordered arrays of  $sp^3$  defects lead to the formation of in-gap energy bands that can be understood in terms of a tight-binding lattice model, where every functionalization corresponds to a site and a relatively short ranged hopping matrix. Importantly, the density of carriers can be tuned independently of the size of the graphene bilayer, using dual gating.<sup>18,19</sup> Therefore, the Fermi energy could be moved along the bandwidth, controlling the filling factor, very much like in the case of the flat bands in the magic angle twisted bilayer.<sup>28,146</sup>

### 7.3 MANY-BODY RESULTS

We now consider the effect of electron-electron interactions. For that matter, we model the Coulomb interaction for the functionalized graphene bilayer in the Hubbard approximation. Our main goal is to provide a fair estimate of the magnitude of the effective Coulomb repulsion for the electrons occupying the in-gap bands of the artificial lattices. We consider the exact solution for the minimal system where hybridization and Coulomb repulsion compete with each other, namely, a dimer at half filling. The energy scales of this problem are controlled by both the distance between the two  $sp^3$  defects and the gap induced by the electric field.

We first solve the single particle problem for two impurities, using again a bilayer island (with up to  $N=131772$  sites) and two  $sp^3$  centers. The diagonalization yields two in-gap states, with energy  $\epsilon \pm \frac{\delta}{2}$ , where  $\delta$  is the hybridization splitting of the states. Two states  $\phi_{1/2}$ , localized states around the defects, can be built out of the two in-gap eigenstates,  $\psi_{\pm}$ :

$$|\phi_{1/2}\rangle = \frac{1}{\sqrt{2}} (|\psi_+\rangle \pm |\psi_-\rangle) \quad (7.1)$$

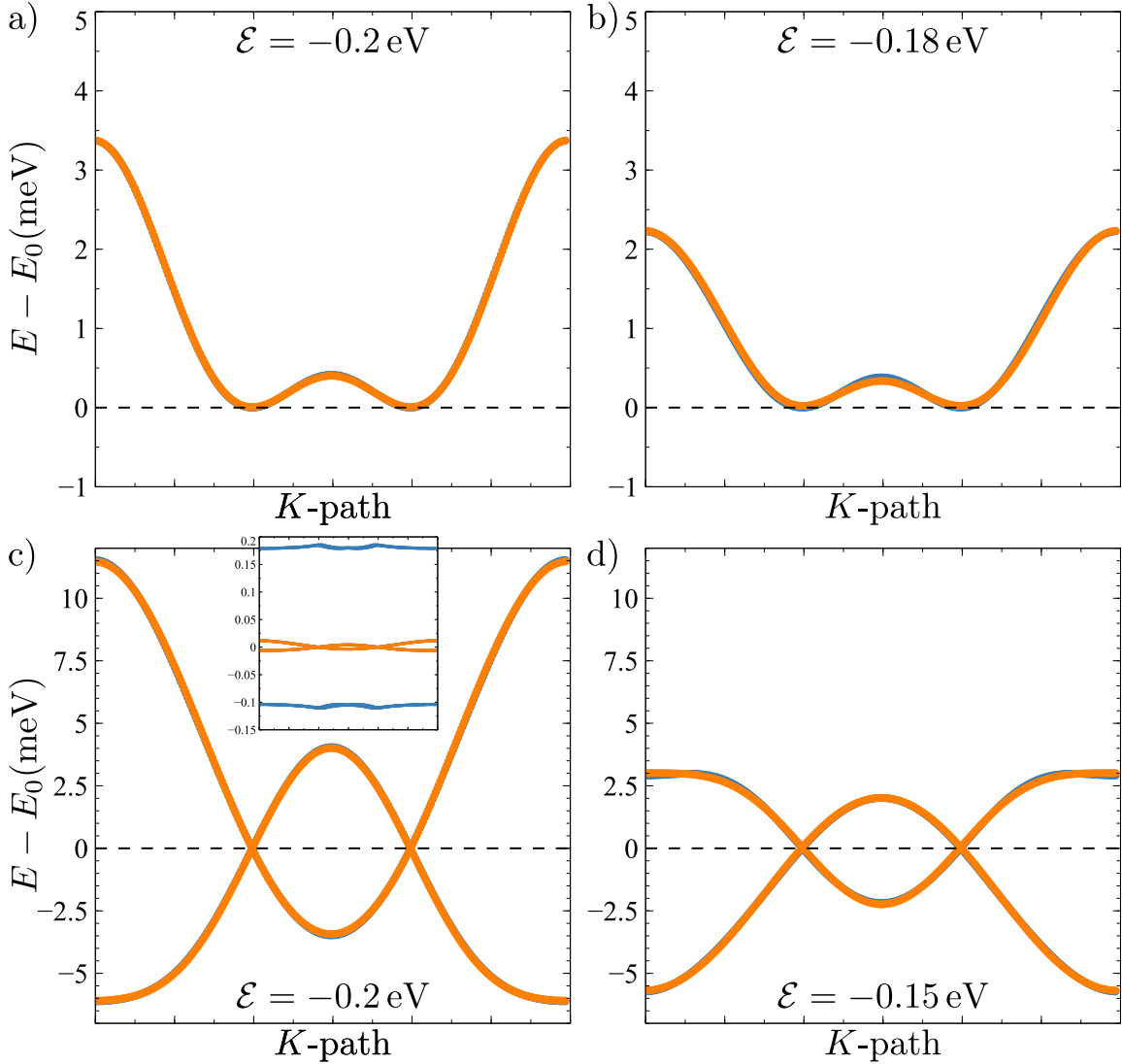


FIGURE 7.2: In-gap energy bands for a triangular (a,b) and a honeycomb lattice (c,d) of  $sp^3$  defects on a graphene bilayer for two different values of the electric field. The inset of panel c) also shows the conduction and valence bands. The bands obtained by fitting to tight-binding models for triangular and honeycomb lattices with one orbital per site and up to third neighbour hopping are also plotted in blue, but barely visible due to the perfect fitting.

In the following we refer to  $\phi_1$  and  $\phi_2$  as site states, but it has to be kept in mind that they are extended states living in hundreds of carbon atoms.

We now build the many body Hamiltonian for two electrons in two states,  $\phi_{1,2}$ . The Hamiltonian can be written as the sum of the singe particle part  $\mathcal{H}_0$  and the Coulomb interaction part  $\mathcal{H}_U$ . The first term reads:

$$\mathcal{H}_0 = \tilde{t} \sum_{\sigma} \left( c_{1\sigma}^{\dagger} c_{2\sigma} + c_{2\sigma}^{\dagger} c_{1\sigma} \right) \quad (7.2)$$

where  $c_{\eta\sigma}^{\dagger}$ , with  $\eta = \{1, 2\}$  creates an electron with spin  $\sigma$  in the site state  $\phi_{\eta}$  and  $\tilde{t} = \frac{\delta}{2}$

A minimal model for the Coulomb contribution is obtained using the Hubbard approximation and truncating the Hilbert space to just the two in-gap states. When represented in the basis of the two site-orbitals, the Hubbard term can be expressed as the sum of four types of contributions.<sup>149</sup>

$$\begin{aligned} \mathcal{H}_U = & \left( \tilde{U}_1 - \frac{J}{4} \right) n_{1\uparrow} n_{1\downarrow} + \left( \tilde{U}_2 - \frac{J}{4} \right) n_{2\uparrow} n_{2\downarrow} - \\ & - J \vec{S}_1 \cdot \vec{S}_2 + \mathcal{V}_{\text{pair}} + \mathcal{V}_{12} + \mathcal{V}_{21} \end{aligned} \quad (7.3)$$

where  $n_{\eta\sigma} = c_{\eta\sigma}^{\dagger} c_{\eta\sigma}$  is the occupation operator in the basis of  $\phi_{1,2}$ ,  $\vec{S}_{\eta} = \frac{1}{2} \sum_{\sigma, \sigma'} c_{\eta\sigma}^{\dagger} \vec{\tau}_{\sigma, \sigma'} c_{\eta\sigma'}$  are the spin operators associated to these quantum states.

Hubbard-like terms, with energy  $\tilde{U}_{\eta} - \frac{J}{4}$  describe the Coulomb energy penalty of double occupation of states  $\phi_1$  and  $\phi_2$ . The energy scales  $\tilde{U}_{\eta}$  are given by  $\tilde{U}_{\eta} = U \sum_i |\phi_{\eta}(i)|^4$  where  $\sum_i |\phi_{\eta}(i)|^4$  is the so-called inverse participation ratio (IPR) and it is a metric of the extension of the state<sup>149</sup> and  $U$  is the atomic carbon on-site repulsion. Because of the symmetry of site states, we have  $\mathcal{U}_1 \simeq \mathcal{U}_2$ . Here we take  $U = |t| = 2.7 \text{ eV}$ . The second type of term is a ferromagnetic exchange with  $J = 2U \sum_i |\phi_1(i)|^2 |\phi_2(i)|^2$  which is a metric of the *overlap* of the two site states. The last two terms are *density assisted* hopping terms,

$$\mathcal{V}_{21} = \sum_{\sigma} n_{1\sigma} \left( t_{12} c_{1\bar{\sigma}}^{\dagger} c_{2\bar{\sigma}} + t_{12}^* c_{2\bar{\sigma}}^{\dagger} c_{1\bar{\sigma}} \right) \quad (7.4)$$

and the pairing hopping term:

$$\mathcal{V}_{\text{pair}} = \Delta c_{1\uparrow}^{\dagger} c_{1\downarrow}^{\dagger} c_{2\uparrow} c_{2\downarrow} + \Delta^* c_{2\uparrow}^{\dagger} c_{2\downarrow}^{\dagger} c_{1\uparrow} c_{1\downarrow} \quad (7.5)$$

The Hubbard matrix elements that control these Coulomb energies assisted with hopping processes are:  $t_{12} = U \sum_i |\phi_1(i)|^2 \phi_1(i)^* \phi_2(i)$  and  $\Delta = U \sum_i (\phi_1(i)^*)^2 \phi_2(i)^2$ . Both  $t_{12}$  and  $\Delta$  could be complex numbers.

The evolution of each of these energy scales as we vary both the applied electric field and the dimer separation is shown in Fig. 7.3 a-c). At zero field, the site states are sublattice polarized and the only finite energy scale is the ferromagnetic exchange  $J$  and the pair hopping  $\Delta$ . As the field is ramped up,

for both polarities, the site states acquire weight on both sublattices, which permits to have finite  $\tilde{t}$ ,  $\Delta$ , and  $t_{1,2}$ . At the same time, their extension starts to shrink. The competition between these two effects leads both to the non monotonic behaviour of  $\delta$ , as well as to the decay of  $J$  and  $\Delta$ . Importantly, for a sufficiently large electric field and defect separation, the dominant energy scales are  $\tilde{t}$  and  $\mathcal{U}$ , showing that the artificial lattice defines an effective Hubbard model with narrow energy bands.

We now discuss the properties of the multi-electronic eigenstates of  $\mathcal{H} = \mathcal{H}_0 + \mathcal{H}_U$ . We can expand these states in the basis of configurations with a well defined occupation of the single particle states  $|\phi_{1,2}\rangle$ . There are 6 such configurations for 2 electrons in 2 single particle states: four open-shell many-body states, where there is one electron per site-state and two closed shell states, where one of the site states is doubly occupied and the other is empty. The eigenstates of  $\mathcal{H}$  have a well defined total spin  $S$  that can take two values,  $S = 0$  and  $S = 1$ . The triplet is formed with open shell configurations. In contrast, the  $S = 0$  states combine both open and closed shell configurations.

For the dimer at half-filling, tuning the electric field can lead to three limiting cases with different types of ground state. For zero electric field, the only non-vanishing energy scales are  $J$  and  $\Delta$ . Since the site state wave functions are real, we have  $J = 2\Delta$ , leading to a  $S = 1$  ground state, complying with Lieb's theorem for a bipartite lattice.<sup>133</sup> At finite electric field both  $\mathcal{U}$  and  $\tilde{t}$  rapidly overcome the other energy scales, so that the system effectively becomes a Hubbard dimer. This leads to  $S = 0$  ground states. Here, we can have two different limiting situations.<sup>150</sup> In the strong coupling limit,  $\mathcal{U} \gg \tilde{t} \gg J$ , the ground state is an open shell singlet with an entangled spin state. In the limit of weak coupling,  $\tilde{t} \gg \mathcal{U} \gg J$ , the system behaves like a Hydrogen molecule, with two electrons occupying a bonding molecular orbital. The corresponding many-body energy spectra for the weak and strong coupling cases at finite field are shown in Fig. 7.3 d).

We now discuss qualitatively on the different electronic phases that could emerge in the limit of large lattices, on the basis of the predictions for a Hubbard model with first neighbour hoppings, although, other terms, such as beyond-first neighbour hopping, direct exchange and other many-body terms are also present. At half filling, the honeycomb and triangular lattices are expected to undergo a transition from a paramagnetic conducting phase to a Mott insulator that can either have magnetic order<sup>151</sup> or be spin liquids,<sup>152</sup> as the ratio  $\tilde{U}/\tilde{t}$  goes above a critical threshold.

Away from half filling many other non-trivial phases have been predicted. For the triangular lattice at 3/4 filling, a non-coplanar spin canted phase with a Chern number  $\mathcal{C} = 2$  has been predicted<sup>153</sup> giving rise to a quantized anomalous

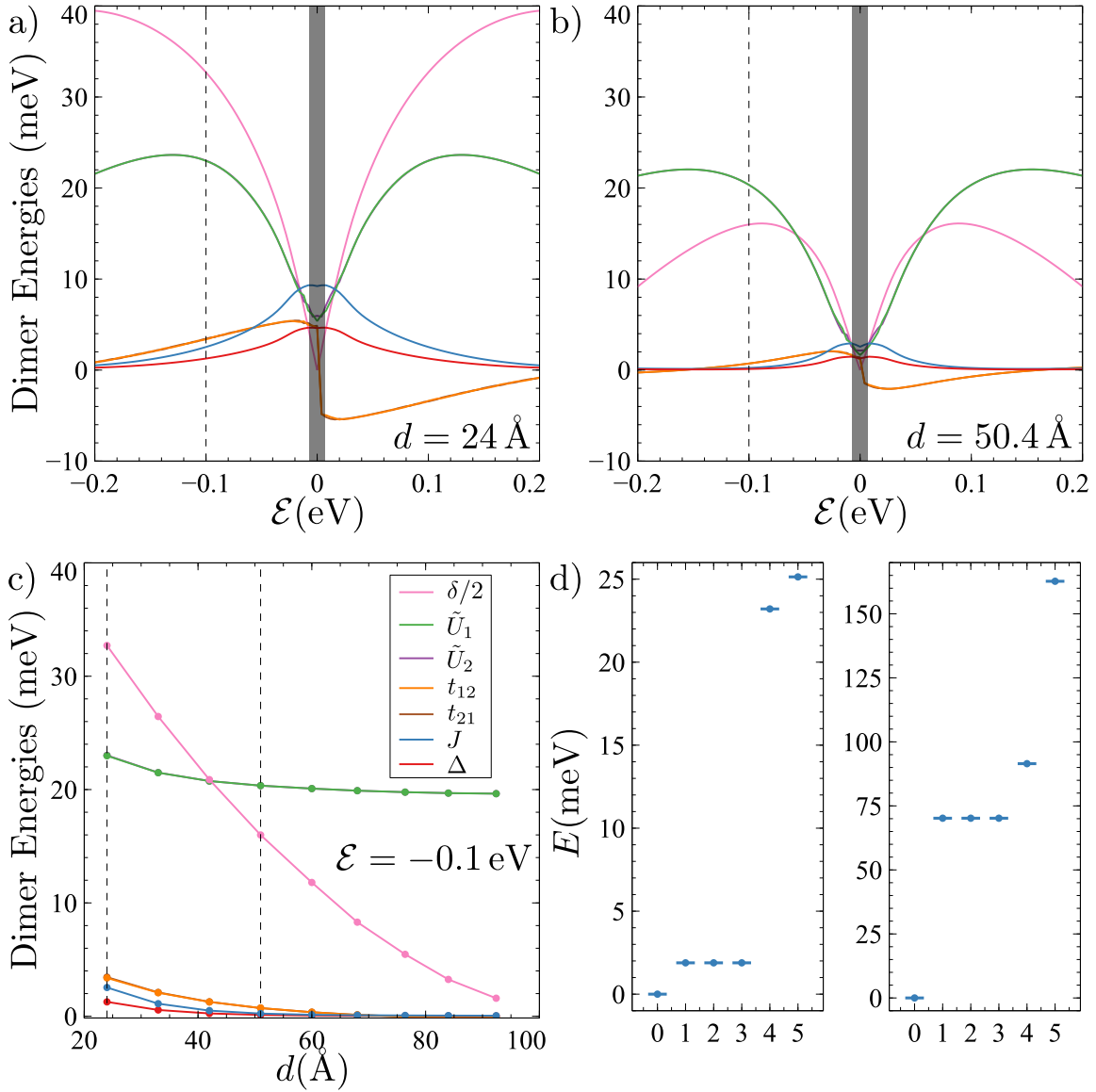


FIGURE 7.3: a,b) Dependence of  $J$ ,  $U_{1/2}$ ,  $t_{12/21}$  and  $\Delta$  on electric field for two  $\text{sp}^3$  defects separated by  $d = 24 \text{ \AA}$  and  $50.4 \text{ \AA}$  respectively. The dark stripes around  $\mathcal{E} = 0$  show the regime in which the confinement gap is comparable to the electric field induced gap. c) Dependence of the Hubbard parameters with the distance between  $\text{sp}^3$  defects at  $\mathcal{E} = -0.1 \text{ eV}$ . d) Many body spectra at the strong ( $d = 92.4 \text{ \AA}$ ,  $\mathcal{E} = -0.2 \text{ eV}$ ) and weak coupling limit ( $d = 25.2 \text{ \AA}$ ,  $\mathcal{E} = -0.2 \text{ eV}$ ). The weak to strong coupling transition can be achieved changing either  $d$  or  $\mathcal{E}$ .

Hall effect. In the case of the honeycomb, chiral superconductivity has been predicted when the Fermi energy is tuned at the Van Hove singularities.<sup>154</sup> The application of perpendicular magnetic field would lead to the quantized regime

at much smaller magnetic fields, on account of the larger unit cell. Finally, superconducting proximity effect, induced by lateral superconducting contacts, might bring an additional knob to induce novel electronic phases, including topological superconductivity.<sup>155</sup> Of course, the sp<sup>3</sup> functionalization approach could be used to create zero and one dimensional structures as well.

The experimental realization of this type of artificial lattices will face several technical challenges. So far, the manipulation of hydrogen atoms on graphene has been demonstrated with up to 14 atoms.<sup>25</sup> In principle, there is no limit on the number of adatoms that can be manipulated.<sup>143</sup> For instance, up to 80000 chlorine atoms on a Cu(111) surface were manipulated, making use of automatic protocols.<sup>144</sup> Importantly, the number of localized states needed for emergent phases to occur is definitely smaller than that: the correlated phases observed in magic angle twisted bilayer graphene occur in samples with 10<sup>4</sup> Moiré unit cells. A second important challenge will be the combination of STM manipulation and dual gating. A possible implementation would be to carry out the atomic manipulation on a graphene bilayer placed on a gated substrate and use the STM as a top gate. This would require to have electrodes on the sample to carry out in-plane transport to probe the electronic phases.

#### 7.4 CONCLUSIONS

In summary, we have analysed the potential of functionalized graphene bilayer to produce artificial fermion lattices where the band and Coulomb energies can be tuned by means of gate voltages and geometrical control of the defects. The system proposed here combines the advantage of electric control afforded by quantum dots arrays, and the advantage of reversible structural control given by STM atomic manipulation. The proposed platform could be used to explore a very large variety of electronic phases, including Mott-Hubbard transition, magnetically ordered phases, quantized anomalous insulators, spin liquids and superconducting phases.

# Conclusions and Outlook 8

---

Bye bye

## My publications

A

My publications are

This<sup>85</sup>

This<sup>156</sup>

This<sup>150</sup>



This<sup>29</sup>

This<sup>86</sup>

This<sup>87</sup>

This<sup>157</sup>

This<sup>158</sup>

This<sup>159</sup>

This<sup>149</sup>

# Slater-Koster hoppings

**B**

---

In this chapter we just summarize the *Slater-Koster* (SK) hoppings. In every case it is assumed that the orbitals are separated by a vector  $\vec{r}$  and

$$\vec{r} \longrightarrow \hat{r} = \frac{\vec{r}}{|\vec{r}|} = (l, m, n)$$

The formulas for the  $s - p$  hoppings are:

$$\begin{aligned} t_{ss} &= V_{ss\sigma} \\ t_{sp_x} &= lV_{ss\sigma} \end{aligned} \tag{B.1}$$

by symmetry it follows that:

$$t_{sp_y}(l, m, n) = t_{sp_x}(m, -l, n) \quad \text{and} \quad t_{sp_z}(l, m, n) = t_{sp_x}(n, m, -l) \tag{B.2}$$

The formulas for hoppings among the  $p$  orbitals are:

$$\begin{aligned} t_{p_x-p_x} &= l^2 V_{pp\sigma} + (1 - l^2) V_{pp\pi} \\ t_{p_x-p_y} &= lm V_{pp\sigma} - lm V_{pp\pi} \\ t_{p_x-p_z} &= ln V_{pp\sigma} - ln V_{pp\pi} \end{aligned} \tag{B.3}$$

which imply that:

$$\begin{aligned} t_{p_y-p_y}(l, m, n) &= t_{p_x-p_x}(m, -l, n) \\ t_{p_y-p_z}(l, m, n) &= t_{p_x-p_y}(m, n, l) \\ t_{p_z-p_z}(l, m, n) &= t_{p_z-p_z}(n, m, -l) \end{aligned} \tag{B.4}$$

the formulas for the  $s - d$  hoppings are:

$$\begin{aligned} t_{s-d_{xy}} &= \sqrt{3}lm V_{sd\sigma} \\ t_{s-d_{x^2-y^2}} &= \frac{\sqrt{3}}{2}(l^2 - m^2) V_{sd\sigma} \\ t_{s-d_{3x^2-r^2}} &= \left[ n^2 - \frac{1}{2}(l^2 + m^2) \right] V_{sd\sigma} \end{aligned}$$

for the  $p-d$  hoppings:

$$\begin{aligned}
 t_{p_x-d_{xy}} &= \sqrt{3}l^2mV_{pd\sigma} + m(1-2l^2)V_{pd\pi} \\
 t_{p_x-d_{yz}} &= \sqrt{3}lmnV_{pd\sigma} - 2lmnV_{pd\pi} \\
 t_{p_x-d_{zx}} &= \sqrt{3}l^2nV_{pd\sigma} + n(1-2l^2)V_{pd\pi} \\
 t_{p_x-d_{x^2-y^2}} &= \frac{\sqrt{3}}{2}l(l^2-m^2)V_{pd\sigma} + l(1-l^2+m^2)V_{pd\pi} \\
 t_{p_y-d_{x^2-y^2}} &= \frac{\sqrt{3}}{2}m(l^2-m^2)V_{pd\sigma} - m(1+l^2-m^2)V_{pd\pi} \\
 t_{p_z-d_{x^2-y^2}} &= \frac{\sqrt{3}}{2}n(l^2-m^2)V_{pd\sigma} - n(l^2-m^2)V_{pd\pi} \\
 t_{p_x-d_{3z^2-r^2}} &= l\left[n^2 - \frac{1}{2}(l^2+m^2)\right]V_{pd\sigma} - \sqrt{3}ln^2V_{pd\pi} \\
 t_{p_y-d_{3z^2-r^2}} &= m\left[n^2 - \frac{1}{2}(l^2+m^2)\right]V_{pd\sigma} - \sqrt{3}mn^2V_{pd\pi} \\
 t_{p_z-d_{3z^2-r^2}} &= n\left[n^2 - \frac{1}{2}(l^2+m^2)\right]V_{pd\sigma} + \sqrt{3}n(l^2+m^2)V_{pd\pi}
 \end{aligned}$$

and inter- $d$  hoppings:

$$\begin{aligned}
 t_{d_{xy}-d_{xy}} &= 3l^2m^2V_{dd\sigma} + (l^2+m^2-4l^2m^2)V_{dd\pi} + (n^2+l^2m^2)V_{dd\delta} \\
 t_{d_{xy}-d_{yz}} &= 3lm^2nV_{dd\sigma} + ln(1-4m^2)V_{dd\pi} + ln(m^2-1)V_{dd\delta} \\
 t_{d_{xy}-d_{zx}} &= 3l^2mnV_{dd\sigma} + mn(1-4l^2)V_{dd\pi} + mn(l^2-1)V_{dd\delta} \\
 t_{d_{xy}-d_{x^2-y^2}} &= \frac{3}{2}lm(l^2-m^2)V_{dd\sigma} + 2lm(m^2-l^2)V_{dd\pi} + \frac{1}{2}lm(l^2-m^2)V_{dd\delta} \\
 t_{d_{yz}-d_{x^2-y^2}} &= \frac{3}{2}mn(l^2-m^2)V_{dd\sigma} - mn[1+2(l^2-m^2)]V_{dd\pi} + mn[1+\frac{1}{2}(l^2-m^2)]V_{dd\delta}
 \end{aligned}$$

Hopping	Slater-Koster formula
$s - s =$	$V_{ss\sigma}$
$s - p_x =$	$lV_{ss\sigma}$
$s - p_y =$	$t_{sp_x}(m, -l, n)$
$s - p_z =$	$t_{sp_x}(n, m, -l)$
$p_x - p_x =$	$l^2 V_{pp\sigma} + (1 - l^2) V_{pp\pi}$
$p_x - p_y =$	$lm V_{pp\sigma} - lm V_{pp\pi}$
$p_x - p_z =$	$ln V_{pp\sigma} - ln V_{pp\pi}$
$p_y - p_y =$	$t_{p_x p_x}(m, -l, n)$
$p_y - p_z =$	$t_{p_x p_y}(m, n, l)$
$p_z - p_z =$	$t_{p_z p_z}(n, m, -l)$
$s - d_{xy} =$	$\sqrt{3}lm V_{sd\sigma}$
$s - d_{yz} =$	$t_{sd_{xy}}(n, m, -l)$
$s - d_{zx} =$	$t_{sd_{xy}}(l, n, -m)$
$s - d_{x^2-y^2} =$	$\frac{\sqrt{3}}{2}(l^2 - m^2) V_{sd\sigma}$
$s - d_{3x^2-r^2} =$	$[n^2 - \frac{1}{2}(l^2 + m^2)] V_{sd\sigma}$
$p_x - d_{xy} =$	$\sqrt{3}l^2 m V_{pd\sigma} + m(1 - 2l^2) V_{pd\pi}$
$p_x - d_{yz} =$	$\sqrt{3}lm n V_{pd\sigma} - 2lm n V_{pd\pi}$
$p_x - d_{zx} =$	$\sqrt{3}l^2 n V_{pd\sigma} + n(1 - 2l^2) V_{pd\pi}$
$p_x - d_{x^2-y^2} =$	$\frac{\sqrt{3}}{2}l(l^2 - m^2) V_{pd\sigma} + l(1 - l^2 + m^2) V_{pd\pi}$
$p_y - d_{x^2-y^2} =$	$\frac{\sqrt{3}}{2}m(l^2 - m^2) V_{pd\sigma} - m(1 + l^2 - m^2) V_{pd\pi}$
$p_z - d_{x^2-y^2} =$	$\frac{\sqrt{3}}{2}n(l^2 - m^2) V_{pd\sigma} - n(l^2 - m^2) V_{pd\pi}$
$p_x - d_{3z^2-r^2} =$	$l[n^2 - \frac{1}{2}(l^2 + m^2)] V_{pd\sigma} - \sqrt{3}ln^2 V_{pd\pi}$
$p_y - d_{3z^2-r^2} =$	$m[n^2 - \frac{1}{2}(l^2 + m^2)] V_{pd\sigma} - \sqrt{3}mn^2 V_{pd\pi}$
$p_z - d_{3z^2-r^2} =$	$n[n^2 - \frac{1}{2}(l^2 + m^2)] V_{pd\sigma} + \sqrt{3}n(l^2 + m^2) V_{pd\pi}$
$d_{xy} - d_{xy} =$	$3l^2 m^2 V_{dd\sigma} + (l^2 + m^2 - 4l^2 m^2) V_{dd\pi} + (n^2 + l^2 m^2) V_{dd\delta}$
$d_{xy} - d_{yz} =$	$3lm^2 n V_{dd\sigma} + ln(1 - 4m^2) V_{dd\pi} + ln(m^2 - 1) V_{dd\delta}$
$d_{xy} - d_{zx} =$	$3l^2 m n V_{dd\sigma} + mn(1 - 4l^2) V_{dd\pi} + mn(l^2 - 1) V_{dd\delta}$
$d_{xy} - d_{x^2-y^2} =$	$\frac{3}{2}lm(l^2 - m^2) V_{dd\sigma} + 2lm(m^2 - l^2) V_{dd\pi} + \frac{1}{2}lm(l^2 - m^2) V_{dd\delta}$
$d_{yz} - d_{x^2-y^2} =$	$\frac{3}{2}mn(l^2 - m^2) V_{dd\sigma} - mn[1 + 2(l^2 - m^2)] V_{dd\pi} + mn[1 + \frac{1}{2}(l^2 - m^2)] V_{dd\delta}$

# Quantum Spin Hall C

---

## C.1 HOMOGENEOUS MULTILAYERS

Monolayer graphene consists of a triangular lattice with two atoms per unit cell that leads, in the reciprocal space, to a hexagonal Brillouin zone that hosts Dirac cones in its corners. When  $N$  layers are considered the crystalline structure remains the same, only there will be  $2N$  atoms per unit cell. We shall only use the so called Bernal stacking, shown in Fig. C.1, which is the ground state configuration, according to both *Density Functional Theory* (DFT) calculations and experimental evidence.<sup>71–73</sup> In Bernal stacked materials an atom from the sublattice  $B(A)$  sits on top of an atom belonging to the other sublattice  $A(B)$ . For  $N = 2$  there is only one way to achieve this, but for  $N > 2$  there are different possible stacking orders. In figure C.1 we show the different possibilities for  $N \leq 4$ , with a self-evident notation.

### *The Model*

We describe the multilayers with the following tight-binding Hamiltonian:

$$H = H_{ML} + \eta H_{inter} + \lambda \vec{L} \cdot \vec{S} \quad (\text{C.1})$$

where  $H_{ML}$  and  $H_{inter}$  account for the intralayer and interlayer hoppings, respectively, and the last term is the intra-atomic *Spin-Orbit Coupling* (SOC). Our tight-binding model is based on four atomic orbitals,  $s$ ,  $p_x$ ,  $p_y$  and  $p_z$ . Both the intralayer and interlayer hoppings are described within the *Slater-Koster* (SK) formalism.<sup>61</sup> The intralayer hopping parameters are taken from Ref.<sup>64</sup> In order to study the effect of interlayer coupling, the interlayer terms are scaled by a dimensionless parameter  $\eta$ . When  $\eta = 1$ , the ratio between interlayer and intralayer  $V_{pp\pi}$  in graphene is taken as<sup>118</sup> 0.13. Unless otherwise

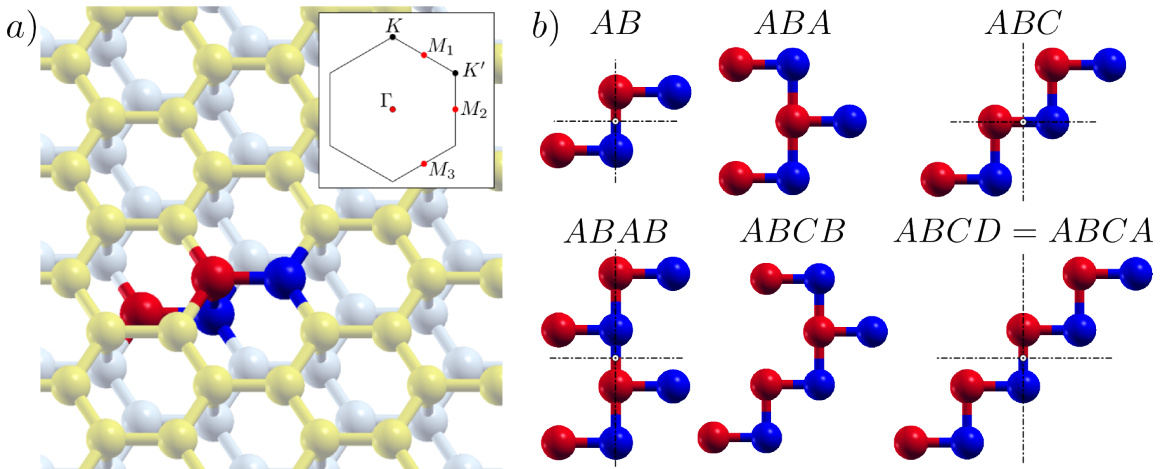


FIGURE C.1: a) Crystal structure of bilayer graphene system with a highlighted unit cell. Different colors for each layer are used to distinguish the two layers. In the inset the first Brillouin Zone is depicted with the high symmetry points and the Time Reversal Invariant Momenta colored in red. In b) Side view of the unit cells for all the different stackings studied. For the stackings with inversion symmetry the inversion center is shown at the crossing point of the dashed lines. For both figures red and blue denote sublattice.

stated, in all our calculations we have  $\eta = 1$ . Within this model, the dimension of the Hilbert space for the minimal unit cell of the crystal with  $N$  layers is  $4 \times 2 \times 2 \times N = 16N$  (4 orbitals per atom, 2 atoms per layer, plus the two possible spin orientations).

Without SOC, this model reproduces the very well known band structure of graphene ( $N = 1$ ) and multilayer graphene  $N > 1$ , that portraits these systems as zero-gap semiconductors. Within this model, SOC is known to open a gap in the monolayer<sup>70</sup> as well as in the bilayer.<sup>160–162</sup> In the case of the monolayer graphene the gap is known to be topological. Within this model, the computed value of the gap  $1.46 \mu\text{eV}$  when we take a realistic value of the atomic SOC,  $\lambda = 10 \text{ meV}$ . This gap is much smaller than the ones obtained with accurate DFT calculations,<sup>35</sup> in the range of  $\sim 30 \mu\text{eV}$ . The reason for the discrepancy turns out to be that the mayor contribution to the SOC gap at the Dirac point comes from the coupling to the higher energy  $d$  bands.<sup>35, 160</sup> The later is a simple consequence of the fact that SOC opens a gap in second order in the coupling in the Dirac points when projected over the  $p$  band. In comparison, SOC acts as first order when considering channels involving the  $d$  band. Nevertheless, interlayer hopping may open a first order spin flipping channel in the  $p$  manifold, becoming of the same order as the intrinsic spin

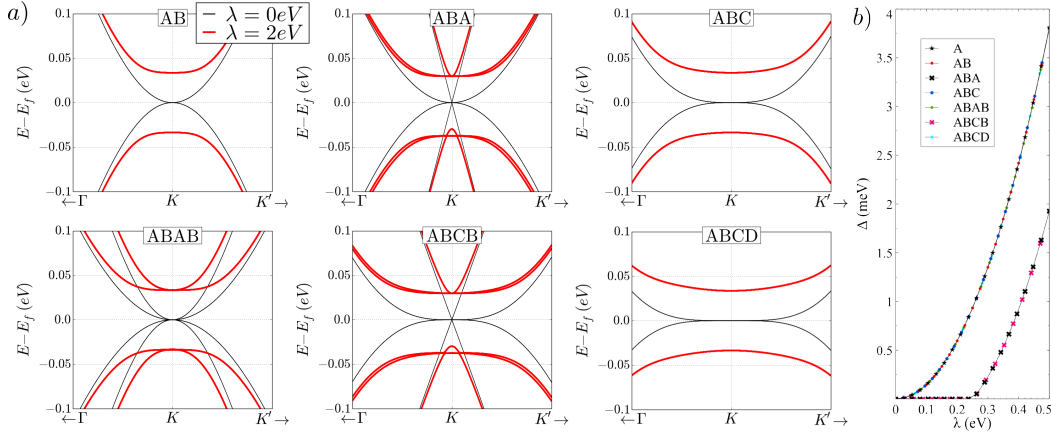


FIGURE C.2: In *a*) the band structure close to the  $K$  point is shown for all the possible stackings of multilayer graphene with  $N = 2, 3, 4$ . Only when  $\lambda \neq 0$  (red line) a gap is opened at the Dirac points. Note that for  $ABA$  and  $ABCB$  stackings there are linear bands when  $\lambda = 0$  that when the SOC is switched on cause a smaller gap than in the other cases. In *b*) the dependence of the gap with the SOC  $\lambda$  is shown. The anomalous behavior for the  $ABA$  and  $ABCB$  stackings is just due to the linear bands mentioned before.

conserving  $d$ -level contribution. These last processes would be the ones missing in the multilayer Kane-Mele model, and should be added for completeness. In our case, for the sake of simplicity, we will focus on the spin flipping channel, and use a four orbital tight-binding model considering  $\lambda$  as a free parameter.

Future work shall focus on the effect of the d-levels in multilayer graphene, which will not be addressed here.

The effect of SOC on the band structure of the multilayers can be summarized in the following points:

- 1) SOC opens up a gap for all the  $N$  stacked layers considered, reproducing the existing results<sup>161</sup> for the case of  $N = 2$ . Notice that in the case of  $ABA$  and  $ABCB$  stackings, the system remains gapless until a critical value of  $\lambda$ . This peculiarity is related to the non uniform evolution of the SO splitting of the linear and non-linear bands as shown in figure C.2.
- 2) The scaling of the gap with  $\lambda$  is very similar for monolayer and  $N = 2, 3, 4$  multilayers as it is shown in Figure C.2. Therefore, it is expected that within this model, the gap opened by the intrinsic SOC might be as small in multilayers as in monolayers.
- 3) The magnitude of the band-gap is insensitive to the interlayer coupling. This result is somewhat surprising, since together with atomic SOC the

interlayer coupling opens a spin-flip channel, otherwise missing in the monolayer case. For the  $AB$  bilayer, this can be understood considering the Hamiltonian at the Dirac point, for a given spin flavor. In the basis  $\{A_1, B_1, A_2, B_2\}$  the low energy Hamiltonian is given by

$$H(K) = \begin{pmatrix} \Delta/2 & 0 & 0 & 0 \\ 0 & -\Delta/2 & \eta t & 0 \\ 0 & \eta t^\dagger & \Delta/2 & 0 \\ 0 & 0 & 0 & -\Delta/2 \end{pmatrix} \quad (\text{C.2})$$

where  $\Delta$  is the SO gap. When  $\eta = 0$  this Hamiltonian represents two decoupled monolayers. For finite  $\eta$  the eigenvalues are  $E_\pm^1 = \pm\Delta/2$  and  $E_\pm^2 = \pm\sqrt{(\eta t)^2 + (\Delta/2)^2}$ . Since  $\eta t \gg \Delta$  the gap is still controlled by the  $E^1$  couple and thereby identical to that of the decoupled monolayers. As a result, switching on the interlayer coupling does not close the SOC gap of the monolayer as shown in Figure C.2. As a consequence, the ground state of two decoupled ( $\eta = 0$ ) monolayers can be adiabatically connected to the ground state of the bilayer ( $\eta = 1$ ).

The last observation leads to the following result: odd  $N$  stacked graphene will be quantum spin Hall Insulators, whereas even  $N$  will not. More precisely, for a system of  $N$  decoupled monolayers the  $Z_2$  invariant is:

$$Z_2(N) = [Z_2(1)]^N \quad (\text{C.3})$$

Since the gap opened by  $\lambda$  remains unaffected when switching on the interlayer coupling  $\eta$ , the value of  $Z_2$  for graphene-like multilayers is also given by equation eq. C.3. We have verified that this qualitative behavior remains unchanged when  $d$ -channels are included in the picture by performing all-electron DFT calculations. In the realistic low  $\lambda$  limit, the gap is controlled by the linear contribution in  $\lambda$ , namely the  $d$ -channel. For large SO, the quadratic in  $\lambda$   $p$ -channel becomes dominant, which corresponds to the situation in which the gap opening is properly captured by the SK model. Thus, by artificially increasing  $\lambda$  in a DFT calculation, it is possible to move from the  $d$ -dominated to the  $p$ -dominated SO gap. We have obtained that both limits are adiabatically connected without gap closing, so that the topological properties in the low  $\lambda$  limit are the same than in the large  $\lambda$  limit.

In the following we verify equation eq. C.3 using two different strategies. In the case of inversion symmetric structures, we compute the  $Z_2$  invariant. In all cases, we compute the edge states and check whether they fill the gap, or else. Independently on how the topological character is obtained, eq. eq. C.3 holds in all the cases.

### c.1.1 Calculation of the $Z_2$ invariant.

Using the method developed by Fu and Kane in 2007<sup>163</sup> for systems with inversion symmetry it is possible to determine easily its topological character (the  $Z_2$  invariant) by calculating the parity of the occupied Bloch wave functions at the time reversal invariant momenta (TRIMs).

$$\delta_i = \prod_{m=1}^N \xi_{2m}(\Gamma_i) \quad ; \quad (-1)^\nu = \prod_i \delta_i \quad (\text{C.4})$$

where  $\xi_{2m}$  is the parity eigenvalue of the  $2m^{th}$  occupied state at the TRIM  $\Gamma_i = \{\Gamma, M_1, M_2, M_3\}$ . Using this method the topological character of a system will be determined just by the quantity  $(-1)^\nu$ , resulting that  $(-1)^\nu = +1$  means trivial topology and  $(-1)^\nu = -1$  means non trivial topology. The calculation for the systems with inversion symmetry yields the following results:

	A	AB	ABC	ABAB	ABCD
$M_1$	+	+	+	+	+
$M_2$	+	+	+	+	+
$M_3$	+	+	+	+	+
$\Gamma$	-	+	-	+	+
$(-1)^\nu$	-	+	-	+	+

This guarantees that  $A$  and  $ABC$  crystals are topological but the bilayers and tetralayers (with inversion symmetry) are not. For systems without inversion symmetry, the calculation of the  $Z_2$  invariant requires a different approach<sup>164–166</sup> that requires a line integral of the Berry curvature over a contour in the Brillouin zone. Instead, we compute the edge states for these systems and invoke the bulk-edge correspondence to address the topological nature of those systems.

### c.1.2 Edge states

To confirm equation eq. C.3 even for systems without inversion symmetry we look for the presence of gapless edge states. We consider armchair-terminated semi-infinite crystals. Using translation invariance along the direction parallel to the edge, we block-diagonalize the Hamiltonian of the semi-infinite 2D crystal in terms of a collection of  $k_{||}$  dependent semi-infinite 1D Hamiltonians, as indicated in figure C.3. The 1D Hamiltonian describes unit cells with  $4N$  atoms, where  $N$  stands for the number of graphene layers. The intra-cell terms are denoted by  $H_0(k_{||})$  and the inter-cell hoppings by  $V(k_{||})$ .

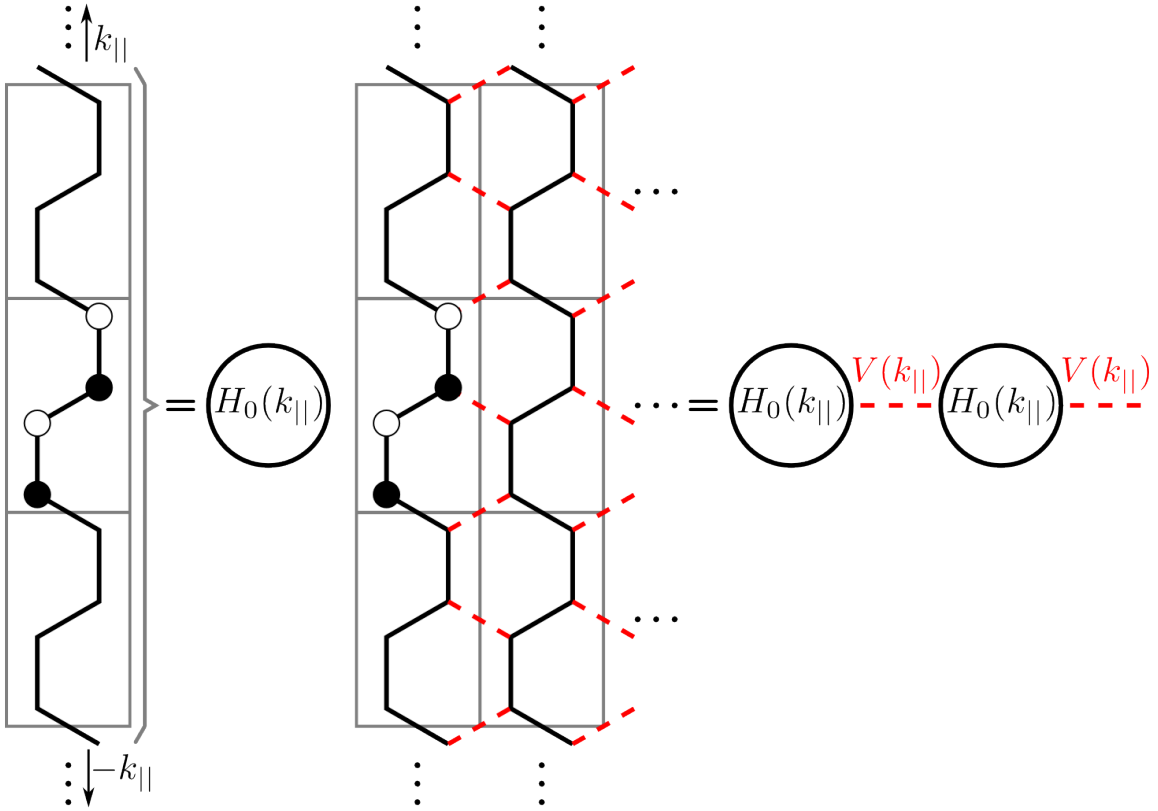


FIGURE C.3: Scheme of the mapping between a semi-infinite crystal and a semi-infinite chain. The coupling between each linear chain (with  $k_{||}$  well defined) is introduced by means of a self energy  $\Sigma_R$ .

The surface Green function of this block tridiagonal semi-infinite matrix can be written as:

$$G^{edge}(E, k_{||}) = [E + i\epsilon - H_0(k_{||}) - \Sigma_R(k_{||}) - \Sigma_H(k_{||})]^{-1} \quad (\text{C.5})$$

where  $\Sigma_R(k_{||})$  is a self-energy that accounts for the coupling to the semi-infinite crystal,  $\Sigma_H(k_{||})$  is the self-energy due to its interaction with the  $H$  atoms included to get rid of the dangling bonds and  $\epsilon$  a small analytic continuation.

The self-energy  $\Sigma_R$  can be calculated employing a recursive Green's function method that leads to the following coupled equations

$$\begin{aligned} \Sigma_R(E, k_{||}) &= V_R(k_{||}) g_R(E, k_{||}) V_R^\dagger(k_{||}) \\ g_R(E, k_{||}) &= [E - H_0(k_{||}) - \Sigma_R(E, k_{||})]^{-1} \end{aligned} \quad (\text{C.6})$$

The  $\Sigma_H(k_{||})$  is calculated just as an additional iteration to the self-consistent calculation with the appropriate value for the hoppings  $C - H$ .

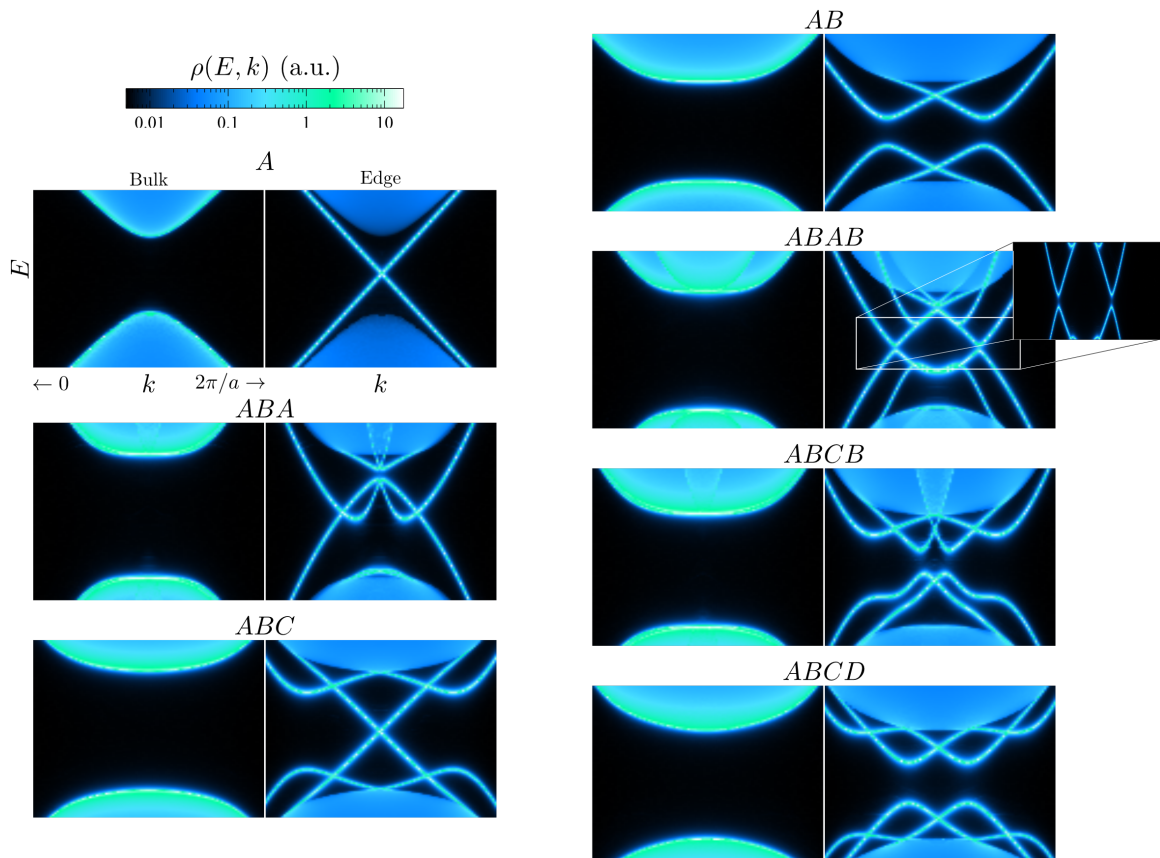


FIGURE C.4: For each structure bulk and edge *Density of States* (DOS) (left and right panel respectively). Gapless edge states appear only when an odd number of layers is considered independently of the stacking used.

For a given  $k_{\parallel}$  we compute the DOS using

$$\rho(E, k_{\parallel}) = -\frac{1}{\pi} \text{Im}[G^{\text{edge}}(E, k_{\parallel})] \quad (\text{C.7})$$

Using a similar approach we can also obtain the bulk DOS calculating the bulk Green function by recursion.

In figure C.4 we show the DOS for both bulk and edge for all the stackings as a contour plot in the  $k_{\parallel}, E$  plane. For each stacking the left panel shows the bulk DOS, which are gaped for all the stackings and the right panel shows the edge states. The calculations are done for a rather large value of  $\lambda = 2 \text{ eV}$ . The first thing to notice is that, for such large values of  $\lambda$ , all the structures have edge states. However, only in the case of odd  $N$ , shown in the left column, the in-gap states are gapless. This is a necessary condition in order to have a *Quantum Spin Hall Insulator* (QSHI). In contrast, all systems with even  $N$  have edge states with a gap. Thereby, they are definitely not in the *Quantum Spin Hall* (QSH) phase, validating equation eq. C.3 . Therefore, we conclude that odd  $N$  graphene stacks are QSHI and even  $N$  are trivial insulators. In all cases, the gap opened by SOC is quite small.

### c.1.3 *Heterogeneous multilayers*

In the previous section we have seen that for homogeneous multilayers the gap opened by SOC has the same magnitude than for the monolayer. Thereby, homogeneous multilayers of graphene would not improve the prospects for observation of the QSH phase compared to the monolayer. We thus explore the case of a heterogeneous multilayer. This is motivated in part by recent experiments<sup>167</sup> that seem to indicate an enhancement of the SOC interaction in graphene due to proximity to  $WS_2$ , a trivial semiconductor with quite large SOC and no inversion symmetry. There has also been plenty of work studying the enhancement of SOC interaction in graphene due to proximity to heavy metals.<sup>168</sup> However, it would be much more interesting if graphene could be driven into a QSH phase by proximity to an insulator, so that the only conducting channels would be only at the edges of graphene.

Density functional calculations show<sup>169</sup> that a topological band-gap opens in graphene on top of both  $WS_2$  and  $WSe_2$ , two widely studied two dimensional *Transition Metal Dichalcogenides* (TMD). The magnitude of this gap is in the range of a few meV, i.e., two or three orders of magnitude larger than the intrinsic SOC gap.

Here we propose a toy model to understand the opening of a non-trivial gap due to proximity to a trivial insulator with strong SOC. For that matter, we

take graphene encapsulated between two monolayers of a trivial semiconductor with strong SOC and broken inversion symmetry. Specifically, the structure of these adjacent monolayers is that of a *BN*-like crystal (see figure C.5(a)). The choice of the stacking is such that, globally, the structure has inversion symmetry. Otherwise, a trivial band gap would be opened by proximity.<sup>170</sup>

The *BN*-like crystal is described with the same interatomic SK parameters than graphene, but very different on-site parameters. In particular we assume a large SOC  $\lambda$  and a staggered potential  $\pm m$  that breaks inversion symmetry of the top and bottom layers. Since we are interested in the proximity effect, we turn off the atomic SOC of the graphene layer. As in the case of the homogeneous multilayers, the interlayer coupling is characterized by the dimensionless parameter  $\eta$ . In this case we impose zero SOC for the graphene layer, in order to study the proximity effect. For  $\eta = 0$  the bands of this system would be the superposition of those of the top and bottom insulators, with gap  $2m$ , and the bands of graphene, whose Dirac cones would lie inside the gap. Broadly speaking, this picture remains the same as the interlayer coupling is turned on. Interestingly, a non-trivial gap  $\Delta$  opens in the Dirac cones only when  $\eta \neq 0$  and  $\lambda \neq 0$ . We have verified that this gap satisfies the scaling

$$\Delta \propto \frac{\lambda\eta^2}{m^2} \quad (\text{C.8})$$

in the limit of small  $\lambda$ ,  $\eta$  and  $m^{-1}$ . This results implies that graphene can borrow SOC from a neighbor trivial insulator layer via interlayer coupling. Using the method of the TRIM we have verified that this insulator has  $Z_2 = (-1)^\nu = -1$ , and is therefore topologically non-trivial.

The magnitude of the proximity effect away from the weak coupling limit of eq. eq. C.8 is shown in figures C.5. We study the dependence of the proximity gap  $\Delta$  as a function of both the SOC  $\lambda$  and the interlayer coupling  $\eta$  for two values of the encapsulating layer staggered potential  $m$ . It is apparent that, taking  $m = 2.0$  eV (a trivial gap  $\sim 1.5$  eV) and  $\lambda \simeq 0.25$  eV, values in line with those of 2D TMD, the proximity gap is in the order of  $\sim 1$  meV, similar to the DFT results. Therefore, our model provides a reasonable justification of the DFT computations, which are certainly more complete.

Our toy model does not capture some probably important features of real heterogeneous multilayers. For instance, the interlayer interaction could break inversion symmetry which is expected to open a trivial gap. In addition, the geometry of our encapsulating layers was chosen to minimize the size of the unit cell, rather than to describe a real material. In general, the coupling of graphene to other 2D crystals will imply a new length scale, given by the size of

the new unit cell. In this setup, the inversion symmetry breaking could average out.

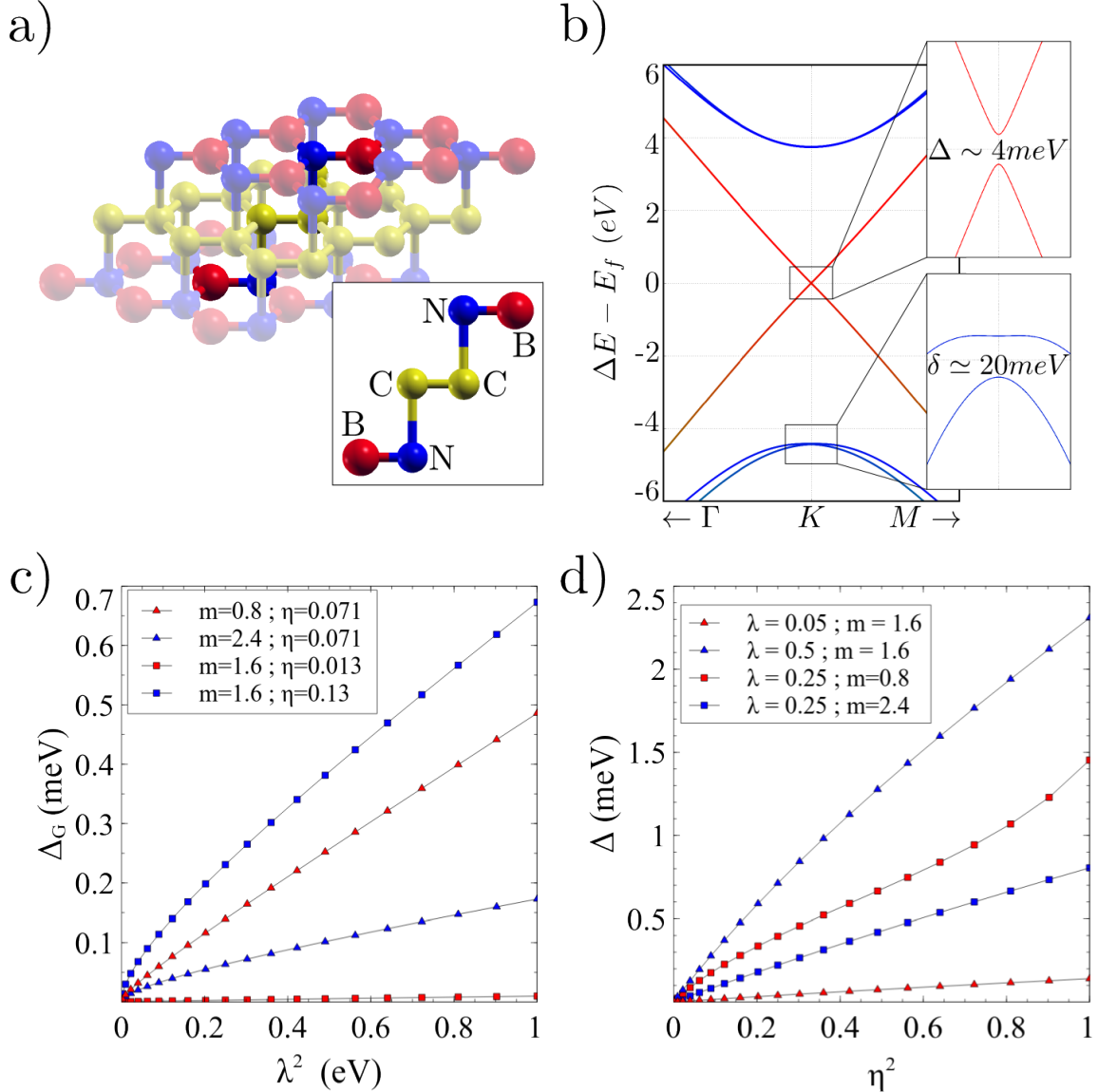


FIGURE C.5: Panel *a*) shows the structure of the heterostructure considered. Panels (b,c,d) show the dependence of the induced gap in graphene due to the proximity of the encapsulating layers. In panel *b*) it can be seen that the gap is proportional to  $\lambda^2$  and this estimation gets better as the gap of insulating layers gets bigger. Panel *b*) shows how the interlayer coupling  $\eta$  produces the expected effect, for small interlayer coupling the induced gap is small but it grows quickly as  $\eta$  increases. Panel *c*) shows the dependence of the induced gap with the sublattice imbalance

# Real space mapping of topological invariants using artificial neural networks

---

## D.1 INTRODUCTION

The study of topological electronic phases is one of the central topics in modern Condensed Matter Physics. Depending on the symmetry class different topological states exist, with the paradigmatic examples of time reversal topological insulators,<sup>171</sup> topological superconductors,<sup>172</sup> topological crystal insulators,<sup>173</sup> topological Kondo insulators<sup>174</sup> and topological Mott insulators<sup>175</sup> among others. The most fundamental quantity to characterize these states is the so called topological invariant, whose value determines the topological class of the system. In particular, interfaces between systems with different topological invariants show topologically protected excitations, resilient towards perturbations respecting the symmetry class of the system. Computationally, the calculation of the topological invariant usually requires the explicit knowledge of the wavefunctions of the entire system.<sup>176–178</sup> In particular, topological invariants can be calculated as the winding number of the occupied wave functions under twisted boundary conditions.<sup>176–178</sup> In that way, these methods generically require computing the full wavefunctions, that becomes a cumbersome task for systems without translational symmetry consisting on thousands of atoms.

In several situations of experimental relevance, translational symmetry is broken and systems are able to show different phases in real space due to the spatial modulation of the effective parameters. This situation might lead to protected modes between different regions of the system, dramatically changing the low

energy properties of the whole material. This is the natural scenario in van der Waals heterostructures, where Moire patterns<sup>179–181</sup> could coexist with any topological state.<sup>182,183</sup> A more controlled situation is the proposals for topological superconductivity involving nanowires, where the topological state is controlled *locally* by electric gates.<sup>184,185</sup> Even though real space formulations for the topological invariant do exist,<sup>186–190</sup> their computation requires an integration over the whole space. Thus, there is not a simple methodology to obtain a topological invariant in inhomogeneous systems by evaluating solely their local properties.

Application of Machine learning methods in Condensed Matter Physics is a growing area. A significant advantage of these techniques is that they are capable of finding the important degrees of freedom of a dataset without needing a profound insight of the treated problem. The identification of phase transitions<sup>191–196</sup> and the study of the ground state and correlations in different quantum many body problems<sup>197–202</sup> are just some of the problems that Machine Learning has helped tackle in the past few years. Even some techniques have been used in combination with *ab initio* calculations allowing a broader and more accurate understanding of materials.<sup>203–205</sup> Within the language of machine learning, the calculation of topological invariants is understood as a simple classification algorithm,<sup>206,207</sup> that could be efficiently tackled with the so called artificial neural networks.<sup>208–213</sup>

In this manuscript we show that artificial neural networks (ANN) are capable of characterizing the local topology of a system using as input a restricted amount of real space information. In particular, we show that a trained ANN identifies correctly the local topological character in spatially varying Hamiltonians that create topologically different regions in space. Importantly, we show that this technique, used in conjunction with the kernel polynomial method, allows to compute local topological invariants with an algorithm whose computational cost scales just linearly with the size of the system.

The rest of the paper is organized as follows. In section D.2 we review the basics of artificial neural networks (Sec. D.2.1) and summarize the use of the kernel polynomial method to efficiently compute density matrices (Sec. D.2.2). In section D.3 we apply the combined ANN-KPM technique both to a model Hamiltonian for a 1-D topological superconductor (Sec. D.3.1) and a 2-D anomalous Hall insulator (Sec. D.3.2). Finally, in section D.4 we present our conclusions.

## D.2 METHOD

### D.2.1 Artificial Neural Networks

Machine Learning (ML) is a broad field that includes many different approaches, goals and methods.<sup>214</sup> The defining property of ML algorithms is that they allow computers to perform specific tasks without being explicitly programmed for each one of them.<sup>215</sup> Within the vast variety of ML algorithms, we will focus on supervised learning algorithms, which require a training dataset to fit the parameters in the model. One of the most common models of supervised learning are *Artificial Neural Networks* (ANN) which have been proven very useful to model patterns and correlations of complex problems that cannot be modeled analytically such as image or sound recognition,<sup>208–210</sup> and even natural language processing.<sup>211, 212</sup> In our case, we aim to use an artificial neural network to characterize locally the topological state of a one (Fig. D.1 (a)) or two (Fig. D.1 (b)) dimensional system. The objective of the procedure is to have a neural network that, given local information about the system, returns the topological invariant as sketched in Fig. D.1 (c). The local information that will be provided is a local block of the density matrix of the system, as we will discuss later.

ANN are loosely based on parts of the brain, consisting of neurons, modeled as perceptrons,<sup>216</sup> and synapses as shown in Fig. D.1 (a). The neurons in an ANN do not attempt to model the actual structure or behavior of the biological cells.<sup>217</sup> Instead, they mimic one of their main features, the activation function. This activation function,  $\sigma$ , sketched in Fig. D.1 (b) provides the output of each neuron based on the received inputs and an external parameter (bias). For computational convenience,  $\sigma$  should be any smooth and differentiable function defined over  $\mathbb{R}$  but with its range restricted to a closed interval, namely  $\sigma \in [-1, 1]$ , as depicted in Fig. D.1 (e). Usually, these functions are either the tanh or the sigmoid function, but others might be used without loss of generality or functionality since these models are only weakly sensitive to these details.<sup>218</sup>

The inputs  $X$  entering each neuron are weighted by the synapses  $W$  and shifted by the bias  $b$ . The synapses' weights are parameters to be tuned and they can be arranged as rectangular matrices,  $W^\alpha$ , so the output  $L$  of the layer  $\alpha$  can be obtained simply as:  $L_\alpha = \sigma(X_\alpha \cdot W_\alpha + b_\alpha)$ , where  $X_\alpha$  is the input of the layer  $\alpha$  (note that for the hidden layers  $X_\alpha = L_{\alpha-1}$ ). As a formative

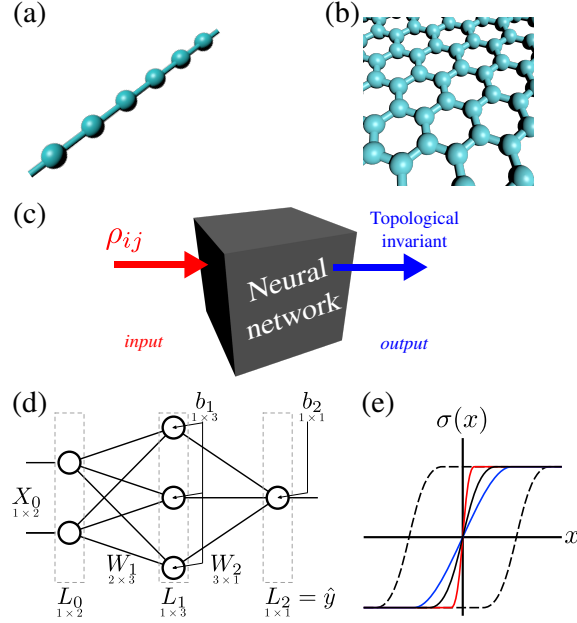


FIGURE D.1: Panels (a,b) show a cartoon of the two different geometries of the model Hamiltonians considered below, a one dimensional topological superconductor (a) and a two dimensional quantum anomalous Hall insulator (b). Panel (c) shows a schematic sketch of our procedure: a trained neural network will take as input a local density matrix, and it will return the topological invariant of the system. Panel (d) shows a sketch for an artificial neural network as described in the text, whereas in (e) we sketch the standard behavior of an activation function of a neuron,  $\sigma(x)$ , for different weights (colors) and bias (dashed lines).

example the outputs of every layer of the toy model sketched in Fig. D.1 (d) can be calculated as follows:

$$\begin{aligned} L_0 &= \sigma(X_0) \quad \text{or just} \quad L_0 = X_0 \\ L_1 &= \sigma(L_0 \cdot W_1 + b_1) \\ L_2 &= \sigma(L_1 \cdot W_2 + b_2) = \hat{y} \end{aligned} \tag{D.1}$$

where  $X_0$  is the input fed to the ANN. The matrices  $W_\alpha$  and the arrays  $b_\alpha$  are the parameters to be fitted during the training process in order to modify the activation functions of each of the neurons in the ways showed in Fig. D.1 (e). Note that the number of parameters in ANN models grows very quickly with the size (number of neurons per layer) and depth (number of layers) of the network.

Artificial neural network, as every supervised learning algorithm, consist in three phases. First, the architecture of the model (i.e. the number of layers and neurons per layer) is decided depending on the complexity of the prob-

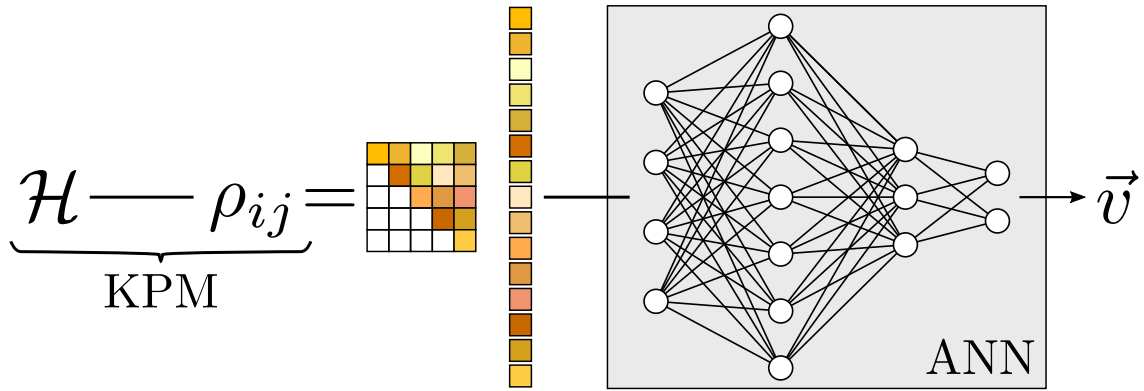


FIGURE D.2: Sketch of the process to evaluate the topological character of a local region of space. The density matrix corresponding to a certain area in space is calculated using the KPM, after removing the redundant elements the matrix is rearranged in a 1D array that is used as input for neural network that will provide the corresponding topological invariant as output.

lem addressed. Second, the model is trained. In this process, several input-output pairs are provided to the model whose parameters are fitted to mimic the correlations present in the user-provided data. Finally, when the training is completed, the model can be used to evaluate new (unseen) input data.

Supervised learning algorithms require a training dataset to optimize the parameters of the models. The training is performed by minimizing a cost function,  $\mathcal{E}$ , usually proportional to the squared difference between the expected output,  $y$ , and the actual output of the network,  $\hat{y}$ .

$$\mathcal{E} = \frac{1}{2}(y - \hat{y})^2 \quad (\text{D.2})$$

Notice that  $y$  is a constant defined by the (user-provided) training dataset while  $\hat{y}$  depends on all the parameters of the network (weights and bias). The minimization of  $\mathcal{E}$  is, then, performed by iteratively modifying the values of all the weights and bias in the network until the desired output is obtained. This is a computationally complex and expensive process since the number of parameters can range from a few tens to millions. In fact, it was not until 1986 that an efficient method was developed for such a purpose.<sup>219</sup> We use the gradient descent with the back-propagation algorithm to train the ANN, which is the most common approach nowadays. We used the open source library PyBrain,<sup>213</sup> to create, train and evaluate the ANN.

### D.2.2 Correlation functions with the Kernel Polynomial method

In this section we review how real space correlation functions can be efficiently calculated using the Kernel polynomial method (KPM).<sup>122</sup> We will focus the discussion in the case of a normal electronic system, since the case of a superconductor can be treated in an analogous way. The main task that we have to perform is to obtain the density matrix, evaluated in a restricted area of real space, of a certain (very large) Hamiltonian. In terms of the eigenfunctions  $|\Psi_k\rangle$  of the Hamiltonian  $H$ , the elements of the density matrix can be written as

$$\rho_{ij} = \int_{-\infty}^{E_F} \langle i | \Psi_k \rangle \langle \Psi_k | j \rangle \delta(E_k - \omega) d\omega \quad (\text{D.3})$$

where  $|i\rangle$  and  $|j\rangle$  are the elements of the basis for the Hamiltonian  $H$  and  $E_F$  is the Fermi energy. The diagonal elements of the matrix,  $\rho_{ii}$ , are the integrated local density of states. In the gapped state, the off-diagonal elements are expected to decay exponentially with distance. So, when the Fermi energy  $E_F$  lies in the gap, the density matrix is properly described by restricting the calculation to a set of neighboring sites. Generically, calculating the previous matrix requires diagonalizing the full Hamiltonian to obtain the occupied wavefunctions, a task that scales with  $\mathcal{O}(N^3)$ , with  $N$  the system size of the system. The Kernel Polynomial Method allows the computation of  $\rho_{ij}$ , for a restricted set of neighboring sites, with a computational cost that scales only as  $\mathcal{O}(N)$ .

The KPM allows to compute the quantity

$$g_{ij}(\omega) = \sum_k \langle i | \Psi_k \rangle \langle \Psi_k | j \rangle \delta(E_k - \omega) \quad (\text{D.4})$$

which can easily be integrated to obtain the density matrix eq. D.3. The central idea is that  $g_{ij}$  can be expressed in matrix form as

$$g_{ij}(\omega) = \langle i | \delta(H - \omega) | j \rangle \quad (\text{D.5})$$

The KPM consists on expanding equation eq. D.5 in terms of Chebyshev polynomials  $T_n(\omega)$ . To do so, the Hamiltonian is first rescaled so that all the eigenenergies lie in the interval  $\mathcal{E}_k \in (-1, 1)$ . The rescaled Hamiltonian is denoted as  $\mathcal{H}$ . The corresponding spectral function is calculated as

$$g_{ij}(\omega) = \frac{1}{\pi\sqrt{1-\omega^2}} \left( \bar{\mu}_n + 2 \sum_{n=1}^N \tilde{\mu}_n T_n(\omega) \right) \quad (\text{D.6})$$

The coefficients  $\tilde{\mu}_n$  determine the expansion of a certain element  $g_{ij}$ , and are calculated as

$$\tilde{\mu}_n = g_n^N \mu_n \quad (\text{D.7})$$

where  $\mu_n$  are the coefficients calculated from the Hamiltonian  $\mathcal{H}$  and  $g_n^N$  denotes the Jackson Kernel that improves the convergence of the series<sup>122,123</sup>

$$g_n^N = \frac{(N - n - 1) \cos \frac{\pi n}{N+1} + \sin \frac{\pi n}{N+1} \cot \frac{\pi}{N+1}}{N + 1} \quad (\text{D.8})$$

Given two sites  $i$  and  $j$ , we define two vectors located in those sites  $v_i$  and  $v_j$ . The coefficients  $\mu_n$  would be calculated as a conventional functional expansion

$$\mu_n = \langle v_i | \int_{-1}^1 \delta(\mathcal{H} - \omega) T_n(\mathcal{H}) d\omega | v_j \rangle \quad (\text{D.9})$$

which in the diagonal basis reads

$$\mu_n = \int_{-1}^1 \langle v_i | \Psi_k \rangle \delta(\mathcal{E}_k - \omega) \langle \Psi_k | v_j \rangle T_n(\omega) d\omega \quad (\text{D.10})$$

Performing the integration over  $\omega$  we get

$$\mu_n = \langle v_i | \Psi_k \rangle T_n(\mathcal{E}_k) \langle \Psi_k | v_j \rangle = \langle v_i | T_n(\mathcal{H}) | v_j \rangle \quad (\text{D.11})$$

Therefore, the coefficients  $\mu_n$  can be calculated as the overlap of two vectors

$$\mu_n = \langle v_j | \alpha_n \rangle \quad (\text{D.12})$$

where  $\alpha_n$  is calculated with the recursion relations associated to the Chebyshev polynomials

$$\begin{aligned} |\alpha_0\rangle &= |v_i\rangle \\ |\alpha_1\rangle &= \mathcal{H}|\alpha_0\rangle \\ |\alpha_{n+1}\rangle &= 2\mathcal{H}|\alpha_n\rangle - |\alpha_{n-1}\rangle \end{aligned} \quad (\text{D.13})$$

This procedure thus involves matrix vector products to calculate the coefficients. For a sparse matrix, as it is the case of a tight binding Hamiltonian, the number of non-zero elements scales linearly with the system size, so the computational cost of calculating the density matrix for a fixed number of sites also scales linearly. This method allows to compute  $g_{ij}$  at every energy simultaneously, so that  $\rho_{ij}$  can be calculated by integration up to the Fermi energy.

For small systems, the density matrix can be calculated also by exact diagonalization of the full Hamiltonian. In principle, that procedure allows to calculate the correlation function of relatively large one dimensional systems. However, for a two dimensional system, the dimension of the matrix will be too large in general. It is in that situation when the kernel polynomial method is specially suitable.

### D.3 TOPOLOGICAL INVARIANTS WITH SUPERVISED LEARNING

We now describe the procedure to characterize the local topological character of a system using ANN. We choose as input the elements of the density matrix that involve one site and its closest neighbors. This procedure allows to naturally treat systems without translation symmetry and with disorder, as the calculation of the density matrices is not more computationally expensive in those situations using the previous procedure. The process to calculate the density matrix was discussed in Sec. D.2.2 but in order to use the density matrix as input for our ANN some processing is required. The density matrix is, in general, a complex Hermitian matrix, so we will remove the redundant elements (namely the lower triangle) and arrange the remaining elements in a 1D array, concatenating the real and imaginary parts. Furthermore, we included the eigenvalues of the density matrix as part of the input. Strictly, the inclusion of the eigenvalues is a redundant operation that could be avoided by increasing the size and/or depth of the ANN, yet we found that it helped the optimization of the model with a negligible computational overhead. The output of the ANN will be the topological invariant of the system. The calculation of the corresponding output is done by constructing a translational invariant Hamiltonian in which the corresponding topological invariant is well defined and can be calculated in a standard way. Finally, since we are using the ANN as a classifier, it is convenient to encode the possible outputs as linearly independent vectors,  $\vec{v}$ , rather than use a single scalar. The use of vectors allows the discrimination between wrong answers and false positives. This whole architecture is sketched in Fig. D.2.

In order to train of the ANN we generate a large number of realizations of a family of Hamiltonians, exploring their parameter space. For a given choice of parameters, we compute the topological invariant of the corresponding pristine case and its local density matrix. These procedure allows us to generate a set of inputs and outputs, which are used to train the NN. Once the ANN is trained, the model is ready to be evaluated with new data that the network has never tried to test the accuracy of the network. The last step is to create a new Hamiltonian with spatially dependent parameters, and evaluate the ANN with the local density matrix corresponding to a neighborhood of every lattice site. In this way, we have a procedure to locally evaluate the topological invariant of a systems lacking translational symmetry.

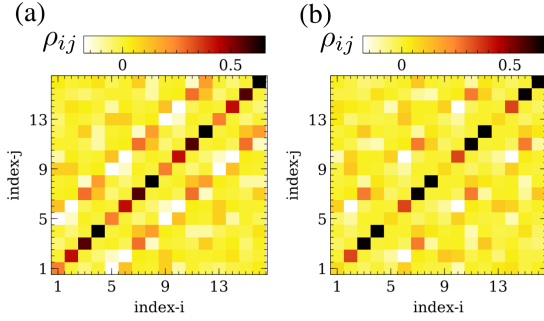


FIGURE D.3: Image representation of the density matrix for two particular different states for the superconducting 1D system, trivial (a) and topological (b). In terms of the matrices shown, the task of the neural network can be understood as an image recognition algorithm capable of distinguishing an input (a) from (b), for different parameters of the Hamiltonian chosen randomly. The different indexes in x and y axis run over spin and electron/hole sectors in the closest sites.

### D.3.1 One dimensional topological superconductor

In the following, we will consider a lattice model Hamiltonian for a one dimensional electron gas that is able to host both trivial and topological superconducting states. The corresponding topological invariant is a  $Z_2$  number that can be calculated as a Berry phase.<sup>220</sup> Such effective one dimensional system, in particular the superconducting topological phase, is realized in semiconducting nanowires deposited on top of a s-wave superconductor.<sup>221–227</sup> The model describes electrons in a 1D chain, in the presence of Zeeman field, Rashba spin-orbit coupling, superconducting proximity effect and a sublattice imbalance term. Thus, the model has six different parameters: a spin-conserving hopping  $t$ , chemical potential  $\mu$ , Rashba spin orbit  $t_R$ , external Zeeman field  $B_z$ , on-site pairing term  $\Delta$  and a trivial mass  $m$ . Moreover, we also include the possibility of having finite Anderson disorder  $W_i$ , so that the full Hamiltonian reads

$$\begin{aligned} \mathcal{H} = & -t \sum_{\langle ij \rangle_\alpha} c_{i\alpha}^\dagger c_{j\alpha} + it_R \sum_{\langle ij \rangle_{\alpha\beta}} \hat{e}_z \cdot (\vec{\sigma}_{\alpha\beta} \times \vec{d}_{ij}) c_{i\alpha}^\dagger c_{j\beta} \\ & + B_z \sum_{i\alpha} c_{i\alpha}^\dagger \sigma_z c_{i\alpha} + \Delta \sum_i [c_{i\uparrow}^\dagger c_{i\downarrow} + c_{i\downarrow}^\dagger c_{i\uparrow}] \\ & + \mu \sum_{i,\alpha} c_{i\alpha}^\dagger c_{i\alpha} + m \sum_i \tau_i c_i^\dagger c_i + \sum_{i,\alpha} W_i c_{i\alpha}^\dagger c_{i\alpha} \end{aligned} \quad (\text{D.14})$$

The previous Hamiltonian can have topological and trivial phases. In a nutshell, a topological phase may arise when the Zeeman term  $B_z$  is such that

the chemical potential  $\mu$  crosses only one of the spin channels, so that a small pairing  $\Delta$  and Rashba field  $t_R$  gives rise to a spinless p-wave superconductor.<sup>225</sup> In the absence of both Zeeman and Rashba couplings, the induced superconducting gap is trivial.

The Hamiltonian eq. D.14 is solved in the Nambu representation by defining a spinor wavefunction as  $\Psi^\dagger = (c_\uparrow^\dagger, c_\downarrow^\dagger, c_\downarrow, -c_\uparrow)$  which gives rise to a Bogoliubov-de-Gennes Hamiltonian  $\mathcal{H} = \frac{1}{2}\Psi^\dagger H \Psi$ . The matrix  $H$  is used to calculate the correlation functions  $\langle c_{i,s} c_{j,s'} \rangle$  and  $\langle c_{i,s}^\dagger c_{j,s'} \rangle$ , as introduced in section D.2.2, by integrating the different  $g_{ij}(\omega)$  from  $\omega = -\infty$  up to  $\omega = 0$ . In Fig. D.3 we show an example of two different input data from the training dataset, for a topological (a) and a trivial (b) state computed for an open chain with  $N = 400$  sites using the KPM. It is evident that simple inspection is not enough to distinguish between the two of them.

In order to generate the training dataset we considered different Hamiltonians for a bipartite chain with 400 sites by varying the different values for the off-plane Zeeman field  $B_z$ , Rashba  $\lambda_R$ , chemical potential  $\mu$ , superconducting pairing  $\Delta$  and sublattice imbalance  $m$ . In order to prove the robustness of our procedure, we also switch on the Anderson on-site disorder ( $W \in (0.0, 0.4t)$ ), with a magnitude comparable to the other energy scales. For the training dataset we generated 1000 different Hamiltonians with parameters randomly chosen in the following ranges:  $t_R \in [-0.3t, 0]$ ,  $B_z \in [0.2t, 0.8t]$ ,  $\mu \in [t, 2t]$ ,  $\Delta \in [0.1t, 0.3t]$ ,  $m \in [-0.2t, 0.2t]$ , yielding a five dimensional phase space. Using the generated Hamiltonians we calculate the density matrix of the central atom in the nanowire,  $\rho_{ij}$ , and its three closest neighbors. Since the Hamiltonian in eq. eq. D.14 only involves two Pauli matrices for a linear chain, the Hamiltonian in real space can be chosen to be purely real, so that its density matrix will be also real. For each example the  $Z_2$  topological invariant is calculated for the pristine system ( $W_i = 0$ ) defined by that particular set of parameters, which is used as expected output. Since this topological invariant only has two possibilities, we encode the  $Z_2$  invariant as a two dimensional vector  $v$ , so that the topological case corresponds to  $v = (1, 0)$  and the trivial case to  $v = (0, 1)$ . With this methodology a single element of the training dataset has a 152-dimensional input and a 2-dimensional output. We took two hidden layers with 101 and 21 neurons. After training, a validation set with 200 new samples is generated to test the accuracy of the ANN yielding an accuracy of  $\sim 97\%$ . In order to gain some insight on the ANN capabilities, we run a simple test by freezing all the parameters in the Hamiltonian eq. D.14 but the chemical potential and comparing the actual  $Z_2$  with the output provided by

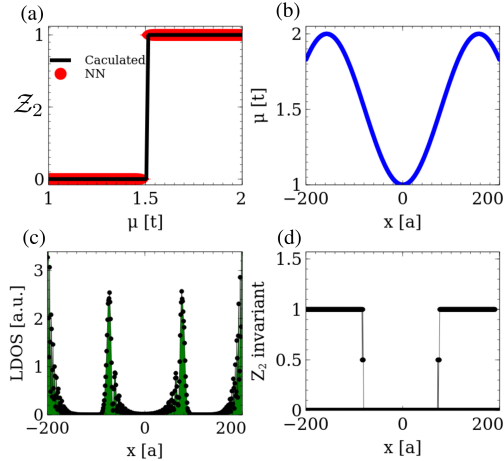


FIGURE D.4: (a) Comparison of the topological invariant computed exactly with the one predicted by the trained neural network in a pristine system, showing that the ANN perfectly captures the phase transitions in the homogeneous system. Afterwards, we create an inhomogeneous system with modulated chemical potential as shown in panel (b). Such modulation creates trivial and topological zones, with Majorana modes pinned at the transition points (c). The neural network is then evaluated in every point of the space, yielding a site-dependent topological invariant shown in (d). The topological transitions shown in (d) mark the existence of zero Majorana modes obtained in (c). The parameters used are  $\lambda_R = -0.3t$ ,  $B_z = 0.5t$ ,  $m = 0$ , and  $\Delta = 0.1t$ .

the ANN. In Fig D.4 (a) we see that even for unseen data the ANN is able to provide the correct topological invariant.

Once the network is trained, it is ready to be used in the case of an inhomogeneous system. We now generate a one dimensional system following equation eq. D.14 with spatially varying couplings. In particular, we modulate the chemical potential along the chain as shown in Fig. D.4 (b). Such modulation is feasible by means of local gates in the experimental realizations involving semiconducting nanowires.<sup>185</sup> With such modulation, we observe the emergence of zero energy modes in the local density of states D.4 (c), which are expected to be a signature of a boundary between a trivial and topological phase. The evaluation of the topological invariant on every atomic position of the chain can be carried out by feeding the local density matrix to the trained neural network. Our network shows that the different regions of the space have different topological invariants as shown in Fig. D.4 (d). It is observed that the points of space where the topological invariant changes in Fig. D.4 (d) correspond to the location of the zero energy Majorana modes, as seen in Fig. D.4 (c), validating the performance of our neural network.

The success of the neural network in describing the topological order of the different phases implies that, locally, the density matrix carries enough information to distinguish between the two cases. In particular, the elements of  $\rho_{ij}$  involving  $\langle c_{i,s} c_{j,s'} \rangle$  encode information about the induced superconducting order parameter, both in the  $s$  and  $p$ -wave channels, which physically is expected to determine the topological phase. If, in comparison, only the diagonal part of the density matrix was used as input for the neural network, it would not be possible to distinguish between trivial and topological states. This is easily understood taking into account that the diagonal part of  $\rho_{ij}$  accounts for the total occupation numbers and two topologically inequivalent band-structures can have arbitrarily similar density of states.

### D.3.2 Two dimensional Chern insulator

In this section we will use an analogous methodology to study a topological two dimensional state. In particular, we consider a model Hamiltonian for electrons moving in a honeycomb lattice with Rashba spin orbit coupling  $t_R$ , off-plane exchange  $B_z$ , that is known to result in a two dimensional Quantum Anomalous Hall state (QAH):<sup>228</sup>

$$\begin{aligned} H = & -t \sum_{\langle ij \rangle_\alpha} c_{i\alpha}^\dagger c_{j\alpha} + i t_R \sum_{\langle ij \rangle_{\alpha\beta}} \hat{e}_z \cdot (\vec{\sigma}_{\alpha\beta} \times \vec{d}_{ij}) c_{i\alpha}^\dagger c_{j\beta} \\ & + B_z \sum_{i\alpha} c_{i\alpha}^\dagger \sigma_z c_{i\alpha} + m \sum_{i,\alpha} \tau_i c_{i\alpha}^\dagger c_{i\alpha} \\ & + \sum_{i,\alpha} W_i c_{i\alpha}^\dagger c_{i\alpha} \end{aligned} \quad (\text{D.15})$$

where  $t_R$  is the Rashba coupling,  $\vec{\sigma}$  are the spin Pauli matrices,  $B_z$  is the external Zeeman field and  $\tau_i = \pm 1$  is the sublattice operator. The first term is the usual tight-binding hopping term, the second one describes the Rashba interaction<sup>70, 228</sup> and the third term is the so-called exchange or Zeeman term which couples to the spin degree of freedom. The fourth term is a trivial mass term that assigns an opposite on-site energy for the atoms in each of the sublattices, that we introduce in order to have a trivial insulator phase in the model. Finally, the last term is an Anderson disorder term that we introduce to prove the robustness of the procedure. For  $m = 0$ , and  $B_z \neq 0$  and  $t_R \neq 0$ , the model has a topological gap with a Chern number  $\mathcal{C} = \pm 2$ . For  $m \neq 0$  and  $B_z = 0$ , the model has a trivial ( $\mathcal{C} = 0$ ) gap.

Each of these Hamiltonian terms can effectively describe different experimental situations. The sublattice imbalance could arise for a graphene monolayer deposited on boron nitride in a commensurate fashion.<sup>181, 229</sup> The Rashba and exchange fields naturally arise for a graphene monolayer deposited over a ferromagnetic insulator, such as YIG,<sup>230, 231</sup> EuO<sup>232</sup> or CrI<sub>3</sub>.<sup>233, 234</sup> Furthermore,

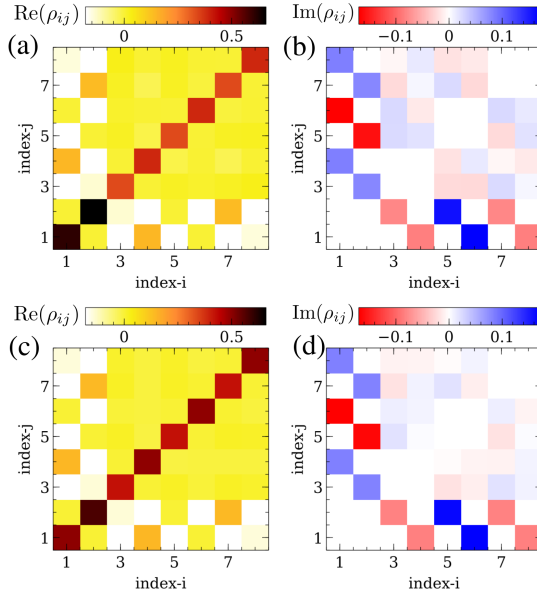


FIGURE D.5: Real and imaginary parts of the density matrix for a trivial  $\mathcal{C} = 0$  (a,b) and a topological  $\mathcal{C} = 2$  (c,d) two dimensional system. In this case, the neural network will implement an image recognition algorithm, where the input are the two images representing the real and imaginary parts.

the non commensuration of graphene with the substrate creates Moire patterns, resulting in an effective spatial modulation of the different contributions.<sup>179–181</sup>

It is worth mentioning two important differences with respect to the model presented in Sec. D.3.1. On one hand, now the Hamiltonian involves the three Pauli matrices, so in general it will be complex. This implies that the calculated density matrices will also be complex, so that the neural network will receive as input both the real and imaginary components. On the other hand, since we are dealing now with a two dimensional system, a finite island will have  $L^2$  sites, with  $L$  the typical size of the island. In particular, the calculation of a the density matrix with the wavefunctions of an island with side  $L \approx 300$  would require the diagonalization of matrix of dimension  $L^2 \approx 90000$ , whose computational complexity is  $L^6$ . It is in this situation where the KPM will be specially useful, as it allows us to calculate the density matrix with a computational complexity of the number of sites,  $L^2$ .

We now move to apply our methodology to the system defined by eq. eq. D.15 . First, to train the neural network, we generate different spatially uniform Hamiltonians by choosing randomly each of the coupling parameters. The Zeeman and Rashba were randomly generated in the interval  $t_R \in [-0.4t, 0.4t]$  and the mass between  $m \in [0, 0.4t]$ . Again, random Anderson-like disorder comparable

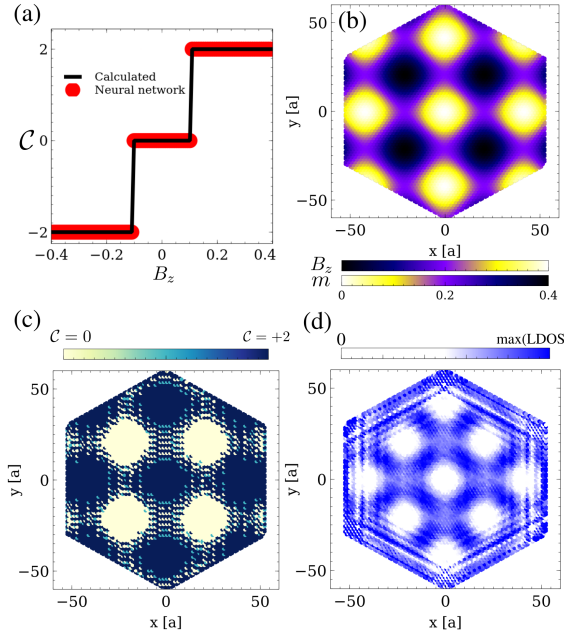


FIGURE D.6: (a) Comparison between the exact Chern number (black) and the prediction of the trained neural network (red) using as input the local density matrix. Once the accuracy of the network has been checked, we created a big graphene island with modulated mass and exchange term as shown in (b). The neural network is used to evaluate the topological invariant in each atom, yielding the result shown in (c). The boundary between different topological phases is expected to give rise to in-gap states, which is confirmed by calculating the in-gap spectral function as shown in (d).

to the other interactions are introduced all across the system  $W_i \in [0.0, 0.4t]$ . The training dataset consisted in 564 samples. For every set of parameters, we built the Hamiltonian as in eq. [eq. D.15](#) and calculated the local density matrix for the central atom and its three first neighbors which are used as input of the network, in this case a 128-dimensional array. Again we chose having two hidden layers with 101 and 21 neurons. It is worth considering again the challenging task of distinguishing between different inputs as those shown in Fig. [D.5](#), which highlights that the classification of topological and trivial phases based only in local properties is far from being a trivial task.

The output for each input was obtained by calculating the Chern number of the ground state of the system integrating the Berry curvature in the Brillouin zone of a translational invariant ( $W_i = 0$ ) Hamiltonian with the same parameters. Once the network was trained, we tested its accuracy on a validation dataset with 586 samples randomly generated, showing an accuracy of  $\sim 92\%$ .

The comparison of the result predicted by the network and the one calculated exactly in a system with translational invariance is shown in Fig. D.6 (a) for the different topological phases.

After the training, we generated a graphene nano-island with 7400 atoms. In this island, we choose a spatially modulated exchange field of the form  $B_z(x, y) = 0.1t[\cos(0.15x) + \cos(0.15y) + 2]$ , a modulated mass term of the form  $m(x, y) = 0.1t[\sin(0.15x) + \sin(0.15y) + 2]$  (shown in Fig. D.6 (b)), and a constant Rashba coupling  $\lambda_R = 0.2$ . The previous modulations are expected to create neighboring trivial and topological areas depending on which is the dominant contribution, mass or exchange and Rashba couplings. With such a Hamiltonian, we calculated the local density matrix using the Kernel polynomial method, that was used as input of the neural network. The result of the evaluation of the neural network across the sample is shown in Fig. D.6 (c). It can be seen that different regions with different Chern number appear according to the spatial modulation of the Hamiltonian parameters. The significance of the different regions becomes clear once the in-gap density of states is calculated in Fig. D.6 (d). This shows both in-gap modes precisely at the boundary between different regions, as expected from the bulk-boundary correspondence, as well as edge states all around the sample.

This result highlights that the artificial neural network faithfully distinguishes between the different phases based solely in local information, providing an useful method to calculate the topological invariant in systems without translational symmetry.

#### D.4 CONCLUSIONS

We have shown that an artificial neural network is capable of predicting the topological nature of different model Hamiltonians using as an input a local sector of the density matrix, *i.e.*, evaluating solely *local properties*. Our procedure consisted on training an artificial neural network using as input the subspace of the density matrix corresponding to a local area of the sample, and as output the topological invariant that an analogous (pristine and translational invariant) Hamiltonian with the same effective parameters would have.

We applied this procedure to two well known models, a 1D topological superconductor and 2D topological insulator. In both cases we considered finite systems with a space dependent Hamiltonian that create regions with both topological and trivial character. By evaluating the network with local quantities for each Hamiltonian we showed that the different topological domains are accurately identified by the network, even when the inhomogeneous systems

have Anderson-like disorder, proving that this methodology can be applied for disordered systems.

It is worth remarking that the training procedure is carried out for a specific model, and tested in that same model for different parameters, including local modulations in space. An open question is whether this methodology can be extended to cases with the same topological classes but different geometries. Finally, it is interesting to note that an analogous methodology could be applied to interacting systems, so that similar procedures could be exploited to identify quantum spin liquid states in two dimensional spin systems.

# About the units

E

---

## E.1 MAGNETIC MOMENT

The magnetic moment of any particle is defined as follows:

$$\vec{m} = g \frac{q}{2m} \vec{S} \quad \text{with} \quad \vec{S} = \frac{\hbar}{2} \vec{\sigma} \quad \Rightarrow \quad \vec{m} = \frac{1}{2} g \mu \vec{\sigma} \quad (\text{E.1})$$

where  $q$  and  $m$  are the charge and mass of particle respectively,  $g$  is the so-called g-factor<sup>I</sup>, a dimensionless constant and  $\vec{\sigma}$  are the Pauli matrices.

$$\sigma_x = \begin{pmatrix} 0 & 1 \\ 1 & 0 \end{pmatrix} \quad ; \quad \sigma_y = \begin{pmatrix} 0 & -i \\ i & 0 \end{pmatrix} \quad ; \quad \sigma_z = \begin{pmatrix} 1 & 0 \\ 0 & -1 \end{pmatrix} \quad (\text{E.2})$$

Note that in eq. E.1 we have grouped the charge/mass ratio in the magneton  $\mu$ .

$$\mu = \frac{q\hbar}{2m} \quad (\text{E.3})$$

In the case of the the magnetic moment of the electron  $\mu$  is the Bohr magneton.

Magnetic moments have units of  $[\vec{m}] = \text{eV/T}$ . This can be seen starting from the right most equation of eq. E.1

$$[\vec{m}] = [\mu] = \frac{\text{C} \cdot \text{eV} \cdot \text{s}}{\text{kg}} = \frac{\text{eV}}{\text{T}}$$

## E.2 EXCHANGE COUPLING

The Heisenberg Hamiltonian reads:

$$H_{ex} = J_H \vec{S}_1 \vec{S}_2 \quad \text{where the units of } J_H \text{ are} \quad [J_H] = \frac{1}{\text{eV} \cdot \text{s}^2} \quad (\text{E.4})$$

---

I The g-factor for the electron and proton are:  $g_e = -2.0023\dots$  and  $g_p = 5.5857\dots$

To use the Heisenberg coupling in eV as it is often calculated from *Density Functional Theory* (DFT) or from effective Hamiltonians, it is necessary to process the hamiltonian eq. E.4

$$H_{ex} = J_H \vec{S}_1 \cdot \vec{S}_2 = J_H \frac{\hbar}{2} \frac{\hbar}{2} \vec{\sigma}_1 \cdot \vec{\sigma}_2 = J \vec{\sigma}_1 \cdot \vec{\sigma}_2 \quad (\text{E.5})$$

where we have used

$$J = J_H \frac{\hbar}{2} \frac{\hbar}{2} \quad \text{where} \quad [J] = \text{eV} \quad (\text{E.6})$$

### E.3 HYPERFINE COUPLING

In our notation, from eq. 6.2 , the hyperfine term is introduced as:

$$H_{hf} = -\mu_0 \frac{2}{3} \vec{m}_e \vec{m}_p \delta(\vec{R}) = \mathcal{A} \vec{\sigma}_e \cdot \vec{\sigma}_p \quad (\text{E.7})$$

Note that, using this notation, the hyperfine coupling has units of energy  $[\mathcal{A}] = \text{eV}$ . This can be easily shown by taking into account these relations

$$\text{Tesla} \rightarrow \text{T} \sim \frac{\text{N}}{\text{A} \cdot \text{m}} \sim \frac{\text{V} \cdot \text{s}}{\text{m}^2} \sim \frac{\text{kg}}{\text{C} \cdot \text{s}} \quad ; \quad \text{Volt} \rightarrow \text{V} \sim \frac{\text{eV}}{\text{C}} \quad ; \quad \text{Ampere} \rightarrow \text{A} \sim \frac{\text{C}}{\text{s}} \quad (\text{E.8})$$

The units, then, for the hyperfine coupling  $\mathcal{A}$  are:

$$[\mathcal{A}] = [\mu_0 \mu_e \mu_p \delta] = \frac{\text{N}}{\text{A}^2} \frac{\text{eV}}{\frac{\text{N}}{\text{A}}} \frac{\text{eV}}{\text{T}} \frac{1}{\text{m}^3} \sim \frac{1}{\text{A}} \frac{\text{eV}^2}{\text{T}} \frac{1}{\text{m}^2} \sim \frac{\text{s}}{\text{C}} \frac{\text{eV}^2}{\text{T}} \frac{1}{\text{m}^2} \sim \frac{\text{V} \cdot \text{s}}{\text{m}^2} \frac{\text{eV}}{\text{T}} \sim \text{eV} \quad (\text{E.9})$$

It is common practice to express the hyperfine coupling in MHz. To convert frequencies to energies we will use the well known value of the  $21\text{cm}^{-1} = 1420 \text{ MHz}$  of Hydrogen<sup>235</sup> and the Planck-Einstein relation  $E = h\nu$ :

$$\nu_H = 1420 \text{ MHz} \Rightarrow \mathcal{A} = 1420 \text{ MHz} \hbar 2\pi \simeq 5.8 \text{ } \mu\text{eV} \quad (\text{E.10})$$

### E.4 ELECTRIC FIELD HAMILTONIAN

The energy of an electron in a constant electric field can be written as<sup>20</sup>

$$H_e = q_e \vec{d} \cdot \vec{E} \quad ; \quad E = \frac{Q}{4\pi\varepsilon} \quad ; \quad \varepsilon = \varepsilon_r \varepsilon_0 \quad (\text{E.11})$$

where  $q_e$  is the charge of the electron,  $\vec{d}$  is the position in the electric field and  $\vec{E}$  is the electric field. The constant  $\varepsilon_0 = 8.85 \cdot 10^{-4} \frac{\text{C}}{\text{V} \cdot \text{m}}$  is the vacuum permittivity and  $\varepsilon_r$  is a dimensionless constant related to the electronic screening of the material as discussed elsewhere in the standard literature<sup>20, 236</sup>

# A complete list of my publications

---

F

- Coupling of the As  $A_{1g}$  phonon to magnetism in iron pnictides<sup>157</sup>
- Interaction-driven phases in the half-filled spinless honeycomb lattice from exact diagonalization<sup>158</sup>
- Quantum spin Hall phase in multilayer graphene<sup>87</sup>
- Edge states in graphene-like systems<sup>86</sup>
- Anomalous magnetism in hydrogenated graphene<sup>29</sup>
- Real-space mapping of topological invariants using artificial neural networks<sup>156</sup>
- Electrical spin manipulation in graphene nanostructures<sup>150</sup>
- Van der Waals spin valves<sup>85</sup>
- Exchange rules for diradical  $\pi$ -Conjugated Hydrocarbons<sup>149</sup>
- Designer fermion models in functionalized graphene bilayers<sup>159</sup>

# Bibliography

---

- [1] B. E. Kane, “A silicon-based nuclear spin quantum computer,” *Nature*, vol. 393, pp. 27–40, 1988.
- [2] G. Feher, “Electron spin resonance experiments on donors in silicon. i. electronic structure of donors by the electron nuclear double resonance technique,” *Phys. Rev.*, vol. 114, pp. 1219–1244, 1959.
- [3] D. K. Wilson and G. Feher, “Electron spin resonance experiments on donors in silicon. iii. investigation of excited states by the application of uniaxial stress and their importance in relaxation processes,” *Phys. Rev.*, vol. 124, pp. 1068–1083, 1961.
- [4] J. S. Waugh and C. P. Slichter, “Mechanism of nuclear spin-lattice relaxation in insulators at very low temperatures,” *Phys. Rev. B*, vol. 37, pp. 4337–4339, 1988.
- [5] C. P. Slichter, *Principles of Magnetic Resonance*. Springer Berlin Heidelberg, 1990.
- [6] B. E. Kane, L. N. Pfeiffer, and K. W. West, “Evidence for an electric-field-induced phase transition in a spin-polarized two-dimensional electron gas,” *Phys. Rev. B*, vol. 46, pp. 7264–7267, Sep 1992.
- [7] K. R. Wald, L. P. Kouwenhoven, P. L. McEuen, N. C. van der Vaart, and C. T. Foxon, “Local dynamic nuclear polarization using quantum point contacts,” *Phys. Rev. Lett.*, vol. 73, pp. 1011–1014, Aug 1994.
- [8] B. Stich, S. Greulich-Weber, and J.-M. Spaeth, “Electrical detection of electron nuclear double resonance in silicon,” *Applied Physics Letters*, vol. 68, no. 8, pp. 1102–1104, 1996.

- [9] D. C. Dixon, K. R. Wald, P. L. McEuen, and M. R. Melloch, “Dynamic nuclear polarization at the edge of a two-dimensional electron gas,” *Phys. Rev. B*, vol. 56, pp. 4743–4750, 1997.
- [10] M. Dobers, K. v. Klitzing, J. Schneider, G. Weimann, and K. Ploog, “Electrical detection of nuclear magnetic resonance in  $gaas - al_xga_{1-x}as$  heterostructures,” *Phys. Rev. Lett.*, vol. 61, pp. 1650–1653, Oct 1988.
- [11] A. R. Stegner, C. Boehme, H. Huebl, M. Stutzmann, K. Lips, and M. S. Brandt, “Electrical detection of coherent 31p spin quantum states,” *Nature Physics*, vol. 2, pp. 835–838, nov 2006.
- [12] A. Morello, J. J. Pla, F. a. Zwanenburg, K. W. Chan, K. Y. Tan, H. Huebl, M. Möttönen, C. D. Nugroho, C. Yang, J. a. van Donkelaar, A. D. C. Alves, D. N. Jamieson, C. C. Escott, L. C. L. Hollenberg, R. G. Clark, and A. S. Dzurak, “Single-shot readout of an electron spin in silicon,” *Nature*, vol. 467, no. 7316, pp. 687–91, 2010.
- [13] J. J. Pla, K. Y. Tan, J. P. Dehollain, W. H. Lim, J. J. L. Morton, F. A. Zwanenburg, D. N. Jamieson, A. S. Dzurak, and A. Morello, “High-fidelity readout and control of a nuclear spin qubit in silicon,” *Nature*, vol. 496, 2012.
- [14] J. P. Dehollain, J. T. Muhonen, K. Y. Tan, A. Saraiva, D. N. Jamieson, A. S. Dzurak, and A. Morello, “Single-shot readout and relaxation of singlet and triplet states in exchange-coupled p 31 electron spins in silicon,” *Physical Review Letters*, vol. 112, no. 23, pp. 1–6, 2014.
- [15] E. McCann, “Asymmetry gap in the electronic band structure of bilayer graphene,” *Phys. Rev. B*, vol. 74, p. 161403, Oct 2006.
- [16] E. V. Castro, K. S. Novoselov, S. V. Morozov, N. M. R. Peres, J. M. B. Lopes dos Santos, J. Nilsson, F. Guinea, A. K. Geim, and A. H. Castro Neto, “Biased bilayer graphene: Semiconductor with a gap tunable by the electric field effect,” *Phys. Rev. Lett.*, vol. 99, no. 21, p. 216802, 2007.
- [17] J. B. Oostinga, H. B. Heersche, X. Liu, A. F. Morpurgo, and L. M. K. Vandersypen, “Gate-induced insulating state in bilayer graphene devices,” *Nature Materials*, vol. 7, pp. 151–157, feb 2007.
- [18] Y. Zhang, T.-T. Tang, C. Girit, Z. Hao, M. C. Martin, A. Zettl, M. F. Crommie, Y. R. Shen, and F. Wang, “Direct observation of a widely tunable bandgap in bilayer graphene,” *Nature*, vol. 459, no. 7248, 2009.

- [19] T. Taychatanapat and P. Jarillo-Herrero, “Electronic transport in dual-gated bilayer graphene at large displacement fields,” *Phys. Rev. Lett.*, vol. 105, p. 166601, oct 2010.
- [20] E. V. Castro, K. S. Novoselov, S. V. Morozov, N. M. R. Peres, J. M. B. Lopes dos Santos, J. Nilsson, F. Guinea, a. K. Geim, and a. H. Castro Neto, “Electronic properties of a biased graphene bilayer,” *J. Phys. Condens. Matter*, vol. 22, no. 17, p. 175503, 2010.
- [21] L. A. Ponomarenko, A. K. Geim, A. A. Zhukov, R. Jalil, S. V. Morozov, K. S. Novoselov, I. V. Grigorieva, E. H. Hill, V. Cheianov, V. Falko, K. Watanabe, T. Taniguchi, and R. V. Gorbachev, “Tunable metal-insulator transition in double-layer graphene heterostructures,” *Nature Physics*, vol. 7, no. 12, pp. 958–961, 2011.
- [22] M. T. Allen, J. Martin, and A. Yacoby, “Gate-defined quantum confinement in suspended bilayer graphene,” *Nature Communications*, vol. 3, no. May, p. 934, 2012.
- [23] M. Sui, G. Chen, L. Ma, W.-Y. Shan, D. Tian, K. Watanabe, T. Taniguchi, X. Jin, W. Yao, D. Xiao, and Y. Zhang, “Gate-tunable topological valley transport in bilayer graphene,” *Nature Physics*, no. September, pp. 1–6, 2015.
- [24] D. C. Elias, R. R. Nair, T. M. G. Mohiuddin, S. V. Morozov, P. Blake, M. P. Halsall, A. C. Ferrari, D. W. Boukhvalov, M. I. Katsnelson, A. K. Geim, and K. S. Novoselov, “Control of graphene’s properties by reversible hydrogenation: Evidence for graphane,” *Science*, vol. 323, no. 5914, pp. 610–613, 2009.
- [25] H. Gonzalez-Herrero, J. M. Gomez-Rodriguez, P. Mallet, M. Moaied, J. J. Palacios, C. Salgado, M. M. Ugeda, J.-Y. Veuillen, F. Yndurain, and I. Brihuega, “Atomic-scale control of graphene magnetism by using hydrogen atoms,” *Science*, vol. 352, no. 6284, pp. 437–441, 2016.
- [26] I. Brihuega and F. Yndurain, “Selective hydrogen adsorption in graphene rotated bilayers,” *J. Phys. Chem. B*, vol. 112, no. 2, pp. 595–600, 2017.
- [27] Y. Cao, V. Fatemi, A. Demir, S. Fang, S. L. Tomarken, J. Y. Luo, J. D. Sanchez-Yamagishi, K. Watanabe, T. Taniguchi, E. Kaxiras, R. C. Ashoori, and P. Jarillo-Herrero, “Correlated insulator behaviour at half-filling in magic angle graphene superlattices,” *Nature*, vol. 556, p. 80, 2018.

- [28] Y. Cao, V. Fatemi, S. Fang, K. Watanabe, T. Taniguchi, E. Kaxiras, and P. Jarillo-Herrero, “Unconventional superconductivity in magic-angle graphene superlattices,” *Nature*, pp. 1–17, 2018.
- [29] N. A. García-Martínez, J. L. Lado, D. Jacob, and J. Fernández-Rossier, “Anomalous magnetism in hydrogenated graphene,” *Phys. Rev. B*, vol. 96, p. 024403, 2017.
- [30] M. I. Katsnelson, *Graphene: Carbon in Two Dimensions*. Cambridge University Press, 2012.
- [31] A. K. Geim and K. S. Novoselov, “Rise of graphene,” *Nat. Mater.*, vol. 6, pp. 183–191, 2007.
- [32] S. Murakami, “Quantum spin hall phases,” *Progress of Theoretical Physics Supplement*, vol. 176, pp. 279–301, 2008.
- [33] A. H. Castro Neto, F. Guinea, N. M. R. Peres, K. S. Novoselov, and A. K. Geim, “The electronic properties of graphene,” *Reviews of Modern Physics*, vol. 81, no. 1, pp. 109–162, 2009.
- [34] R. Mas-Balleste, C. Gomez-Navarro, J. Gomez-Herrero, F. Zamora, R. Mas-Ballesté, C. Gómez-Navarro, and J. Gómez-Herrero, “2d materials: to graphene and beyond,” *Nanoscale*, vol. 3, pp. 20–30, jan 2011.
- [35] S. Konschuh, M. Gmitra, D. Kochan, and J. Fabian, “Theory of spin-orbit coupling in bilayer graphene,” *Physical Review B*, vol. 85, p. 16, nov 2011.
- [36] D. R. Cooper, B. D’Anjou, N. Ghattamaneni, B. Harack, M. Hilke, A. Horth, N. Majlis, M. Massicotte, L. Vandsburger, E. Whiteway, and V. Yu, “Experimental review of graphene,” *ISRN Condensed Matter Physics*, vol. 2012, p. 56, 2012.
- [37] W. Han, R. K. Kawakami, M. Gmitra, and J. Fabian, “Graphene spintronics,” *Nature nanotechnology*, vol. 9, no. 10, pp. 794–807, 2014.
- [38] E. Sadurní, E. Rivera-Mociños, and A. Rosado, “Discrete symmetry in graphene: the dirac equation and beyond,” *arXiv preprint arXiv:1411.6319*, no. 1, pp. 1–12, 2014.
- [39] A. V. Rozhkov, A. O. Sboychakov, A. L. Rakhmanov, and F. Nori, “Electronic properties of graphene-based bilayer systems,” *Physics Reports*, vol. 648, pp. 1–104, 2016.

- [40] K. S. Novoselov, A. K. Geim, S. V. Morozov, D. Jiang, Y. Zhang, S. V. Dubonos, I. V. Grigorieva, and A. A. Firsov, "Electric field effect in atomically thin carbon films," *Science*, vol. 306, no. 5696, pp. 666–669, 2004.
- [41] K. S. Novoselov, A. K. Geim, S. V. Morozov, D. Jiang, M. I. Katsnelson, I. V. Grigorieva, S. V. Dubonos, and A. A. Firsov, "Two-dimensional gas of massless dirac fermions in graphene," *Nature*, vol. 438, no. 7065, pp. 197–200, 2005.
- [42] P. R. Wallace, "The band theory of graphite," *Phys. Rev.*, vol. 71, pp. 622–634, May 1947.
- [43] A. J. Van Bommel, J. E. Crombeen, and A. Van Tooren, "Leed and auger electron observations of the sic(0001) surface," *Surface Science*, vol. 48, no. 2, pp. 463–472, 1975.
- [44] G. W. Semenoff, "Condensed matter simulation of a three-dimensional anomaly," *Physical Review Letters*, vol. 53, no. 26, pp. 2449–2452, 1984.
- [45] F. D. M. Haldane, "Model for a quantum hall effect without landau levels: Condensed-matter realization of the "parity anomaly"," *Physical Review Letters*, vol. 61, no. 18, pp. 2015–2018, 1988.
- [46] I. Forbeaux, J. Themlin, and J. Debever, "Heteroepitaxial graphite on interface formation through conduction-band electronic structure," *Phys. Rev. B*, vol. 58, no. 24, pp. 16396–16406, 1998.
- [47] C. Oshima, A. Itoh, E. Rokuta, T. Tanaka, K. Yamashita, and T. Sakurai, "A hetero-epitaxial-double-atomic-layer system of monolayer graphene/monolayer h.bn on ni(111)," *Solid State Communications*, vol. 116, no. 1, pp. 37–40, 2000.
- [48] P. Y. Huang, C. S. Ruiz-Vargas, A. M. Van Der Zande, W. S. Whitney, M. P. Levendorf, J. W. Kevek, S. Garg, J. S. Alden, C. J. Hustedt, Y. Zhu, J. Park, P. L. McEuen, and D. A. Muller, "Grains and grain boundaries in single-layer graphene atomic patchwork quilts," *Nature*, vol. 469, no. 7330, pp. 389–392, 2011.
- [49] Y. Zheng and T. Ando, "Hall conductivity of a two-dimensional graphite system," *Phys. Rev. B*, vol. 65, p. 245420, Jun 2002.
- [50] Y. Zhang, Y.-W. Tan, H. L. Stormer, and P. Kim, "Experimental observation of the quantum hall effect and berry's phase in graphene," *Nature*, vol. 438, pp. 201–4, nov 2005.

- [51] V. P. Gusynin and S. G. Sharapov, “Unconventional integer quantum hall effect in graphene,” *Phys. Rev. Lett.*, vol. 95, p. 146801, Sep 2005.
- [52] N. Peres, F. Guinea, and C. N. C. N. A.H., “Electronic properties of two-dimensional carbon,” *Annals of Physics*, vol. 321, no. 7, pp. 1559 – 1567, 2006. July 2006 Special Issue.
- [53] L. Brey and H. Fertig, “Edge states and the quantized hall effect in graphene,” *Physical Review B*, vol. 73, no. 19, p. 195408, 2006.
- [54] H. a. Fertig and L. Brey, “Edges and interactions for graphene in quantum hall states,” *Solid State Communications*, vol. 143, pp. 86–91, 2007.
- [55] P. M. Ostrovsky, I. V. Gornyi, and A. D. Mirlin, “Theory of anomalous quantum hall effects in graphene,” *Phys. Rev. B*, vol. 77, no. 19, p. 195430, 2008.
- [56] S. Fujita and A. Suzuki, “Theory of the half-integer quantum hall effect in graphene,” *Int. J. Theor. Phys.*, vol. 55, no. 11, pp. 4830–4840, 2016.
- [57] J. Sichau, M. Prada, T. Anlauf, T. J. Lyon, B. Bosnjak, L. Tiemann, and R. H. Blick, “Resonance microwave measurements of an intrinsic spin-orbit coupling gap in graphene: A possible indication of a topological state,” *Phys. Rev. Lett.*, vol. 122, p. 046403, Feb 2019.
- [58] M. Z. Hasan and C. L. Kane, “Colloquium: Topological insulators,” *Rev. Mod. Phys.*, vol. 82, pp. 3045–3067, nov 2010.
- [59] M. Ishigami, J. H. Chen, W. G. Cullen, M. S. Fuhrer, and E. D. Williams, “Atomic structure of graphene on *sio<sub>2</sub>*,” *Nano Letters*, vol. 7, no. 6, pp. 1643–1648, 2007.
- [60] N. W. Ashcroft and N. Mermin, *Solid State Physics*. Harcourt College Publishers, 1976.
- [61] J. C. Slater and G. F. Koster, “Simplified lcao method for the periodic potential problem,” *Phys. Rev.*, vol. 94, pp. 1498–1524, Jun 1954.
- [62] G. Grosso and G. Parravicini, *Solid State Physics*. Elsevier Science, 2000.
- [63] W. A. Harrison, *Elementary Electronic Structure (Revised Edition)*. WSPC, 1930.
- [64] D. Gosálbez-Martínez, J. J. Palacios, and J. Fernández-Rossier, “Spin-orbit interaction in curved graphene ribbons,” *Physical Review B*, vol. 83, no. 11, p. 115436, 2011.

- [65] S. Konschuh, M. Gmitra, and J. Fabian, “Tight-binding theory of the spin-orbit coupling in graphene,” *Physical Review B*, vol. 82, p. 245412, dec 2010.
- [66] R. Saito, G. Dresselhaus, and M. S. Dresselhaus, *Physical Properties of Carbon Nanotubes*. Imperial College Press, London, jul 1998.
- [67] Y. Liu and R. E. Allen, “Electronic structure of the semimetals bi and sb,” *Phys. Rev. B*, vol. 52, no. 3, pp. 1566–1577, 1995.
- [68] C. L. Kane and E. J. Mele, “Quantum spin hall effect in graphene,” *Physical Review Letters*, vol. 95, no. 22, 2005.
- [69] C. L. Kane and E. J. Mele, “ $z_2$  topological order and the quantum spin hall effect,” *Physical Review Letters*, vol. 95, p. 146802, sep 2005.
- [70] H. Min, J. E. Hill, N. A. Sinitsyn, B. R. Sahu, L. Kleinman, and A. H. MacDonald, “Intrinsic and rashba spin-orbit interactions in graphene sheets,” *Physical Review B*, vol. 74, p. 165310, oct 2006.
- [71] W. Norimatsu and M. Kusunoki, “Selective formation of abc-stacked graphene layers on sic(0001),” *Physical Review B*, vol. 81, p. 161410, apr 2010.
- [72] J. C. Charlier, X. Gonze, and J. Michenaud, “First-principles study of the stacking effect on the electronic properties of graphite(s),” *Carbon*, vol. 32, no. 2, pp. 289–299, 1994.
- [73] J. C. Charlier, X. Gonze, and J. P. Michenaud, “Graphite interplanar bonding: electronic delocalization and van der waals interaction,” *Euro-physics Letters*, vol. 28, no. 6, pp. 403–408, 1994.
- [74] I. Martin, Y. M. Blanter, and A. F. Morpurgo, “Topological confinement in bilayer graphene,” *Phys. Rev. Lett.*, vol. 100, p. 036804, Jan 2008.
- [75] P. San-Jose, E. Prada, E. McCann, and H. Schomerus, “Pseudospin valve in bilayer graphene: Towards graphene-based pseudospintrronics,” *Phys. Rev. Lett.*, vol. 102, p. 247204, Jun 2009.
- [76] R. N. Wang, G. Y. Dong, S. F. Wang, G. S. Fu, and J. L. Wang, “Intra- and inter-layer charge redistribution in biased bilayer graphene,” *AIP Advances*, vol. 6, no. 3, p. 035213, 2016.

- [77] E. Prada, P. San-Jose, L. Brey, and H. Fertig, “Band topology and the quantum spin hall effect in bilayer graphene,” *Solid State Communications*, vol. 151, pp. 1075–1083, aug 2011.
- [78] J. Jung, F. Zhang, Z. Qiao, and A. H. MacDonald, “Valley-hall kink and edge states in multilayer graphene,” *Phys. Rev. B - Condens. Matter Mater. Phys.*, vol. 84, no. 7, pp. 1–5, 2011.
- [79] L. J. Yin, H. Jiang, J. B. Qiao, and L. He, “Direct imaging of topological edge states at a bilayer graphene domain wall,” *Nat. Commun.*, vol. 7, p. 11760, 2016.
- [80] J. Li, K. Wang, K. J. McFaul, Z. Zern, Y. Ren, K. Watanabe, T. Taniguchi, Z. Qiao, and J. Zhu, “Gate-controlled topological conducting channels in bilayer graphene,” *Nat. Nanotechnol.*, vol. 11, pp. 1060–1065, 2016.
- [81] J. Li, R. X. Zhang, Z. Yin, J. Zhang, K. Watanabe, T. Taniguchi, C. Liu, and J. Zhu, “A valley valve and electron beam splitter,” *Science*, vol. 362, no. 6419, pp. 1149–1152, 2018.
- [82] D. R. Klein, D. MacNeill, J. L. Lado, D. Soriano, E. Navarro-Moratalla, K. Watanabe, T. Taniguchi, S. Manni, P. Canfield, J. Fernández-Rossier, and P. Jarillo-Herrero, “Probing magnetism in 2d van der waals crystalline insulators via electron tunneling,” *Science*, 2018.
- [83] T. Song, X. Cai, M. W.-Y. Tu, X. Zhang, B. Huang, N. P. Wilson, K. L. Seyler, L. Zhu, T. Taniguchi, K. Watanabe, M. A. McGuire, D. H. Cobden, D. Xiao, W. Yao, and X. Xu, “Giant tunneling magnetoresistance in spin-filter van der waals heterostructures,” *Science*, 2018.
- [84] Z. Wang, I. Gutiérrez-Lezama, N. Ubrig, M. Kroner, M. Gibertini, T. Taniguchi, K. Watanabe, A. Imamoğlu, E. Giannini, and A. F. Morpurgo, “Very large tunneling magnetoresistance in layered magnetic semiconductor  $cri_3$ ,” *Nat. Commun.*, vol. 9, jun 2018.
- [85] C. Cardoso, D. Soriano, N. A. García-Martínez, and J. Fernández-Rossier, “Van der waals spin valves,” *Phys. Rev. Lett.*, vol. 121, no. 6, p. 67701, 2018.
- [86] J. Lado, N. García-Martínez, and J. Fernández-Rossier, “Edge states in graphene-like systems,” *Synthetic Metals*, vol. 210, pp. 56–67, 2015.

- [87] N. A. García-Martínez, J. L. Lado, and J. Fernández-Rossier, “Quantum spin hall phase in multilayer graphene,” *Physical Review B*, vol. 91, p. 235451, jun 2015.
- [88] P. W. Anderson, “Localized magnetic states in metals,” *Phys. Rev.*, vol. 124, pp. 41–53, Oct 1961.
- [89] M. D. Daybell and W. A. Steyert, “Localized magnetic impurity states in metals: Some experimental relationships,” *Rev. Mod. Phys.*, vol. 40, pp. 380–389, Apr 1968.
- [90] C. P. Slichter, “Spin resonance of impurity atoms in silicon,” *Phys. Rev.*, vol. 99, pp. 479–480, Jul 1955.
- [91] E. J. Duplock, M. Scheffler, and P. J. D. Lindan, “Hallmark of perfect graphene,” *Phys. Rev. Lett.*, vol. 92, p. 225502, Jun 2004.
- [92] O. V. Yazyev and L. Helm, “Defect-induced magnetism in graphene,” *Phys. Rev. B*, vol. 75, p. 125408, Mar 2007.
- [93] D. W. Boukhvalov, M. I. Katsnelson, and A. I. Lichtenstein, “Hydrogen on graphene: Electronic structure, total energy, structural distortions and magnetism from first-principles calculations,” *Phys. Rev. B*, vol. 77, p. 035427, Jan 2008.
- [94] J. Palacios, J. Fernández-Rossier, and L. Brey, “Vacancy-induced magnetism in graphene and graphene ribbons,” *Physical Review B*, vol. 77, p. 195428, may 2008.
- [95] O. V. Yazyev, “Emergence of magnetism in graphene materials and nanostructures,” *Reports on progress in physics*, vol. 73, p. 056501, may 2010.
- [96] E. J. G. Santos, A. Ayuela, and D. Sánchez-Portal, “Universal magnetic properties of  $sp^3$ -type defects in covalently functionalized graphene,” *New Journal of Physics*, vol. 14, 2012.
- [97] D. Soriano, F. Muñoz-Rojas, J. Fernández-Rossier, and J. J. Palacios, “Hydrogenated graphene nanoribbons for spintronics,” *Physical Review B*, vol. 81, no. 16, p. 165409, 2010.
- [98] N. Leconte, D. Soriano, S. Roche, P. Ordejon, J.-C. Charlier, and J. J. Palacios, “Magnetism-dependent transport phenomena in hydrogenated graphene: From spin-splitting to localization effects,” *ACS Nano*, vol. 5, pp. 3987–3992, may 2011.

- [99] D. Soriano, N. Leconte, P. Ordejón, J.-C. Charlier, J.-J. Palacios, and S. Roche, “Magnetoresistance and magnetic ordering fingerprints in hydrogenated graphene,” *Phys. Rev. Lett.*, vol. 107, p. 016602, Jun 2011.
- [100] W. Han, R. K. Kawakami, M. Gmitra, and J. Fabian, “Graphene spintronics,” *Nature nanotechnology*, vol. 9, no. 10, pp. 794–807, 2014.
- [101] J. O. Sofo, A. S. Chaudhari, and G. D. Barber, “Graphane: A two-dimensional hydrocarbon,” *Phys. Rev. B*, vol. 75, p. 153401, Apr 2007.
- [102] V. M. Pereira, F. Guinea, J. M. B. Lopes dos Santos, N. M. R. Peres, and A. H. Castro Neto, “Disorder induced localized states in graphene,” *Phys. Rev. Lett.*, vol. 96, p. 036801, Jan 2006.
- [103] H. Kumazaki and D. S. Hirashima, “Possible vacancy-induced magnetism on a half-filled honeycomb lattice,” *Journal of the Physical Society of Japan*, vol. 76, no. 3, p. 034707, 2007.
- [104] T. O. Wehling, A. V. Balatsky, M. I. Katsnelson, A. I. Lichtenstein, K. Scharnberg, and R. Wiesendanger, “Local electronic signatures of impurity states in graphene,” *Phys. Rev. B*, vol. 75, p. 125425, Mar 2007.
- [105] V. M. Pereira, J. M. B. Lopes Dos Santos, and A. H. Castro Neto, “Modeling disorder in graphene,” *Physical Review B*, vol. 77, no. 11, 2008.
- [106] A. H. Castro Neto and F. Guinea, “Impurity-induced spin-orbit coupling in graphene,” *Phys. Rev. Lett.*, vol. 103, p. 026804, Jul 2009.
- [107] M. Gmitra, D. Kochan, and J. Fabian, “Spin-orbit coupling in hydrogenated graphene,” *Physical Review Letters*, vol. 110, no. 24, p. 246602, 2013.
- [108] J. Balakrishnan, G. Kok Wai Koon, M. Jaiswal, A. H. Castro Neto, and B. Özyilmaz, “Colossal enhancement of spin–orbit coupling in weakly hydrogenated graphene,” *Nature Physics*, vol. 9, no. 5, pp. 284–287, 2013.
- [109] M. Wojtaszek, I. J. Vera-Marun, T. Maassen, and B. J. van Wees, “Enhancement of spin relaxation time in hydrogenated graphene spin-valve devices,” *Phys. Rev. B*, vol. 87, p. 081402, Feb 2013.
- [110] D. Kochan, M. Gmitra, and J. Fabian, “Spin relaxation mechanism in graphene: Resonant scattering by magnetic impurities,” *Physical Review Letters*, vol. 112, p. 116602, mar 2014.

- [111] D. Soriano, D. V. Tuan, S. M.-M. Dubois, M. Gmitra, A. W. Cummings, D. Kochan, F. Ortmann, J. C. Charlier, J. Fabian, and S. Roche, “Spin transport in hydrogenated graphene,” *2D Materials*, vol. 2, no. 2, p. 22002, 2015.
- [112] J. W. González and J. Fernández-Rossier, “Impurity states in the quantum spin hall phase in graphene,” *Physical Review B*, vol. 86, no. 11, p. 115327, 2012.
- [113] J. O. Sofo, G. Usaj, P. S. Cornaglia, A. M. Suarez, A. D. Hernández-Nieves, and C. A. Balseiro, “Magnetic structure of hydrogen-induced defects on graphene,” *Phys. Rev. B*, vol. 85, p. 115405, Mar 2012.
- [114] J. Zhou, Q. Wang, Q. Sun, X. Chen, Y. Kawazoe, and P. Jena, “Ferromagnetism in semihydrogenated graphene sheet,” *Nano letters*, vol. 9, no. 11, pp. 3867–3870, 2009.
- [115] D. Jacob and G. Kotliar, “Orbital selective and tunable kondo effect of magnetic adatoms on graphene: Correlated electronic structure calculations,” *Phys. Rev. B*, vol. 82, p. 085423, Aug 2010.
- [116] M. Settnes, S. R. Power, J. Lin, D. H. Petersen, and A.-P. Jauho, “Patched green’s function techniques for two-dimensional systems: Electronic behavior of bubbles and perforations in graphene,” *Physical Review B*, vol. 91, no. 12, p. 125408, 2015.
- [117] J. Lado and J. Fernández-Rossier, “Unconventional yu–shiba–rusinov states in hydrogenated graphene,” *2D Materials*, vol. 3, no. 2, p. 025001, 2016.
- [118] M. I. Katsnelson, *GRAPHENE: Carbon in Two Dimensions*. No. 1, 2012.
- [119] E. N. Economou, *Green’s Functions in Quantum Physics*. 2006.
- [120] F. Muñoz-Rojas, J. Fernández-Rossier, and J. J. Palacios, “Giant magnetoresistance in ultrasmall graphene based devices,” *Phys. Rev. Lett.*, vol. 102, p. 136810, Apr 2009.
- [121] J. Fernández-Rossier and J. Palacios, “Magnetism in graphene nanoislands,” *Physical Review Letters*, vol. 99, no. 17, p. 177204, 2007.
- [122] A. Weiße, G. Wellein, A. Alvermann, and H. Fehske, “The kernel polynomial method,” *Rev. Mod. Phys.*, vol. 78, pp. 275–306, Mar 2006.

- [123] D. Jackson, “On approximation by trigonometric sums and polynomials,” *Transactions of the American Mathematical society*, vol. 13, no. 4, pp. 491–515, 1912.
- [124] R. R. Nair, M. Sepioni, I.-L. Tsai, O. Lehtinen, J. Keinonen, a. V. Krasheninnikov, T. Thomson, a. K. Geim, and I. V. Grigorieva, “Spin-half paramagnetism in graphene induced by point defects,” *Nature Physics*, vol. 8, no. 3, pp. 199–202, 2012.
- [125] R. Nair, I.-L. Tsai, M. Sepioni, O. Lehtinen, J. Keinonen, A. Krasheninnikov, A. Castro Neto, M. Katsnelson, A. Geim, and I. Grigorieva, “Dual origin of defect magnetism in graphene and its reversible switching by molecular doping,” *Nature communications*, vol. 4, 2013.
- [126] P. Haase, S. Fuchs, T. Pruschke, H. Ochoa, and F. Guinea, “Magnetic moments and kondo effect near vacancies and resonant scatterers in graphene,” *Phys. Rev. B*, vol. 83, no. 24, p. 241408, 2011.
- [127] A. K. Mitchell and L. Fritz, “Kondo effect with diverging hybridization: Possible realization in graphene with vacancies,” *Phys. Rev. B*, vol. 88, p. 075104, Aug 2013.
- [128] M. Gmitra, S. Konschuh, C. Ertler, C. Ambrosch-Draxl, and J. Fabian, “Band-structure topologies of graphene: Spin-orbit coupling effects from first principles,” *Physical Review B*, vol. 80, no. 23, p. 235431, 2009.
- [129] E. V. Castro, M. P. López-Sancho, and M. A. H. Vozmediano, “New type of vacancy-induced localized states in multilayer graphene,” *Physical Review Letters*, vol. 104, no. 3, pp. 1–4, 2010.
- [130] C. Lanczos, “An iteration method for the solution of the eigenvalue problem of linear differential and integral operators,” *Journal of Research of the National Bureau of Standards*, vol. 45, p. 255, oct 1950.
- [131] I. U. Ojalvo and M. Newman, “Vibration modes of large structures by an automatic matrix-reduction method,” *AIAA J.*, vol. 8, no. 7, pp. 1234–1239, 1970.
- [132] W. E. Arnoldi, “The principle of minimized iterations in the solution of the matrix eigenvalue problem,” *Quarterly of Applied Mathematics*, vol. 9, pp. 17–29, apr 1951.
- [133] E. Lieb, “Two theorems on the hubbard model,” *Physical Review Letters*, vol. 62, no. 10, pp. 1201–1204, 1989.

- [134] C. Cohen-Tannoudji, B. Diu, and F. Laloë, *Quantum mechanics. Quantum Mechanics*, Wiley, 1977.
- [135] A. Ranjbar, M. S. Bahramy, M. Khazaei, H. Mizuseki, and Y. Kawazoe, “First-principles study of structural stability, magnetism, and hyperfine coupling in hydrogen clusters adsorbed on graphene,” *Physical Review B*, vol. 82, no. 16, p. 165446, 2010.
- [136] R. Kalra, A. Laucht, C. D. Hill, and A. Morello, “Robust two-qubit gates for donors in silicon controlled by hyperfine interactions,” *Physical Review X*, vol. 4, no. 2, p. 021044, 2014.
- [137] E. Cocchi, L. A. Miller, J. H. Drewes, M. Koschorreck, D. Pertot, F. Brennecke, and M. Köhl, “Equation of state of the two-dimensional hubbard model,” *Phys. Rev. Lett.*, vol. 116, p. 175301, Apr 2016.
- [138] P.-A. Mortemousque, E. Chanrion, B. Jadot, H. Flentje, A. Ludwig, A. D. Wieck, M. Urdampilleta, C. Bauerle, and T. Meunier, “Coherent control of individual electron spins in a two dimensional array of quantum dots,” *arXiv preprint arXiv:1808.06180*, 2018.
- [139] J. P. Dehollain, U. Mukhopadhyay, V. P. Michal, Y. Wang, B. Wunsch, C. Reichl, W. Wegscheider, M. S. Rudner, E. Demler, and L. M. Vandersypen, “Nagaoka ferromagnetism observed in a quantum dot plaquette,” *arXiv preprint arXiv:1904.05680*, 2019.
- [140] K. K. Gomes, W. Mar, W. Ko, F. Guinea, and H. C. Manoharan, “Designer dirac fermions and topological phases in molecular graphene,” *Nature*, vol. 483, no. 7389, p. 306, 2012.
- [141] R. Drost, T. Ojanen, A. Harju, and P. Liljeroth, “Topological states in engineered atomic lattices,” *Nature Physics*, vol. 13, no. 7, p. 668, 2017.
- [142] J. Girovsky, J. Lado, F. Kalff, E. Fahrenfort, L. Peters, J. Fernández-Rossier, and A. F. Otte, “Emergence of quasiparticle bloch states in artificial crystals crafted atom-by-atom,” *SciPost Physics*, vol. 2, no. 3, p. 020, 2017.
- [143] A. A. Khajetoorians, D. Wegner, A. F. Otte, and I. Swart, “Designer quantum states of matter created atom-by-atom,” *arXiv preprint arXiv:1904.11680*, 2019.
- [144] F. E. Kalff, M. P. Rebergen, E. Fahrenfort, J. Girovsky, R. Toskovic, J. L. Lado, J. Fernández-Rossier, and A. F. Otte, “A kilobyte rewritable

- atomic memory,” *Nature Nanotechnology*, vol. 11, no. 11, pp. 926–929, 2016.
- [145] M. M. Ugeda, D. Fernández-Torre, I. Brihuega, P. Pou, A. J. Martínez-Galera, R. Pérez, and J. M. Gómez-Rodríguez, “Point defects on graphene on metals,” *Phys. Rev. Lett.*, vol. 107, no. 11, pp. 1–5, 2011.
  - [146] Y. Cao, V. Fatemi, S. Fang, K. Watanabe, T. Taniguchi, E. Kaxiras, and P. Jarillo-Herrero, “Unconventional superconductivity in magic-angle graphene superlattices,” *Nature*, vol. 556, no. 7699, p. 43, 2018.
  - [147] E. McCann and M. Koshino, “The electronic properties of bilayer graphene,” *Reports on progress in physics*, vol. 76, p. 27, 2012.
  - [148] J. Nilsson and A. H. C. Neto, “Impurities in a biased graphene bilayer,” *Physical Review Letters*, vol. 98, no. 12, p. 126801, 2007.
  - [149] R. Ortiz, R. Boto, N. García-Martínez, J. Sancho-García, M. Melle-Franco, and J. Fernández-Rossier, “Exchange rules for diradical  $\pi$ -conjugated hydrocarbons,” *Nano Lett.*, vol. 19, no. 9, 2019.
  - [150] R. Ortiz, N. A. García-Martínez, J. L. Lado, and J. Fernández-Rossier, “Electrical spin manipulation in graphene nanostructures,” *Physical Review B*, vol. 97, no. 19, p. 195425, 2018.
  - [151] S. Sorella and E. Tosatti, “Semi-metal-insulator transition of the hubbard model in the honeycomb lattice,” *EPL (Europhysics Letters)*, vol. 19, no. 8, p. 699, 1992.
  - [152] P. Sahebsara and D. Sénéchal, “Hubbard model on the triangular lattice: Spiral order and spin liquid,” *Phys. Rev. Lett.*, vol. 100, p. 136402, Mar 2008.
  - [153] I. Martin and C. D. Batista, “Itinerant electron-driven chiral magnetic ordering and spontaneous quantum hall effect in triangular lattice models,” *Phys. Rev. Lett.*, vol. 101, p. 156402, Oct 2008.
  - [154] R. Nandkishore, L. Levitov, and A. Chubukov, “Chiral superconductivity from repulsive interactions in doped graphene,” *Nature Physics*, vol. 8, no. 2, p. 158, 2012.
  - [155] P. San-Jose, J. L. Lado, R. Aguado, F. Guinea, and J. Fernández-Rossier, “Majorana zero modes in graphene,” *Physical Review X*, vol. 5, no. 4, p. 041042, 2015.

- [156] D. Carvalho, N. A. García-Martínez, J. L. Lado, and J. Fernández-Rossier, “Real-space mapping of topological invariants using artificial neural networks,” *Physical Review B*, vol. 97, no. 11, p. 115453, 2018.
- [157] N. A. García-Martínez, B. Valenzuela, S. Ciuchi, E. Cappelluti, M. J. Calderon, and E. Bascones, “Coupling of the  $a_{1g}$  phonon to magnetism in iron pnictides,” *Physical Review B*, vol. 88, no. 16, p. 165106, 2013.
- [158] N. A. García-Martínez, A. G. Grushin, T. Neupert, B. Valenzuela, and E. V. Castro, “Interaction-driven phases in the half-filled spinless honeycomb lattice from exact diagonalization,” *Physical Review B*, vol. 88, p. 245123, dec 2013.
- [159] N. A. García-Martínez and J. Fernández-Rossier, “Designer fermion models in functionalized graphene bilayers,” *Phys. Rev. Res.*, vol. 1, no. 3, pp. 1–5, 2019.
- [160] S. Konschuh, M. Gmitra, D. Kochan, and J. Fabian, “Theory of spin-orbit coupling in bilayer graphene,” *Phys. Rev. B*, vol. 85, p. 115423, Mar 2012.
- [161] F. Guinea, “Spin–orbit coupling in a graphene bilayer and in graphite,” *New Journal of Physics*, vol. 12, no. 8, p. 083063, 2010.
- [162] A. Cortijo, A. G. Grushin, and M. A. H. Vozmediano, “Topological insulating phases in monolayer and bilayer graphene: An effective action approach,” *Physical Review B*, vol. 82, pp. 1–9, 2010.
- [163] L. Fu and C. L. Kane, “Topological insulators with inversion symmetry,” *Physical Review B*, vol. 76, no. 4, p. 045302, 2007.
- [164] L. Fu and C. L. Kane, “Time reversal polarization and a  $Z_2$  adiabatic spin pump,” *Phys. Rev. B*, vol. 74, p. 195312, Nov 2006.
- [165] T. Fukui, Y. Hatsugai, and H. Suzuki, “Chern numbers in discretized brillouin zone: Efficient method of computing (spin) hall conductances,” *Journal of the Physical Society of Japan*, vol. 74, no. 6, pp. 1674–1677, 2005.
- [166] T. Fukui and Y. Hatsugai, “Quantum spin hall effect in three dimensional materials: Lattice computation of  $z_2$  topological invariants and its application to bi and sb,” *Journal of the Physical Society of Japan*, vol. 76, no. 5, p. 053702, 2007.

- [167] A. Avsar, J. Y. Tan, T. Taychatanapat, J. Balakrishnan, G. K. W. Koon, Y. Yeo, J. Lahiri, A. Carvalho, A. S. Rodin, E. C. T. O'Farrell, G. Eda, A. H. Castro Neto, and B. Ozylmaz, "Spin-orbit proximity effect in graphene.," *Nature communications*, vol. 5, p. 4875, 2014.
- [168] J. Zhang, C. Triola, and E. Rossi, "Proximity effect in graphene-topological-insulator heterostructures," *Physical Review Letters*, vol. 112, p. 096802, mar 2014.
- [169] T. P. Kaloni, L. Kou, T. Frauenheim, and U. Schwingenschlögl, "Quantum spin hall states in graphene interacting with  $ws_2$  or  $wse_2$ ," *Applied Physics Letters*, vol. 105, p. 233112, 2014.
- [170] G. Giovannetti, P. a. Khomyakov, G. Brocks, P. J. Kelly, and J. Van Den Brink, "Substrate-induced band gap in graphene on hexagonal boron nitride: Ab initio density functional calculations," *Physical Review B*, vol. 76, pp. 2–5, 2007.
- [171] M. Z. Hasan and C. L. Kane, "Colloquium," *Rev. Mod. Phys.*, vol. 82, pp. 3045–3067, Nov 2010.
- [172] X.-L. Qi and S.-C. Zhang, "Topological insulators and superconductors," *Rev. Mod. Phys.*, vol. 83, pp. 1057–1110, Oct 2011.
- [173] L. Fu, "Topological crystalline insulators," *Phys. Rev. Lett.*, vol. 106, p. 106802, Mar 2011.
- [174] M. Dzero, K. Sun, V. Galitski, and P. Coleman, "Topological kondo insulators," *Phys. Rev. Lett.*, vol. 104, p. 106408, Mar 2010.
- [175] S. Raghu, X.-L. Qi, C. Honerkamp, and S.-C. Zhang, "Topological mott insulators," *Phys. Rev. Lett.*, vol. 100, p. 156401, Apr 2008.
- [176] A. A. Soluyanov and D. Vanderbilt, "Computing topological invariants without inversion symmetry," *Phys. Rev. B*, vol. 83, p. 235401, Jun 2011.
- [177] D. Gresch, G. Autès, O. V. Yazyev, M. Troyer, D. Vanderbilt, B. A. Bernevig, and A. A. Soluyanov, "Z2pack: Numerical implementation of hybrid wannier centers for identifying topological materials," *Phys. Rev. B*, vol. 95, p. 075146, Feb 2017.
- [178] Q. Wu, S. Zhang, H.-F. Song, M. Troyer, and A. A. Soluyanov, "Wannier-tools: An open-source software package for novel topological materials," *Computer Physics Communications*, vol. 224, pp. 405 – 416, 2018.

- [179] P. San-Jose, A. Gutiérrez-Rubio, M. Sturla, and F. Guinea, “Spontaneous strains and gap in graphene on boron nitride,” *Phys. Rev. B*, vol. 90, p. 075428, Aug 2014.
- [180] J. Jung, E. Laksono, A. M. DaSilva, A. H. MacDonald, M. Mucha-Kruczyński, and S. Adam, “Moiré band model and band gaps of graphene on hexagonal boron nitride,” *Phys. Rev. B*, vol. 96, p. 085442, Aug 2017.
- [181] E. Wang, X. Lu, S. Ding, W. Yao, M. Yan, G. Wan, K. Deng, S. Wang, G. Chen, L. Ma, *et al.*, “Gaps induced by inversion symmetry breaking and second-generation dirac cones in graphene/hexagonal boron nitride,” *Nature Physics*, vol. 12, no. 12, pp. 1111–1115, 2016.
- [182] J. D. Sanchez-Yamagishi, J. Y. Luo, A. F. Young, B. M. Hunt, K. Watanabe, T. Taniguchi, R. C. Ashoori, and P. Jarillo-Herrero, “Helical edge states and fractional quantum hall effect in a graphene electron-hole bilayer,” *Nature nanotechnology*, vol. 12, no. 2, pp. 118–122, 2017.
- [183] A. F. Young, J. D. Sanchez-Yamagishi, B. Hunt, S. H. Choi, K. Watanabe, T. Taniguchi, R. C. Ashoori, and P. Jarillo-Herrero, “Tunable symmetry breaking and helical edge transport in a graphene quantum spin hall state,” *Nature*, vol. 505, pp. 528–32, jan 2014.
- [184] J. Alicea, Y. Oreg, G. Refael, F. von Oppen, and M. P. A. Fisher, “Non-abelian statistics and topological quantum information processing in 1d wire networks,” *Nature Physics*, vol. 7, p. 412, 2011.
- [185] O. Güçlü, H. Zhang, J. D. S. Bommer, M. W. A. de Moor, D. Car, S. R. Plissard, E. P. A. M. Bakkers, A. Geresdi, K. Watanabe, T. Taniguchi, and L. P. Kouwenhoven, “Ballistic majorana nanowire devices,” *Nature Nanotechnology*, vol. 13, pp. 192–197, 2016.
- [186] R. Bianco and R. Resta, “Mapping topological order in coordinate space,” *Phys. Rev. B*, vol. 84, p. 241106, Dec 2011.
- [187] A. Marrazzo and R. Resta, “Locality of the anomalous hall conductivity,” *Phys. Rev. B*, vol. 95, p. 121114, Mar 2017.
- [188] T. A. Loring, “K-theory and pseudospectra for topological insulators,” *Annals of Physics*, vol. 356, pp. 383–416, 2015.
- [189] N. P. Mitchell, L. M. Nash, D. Hexner, A. M. Turner, and W. T. Irvine, “Amorphous topological insulators constructed from random point sets,” *Nature Physics*, p. 1, 2018.

- [190] I. C. Fulga, D. I. Pikulin, and T. A. Loring, “Aperiodic weak topological superconductors,” *Phys. Rev. Lett.*, vol. 116, p. 257002, Jun 2016.
- [191] E. van Nieuwenburg, Y.-H. Liu, and S. Huber, “Learning phase transitions by confusion,” *Nature Physics*, vol. 13, pp. 435–439, feb 2017.
- [192] K. Ch’ng, J. Carrasquilla, R. G. Melko, and E. Khatami, “Machine learning phases of strongly correlated fermions,” *Phys. Rev. X*, vol. 7, p. 031038, Aug 2017.
- [193] T. Ohtsuki and T. Ohtsuki, “Deep learning the quantum phase transitions in random two-dimensional electron systems,” *Journal of the Physical Society of Japan*, vol. 85, no. 12, p. 123706, 2016.
- [194] W. Hu, R. R. P. Singh, and R. T. Scalettar, “Discovering phases, phase transitions, and crossovers through unsupervised machine learning: A critical examination,” *Phys. Rev. E*, vol. 95, p. 062122, Jun 2017.
- [195] P. Broecker, F. F. Assaad, and S. Trebst, “Quantum phase recognition via unsupervised machine learning,” *arXiv preprint arXiv:1707.00663*, 2017.
- [196] M. Koch-Janusz and Z. Ringel, “Mutual information, neural networks and the renormalization group,” *Nature Physics*, vol. 14, pp. 578–582, 2017.
- [197] G. Carleo and M. Troyer, “Solving the quantum many-body problem with artificial neural networks,” *Science*, vol. 355, no. 6325, pp. 602–606, 2017.
- [198] D.-L. Deng, X. Li, and S. Das Sarma, “Machine learning topological states,” *Phys. Rev. B*, vol. 96, p. 195145, Nov 2017.
- [199] D.-L. Deng, X. Li, and S. Das Sarma, “Quantum entanglement in neural network states,” *Phys. Rev. X*, vol. 7, p. 021021, May 2017.
- [200] Y. Zhang and E.-A. Kim, “Quantum loop topography for machine learning,” *Phys. Rev. Lett.*, vol. 118, p. 216401, May 2017.
- [201] Y. Nagai, H. Shen, Y. Qi, J. Liu, and L. Fu, “Self-learning monte carlo method: Continuous-time algorithm,” *Phys. Rev. B*, vol. 96, p. 161102, Oct 2017.
- [202] K. Ch’ng, N. Vazquez, and E. Khatami, “Unsupervised machine learning account of magnetic transitions in the hubbard model,” *Phys. Rev. E*, vol. 97, p. 013306, Jan 2018.

- [203] M. Rupp, A. Tkatchenko, K.-R. Müller, and O. A. von Lilienfeld, “Fast and accurate modeling of molecular atomization energies with machine learning,” *Phys. Rev. Lett.*, vol. 108, p. 058301, Jan 2012.
- [204] A. P. Bartók, S. De, C. Poelking, N. Bernstein, J. R. Kermode, G. Csányi, and M. Ceriotti, “Machine learning unifies the modeling of materials and molecules,” vol. 3, no. 12, 2017.
- [205] T. Gao, H. Li, W. Li, L. Li, C. Fang, H. Li, L. Hu, Y. Lu, and Z.-M. Su, “A machine learning correction for dft non-covalent interactions based on the s22, s66 and x40 benchmark databases,” *Journal of cheminformatics*, vol. 8, no. 1, p. 24, 2016.
- [206] P. Zhang, H. Shen, and H. Zhai, “Machine learning topological invariants with neural networks,” *Phys. Rev. Lett.*, vol. 120, p. 066401, Feb 2018.
- [207] N. Yoshioka, Y. Akagi, and H. Katsura, “Learning disordered topological phases by statistical recovery of symmetry,” *Phys. Rev. B*, vol. 97, p. 205110, May 2018.
- [208] *Imagenet classification with deep convolutional neural networks*, Neural Information Processing Systems Conference, 2012.
- [209] G. Dede and M. H. Sazlı, “Speech recognition with artificial neural networks,” *Digital Signal Processing*, vol. 20, no. 3, pp. 763 – 768, 2010.
- [210] Y. Lecun, L. Bottou, Y. Bengio, and P. Haffner, “Gradient-based learning applied to document recognition,” *Proc. IEEE*, vol. 86, no. 11, pp. 2278–2324, 1998.
- [211] Y. Goldberg, “A primer on neural network models for natural language processing,” *arXiv*, 2015.
- [212] Y. Bengio, R. Ducharme, P. Vincent, and C. Janvin, “A neural probabilistic language model,” *J. Mach. Learn. Res.*, vol. 3, pp. 1137–1155, Mar. 2003.
- [213] T. Schaul, J. Bayer, D. Wierstra, Y. Sun, M. Felder, F. Sehnke, T. Rückstieß, and J. Schmidhuber, “Pybrain,” *Journal of Machine Learning Research*, vol. 11, pp. 743–746, 2010.
- [214] R. Solomonoff, “An inductive inference machine,” *IRE Convention Record*, vol. 2, pp. 56–62, 1957.

- [215] A. L. Samuel, “Some studies in machine learning using the game of checkers,” *IBM Journal of Research and Development*, vol. 3, no. 3, pp. 206–226, 1959.
- [216] F. Rosenblatt, “The perceptron: A probabilistic model for information storage and organization in the brain.,” *Psychological Review*, vol. 65, no. 6, pp. 386–408, 1958.
- [217] A. L. Hodgkin and A. F. Huxley, “A quantitative description of membrane current and its application to conduction and excitation in nerve,” *J. Physiol.*, vol. 117, pp. 500–544, 1952.
- [218] J. J. Hopfield, “Neural networks and physical systems with emergent collective computational abilities,” *PNAS*, vol. 79, no. 8, pp. 2554–2558, 1982.
- [219] D. E. Rumelhart, G. E. Hinton, and R. J. Williams, “Learning representations by back-propagating errors,” *Nature*, vol. 323, no. 6088, pp. 533–536, 1986.
- [220] J. C. Budich and E. Ardonne, “Equivalent topological invariants for one-dimensional majorana wires in symmetry class  $d$ ,” *Phys. Rev. B*, vol. 88, p. 075419, Aug 2013.
- [221] R. M. Lutchyn, J. D. Sau, and S. Das Sarma, “Majorana fermions and a topological phase transition in semiconductor-superconductor heterostructures,” *Phys. Rev. Lett.*, vol. 105, p. 077001, Aug 2010.
- [222] Y. Oreg, G. Refael, and F. von Oppen, “Helical liquids and majorana bound states in quantum wires,” *Phys. Rev. Lett.*, vol. 105, p. 177002, Oct 2010.
- [223] V. Mourik, K. Zuo, S. M. Frolov, S. Plissard, E. Bakkers, and L. P. Kouwenhoven, “Signatures of majorana fermions in hybrid superconductor-semiconductor nanowire devices,” *Science*, vol. 336, no. 6084, pp. 1003–1007, 2012.
- [224] T. D. Stanescu, R. M. Lutchyn, and S. Das Sarma, “Majorana fermions in semiconductor nanowires,” *Phys. Rev. B*, vol. 84, p. 144522, Oct 2011.
- [225] R. M. Lutchyn, T. D. Stanescu, and S. Das Sarma, “Search for majorana fermions in multiband semiconducting nanowires,” *Phys. Rev. Lett.*, vol. 106, p. 127001, Mar 2011.

- [226] R. M. Lutchyn, E. P. A. M. Bakkers, L. Kouwenhoven, P. Krogstrup, C. M. Marcus, and Y. Oreg, “Majorana zero modes in superconductor-semiconductor heterostructures,” *Nature Reviews Materials*, vol. 3, pp. 52–68, 2018.
- [227] R. Aguado, “Majorana quasiparticles in condensed matter,” *La Rivista del Nuovo Cimento*, no. 11, pp. 523–593, 2017.
- [228] Z. Qiao, S. a. Yang, W. Feng, W.-K. Tse, J. Ding, Y. Yao, J. Wang, and Q. Niu, “Quantum anomalous hall effect in graphene from rashba and exchange effects,” *Physical Review B*, vol. 82, p. 161414, oct 2010.
- [229] J. L. Lado, J. W. González, and J. Fernández-Rossier, “Quantum hall effect in gapped graphene heterojunctions,” *Physical Review B*, vol. 88, p. 035448, jul 2013.
- [230] C. Tang, B. Cheng, M. Aldosary, Z. Wang, Z. Jiang, K. Watanabe, T. Taniguchi, M. Bockrath, and J. Shi, “Approaching quantum anomalous hall effect in proximity-coupled yig/graphene/h.bn sandwich structure,” *APL Materials*, vol. 6, no. 2, p. 026401, 2018.
- [231] Z. Wang, C. Tang, R. Sachs, Y. Barlas, and J. Shi, “Proximity-induced ferromagnetism in graphene revealed by the anomalous hall effect,” *Phys. Rev. Lett.*, vol. 114, p. 016603, Jan 2015.
- [232] S. Su, Y. Barlas, J. Li, J. Shi, and R. K. Lake, “Effect of intervalley interaction on band topology of commensurate graphene/euo heterostructures,” *Phys. Rev. B*, vol. 95, p. 075418, Feb 2017.
- [233] B. Huang, G. Clark, E. Navarro-Moratalla, D. R. Klein, R. Cheng, K. L. Seyler, D. Zhong, E. Schmidgall, M. A. McGuire, D. H. Cobden, *et al.*, “Layer-dependent ferromagnetism in a van der waals crystal down to the monolayer limit,” *Nature*, vol. 546, no. 7657, pp. 270–273, 2017.
- [234] J. Zhang, B. Zhao, T. Zhou, Y. Xue, C. Ma, and Z. Yang, “Strong magnetization and chern insulators in compressed graphene/cri<sub>3</sub> van der waals heterostructures,” *Phys. Rev. B*, vol. 97, p. 085401, Feb 2018.
- [235] H. Hellwig, R. F. C. Vessot, M. W. Levine, P. W. Zitzewitz, D. W. Allan, and D. J. Glaze, “Measurement of the unperturbed hydrogen hyperfine transition frequency,” *IEEE Trans. Instrum. Meas.*, vol. 19, no. 4, pp. 200–209, 1970.

- [236] Y. Yamashiro, Y. Ohno, K. Maehashi, K. Inoue, and K. Matsumoto, “Electric-field-induced band gap of bilayer graphene in ionic liquid,” *J. Vac. Sci. Technol. B, Nanotechnol. Microelectron. Mater. Process. Meas. Phenom.*, vol. 30, no. 3, p. 03D111, 2012.